TECHNISCHE
UNIVERSITÄT
WIEN
Vienna University of Technology

Diplomarbeit

Classification of signal sources based on seismic and acoustic measurements

ausgeführt am

Department für Geodäsie und Geoinformation
Forschungsgruppe Geophysik

der Technischen Universität Wien

unter der Anleitung von

Em. O.Univ.Prof.Dipl.-Ing. Dr. Ewald Brückl

durch

Matthias Steiner, BSc
Bründlfeldweg 10/1
7000 Eisenstadt

Wien, 30. 03. 2015

_____   _____
Unterschrift Verfasser   Unterschrift Betreuer

Abstract

The need for automated classification of signals recorded with seismic sensors led to the development of various classification techniques. However, most of these techniques use very complex hardware and software equipment. The present work investigates the potential of establishing a source classification that mainly relies upon the comparison of seismic and acoustic data.

Therefore, five rather generally described source types were defined. These source types cover all sources that are known or supposed to produce or induce seismic signals. Based upon these source types classification criteria relying on seismic and acoustic data were defined. In order to be able to verify the usability of these criteria a heterogeneous data set had to be generated that comprises signals produced by various sources. For this purpose in-situ experiments were carried out which incorporated seismic and acoustic sensors deployed in form of a sensor array. Additionally, meteorological parameters were observed.

From the recorded data various parameters describing the signal characteristics could be obtained and were used to compute possible classification criteria. The ratio of seismic and acoustic signal amplitudes and the amplitude spectrum similarity can be used to distinguish seismic and acoustic sources. The slowness computed via array analysis was found to be a third possible classification criterion allowing for an identification of high altitude acoustic sources and different seismic wave phases. However, it was shown that the array analysis maybe would require an interactive processing flow.

Based on these criteria classification diagrams were generated. These diagrams clearly illustrate the usability of the three criteria for the classification of signal sources. The amplitude ratio might even be used as a real-time classification criterion.

Finally, suggestions on how to improve the data basis and regarding an efficient design of a sensor array are discussed.

Kurzfassung

Die Notwendigkeit der automatischen Klassifizierung von Signalen in seismischen Daten hat zur Entwicklung von verschiedenen Klassifizierungsmethoden geführt. Die meisten dieser Methoden nutzen jedoch komplexe Hardware und Software-Komponenten. Die vorliegende Arbeit untersucht die Möglichkeit der Einführung einer Klassifizierungsmethode, welche hauptsächlich auf dem Vergleich von seismischen und akustischen Daten basiert.

Es wurden fünf relativ allgemein beschriebene Klassen von Quellen definiert. Diese Klassen umfassen alle Arten von Quellen, von denen bekannt ist oder vermutet wird, dass sie seismische Signal hervorrufen. Ausgehend von diesen Klassen wurden Klassifikationskriterien definiert. Um die Brauchbarkeit dieser Kriterien zu prüfen musste eine heterogene Datenbasis geschaffen werden. Die Datenbasis sollte Signale, welche von verschiedenen Quellen produziert wurden, enthalten. Zu diesem Zweck wurden Experimente durchgeführt, bei denen sowohl seismische als auch akkustische Sensorarrays eingesetzt wurden. Zusätzlich wurden meteorologische Parameter gemessen.

Aus den aufgezeichneten Daten konnten verschiedenste Parameter gewonnen werden, welche die Signalcharakteristiken beschreiben. Diese Parameter wurden verwendet, um mögliche Klassifizierungskriterien zu berechnen. Das Verhältnis der seismischen und akkustischen Signalamplituden und die Ähnlichkeit der Amplitudenspektren können für die Unterscheidung von seismischen und akustischen Quellen verwendet werden. Die Langsamkeit, welche mittels Array-Analyse berechnet wurde, konnte als drittes mögliches Kriterium gefunden werden, welches die Identifizierung von akustischen Quellen und von verschiedenen Phasen seismischer Wellen ermöglicht. Die Durchführung der Array-Analyse benötigt jedoch eine interaktive Prozessierung.

Basierend auf diesen Kriterien wurden Klassifizierungsdiagramme erstellt. Diesen Diagramme haben die Eignung der drei Kriterien für die Klassifizierung von Quellen bestätigt. Das Amplitudenerhältnis könnte auch als Echtzeit-Klassifizierunskriterium verwendet werden.
Abschließend sind Vorschläge zur Verbesserung der Datenbasis und für ein effizientes Design von Sensorarrays angeführt.

Contents

Contents

List of Tables

List of Figures

Chapter 1

Introduction

In most cases recorded seismic data comprise not only signals being relevant for a further analysis but also signals that are of less or even no interest. Commonly, these unwanted signals are referred to as seismic noise. The definition of the terms "signal" and "noise" is a subjective one, since by using the appropriate analysis tools ones noise can become the other ones signal. The most common noise sources are human activities (air and road traffic, industry, . . .) and natural events (thunder/bolt, fauna, wind, falling trees, . . .). The problem arising from the presence of noise in the seismic data is the waste of resources. Consider an analysis tool that processes seismic signals in order to obtain some geophysical parameter. If the signal in the seismic data was not produced by a seismic source the analysis tool may compute an erroneous parameter or the computation may even fail. Nevertheless, the analysis tool accessed the available resources but never could have efficiently used them. This inefficiency can be reduced by preventing the analysis tool to process insufficient signals.

Many approaches to automatically classify or discriminate signals in seismic data utilize neural networks (Dysart and Pulli, 1990; Scarpetta et al., 2005; Langer et al., 2006; Esposito et al., 2006). In some cases acoustic sensors are installed at monitoring sites in addition to the common seismic monitoring equipment. For example, the relation between the seismic and acoustic data comprises crucial information on volcanic activity (Rowe et al., 2000). Infrasound measurements are used to support the characterisation of mass movements like landslides and avalanches (Suriñach, Vilajosana et al., 2005; Kogelnig et al., 2014).

In the present thesis the potential of simultaneously recording seismic and acoustic data in order to conclude on the source type is analysed. By contrast to the infrasound measurements mentioned before the acoustic data is recorded in the audible range of the human being. The feasibility and usability of this approach are evaluated by classifying different sources based on criteria deduced from in-situ experiment data.

Chapter 2

Seismology

Seismology is a scientific discipline studying the propagation of elastic waves through the Earth and the associated ground motions (earthquakes). Although Chinese scientist Zhang Heng[1] already built the first functional seismoscope in 132 modern seismology is a comparatively young science since quantitative studies were carried out for the first time some 110 years ago. Amongst others Galileo[2], Newton[3] and Hooke[4] laid the basement on which Navier[5] set down the generalized equations of elasticity in 1810. The principles of modern elasticity theory were completed by Chauchy[6] and Poisson[7] in the early 19th century. A major milestone for seismology was the intensively studied great San Francisco earthquake of 1906. These investigations gave the impulse for the development of the elastic rebound theory by Reid[8]. In the same year Oldham[9] found an explanation for the travel times of teleseismic waves through the body by stating a large, dense and probably fluid core. The most well-known scale for quantifying earthquakes is the Richter scale introduced by Richter[10] and Gutenberg[11] in 1935. The search for petroleum promoted the evolution of refraction and reflection seismology using artificial sources. With the dawning of the age of computer technology the modern field of seismic tomography evolved. In the field of earthquake seismology the need to protect mankind and its modern achievements led to the development of construction codes to reduce earthquake damage as well as to attempts in earthquake prediction (Lowrie, 1997).

Seismology is built on the achievements of great scientists and a continuously evolving science. Covering the whole field of seismology in detail would go beyond the scope of this thesis. Hence, the subsequent sections only cover the basics of seismic wave theory and seismic monitoring.

---

[1] Zhang Heng (78–135) Chinese polymath
[2] Galileo Galilei (1564–1642) Italian physicist, mathematician, engineer, astronomer, and philosopher
[3] Sir Isaac Newton (1642–1727) English physicist and mathematician
[4] Robert Hooke FRS (1635–1703) English polymath
[5] Claude-Louis Navier (1785–1836) French engineer and physicist
[6] Baron Augustin-Louis Cauchy (1789–1857) French mathematician
[7] Siméon Denis Poisson (1781–1840) French mathematician
[8] Harry Fielding Reid (1859–1944) American geophysicist
[9] Richard Dixon Oldham FRS (1858–1936) British geologist
[10] Charles Francis Richter (1900–1985) American seismologist and physicist
[11] Beno Gutenberg (1889–1960) German-American seismologist

2.1. Seismic waves

A force applied to a material causes the particles of the material to be displaced from their original positions. When the force is removed and the dislocated particles return to their original positions the material shows an elastic behaviour. The key terms of elastic theory are stress σ, the force per unit area, and strain e, the deformation due to stress.

An elastic medium reverts to its natural state (stresses and strains are zero) when applied forces are removed. Stress and strain will change together under the influence of applied loads. The relation between them is given by the material's constitutive equation which is an important characteristic of the medium. For a linearly elastic material the constitutive equation is called Hooke's law

$$\sigma_{ij} = c_{ijkl}e_{kl} \tag{2.1}$$

written here by using the summation convention. Each component of the stress tensor is a linear combination of all components of the strain tensor (Aki and Richards, 2002).

The elastic moduli c_{ijkl} describe the properties of the material. c_{ijkl} is a fourth-order tensor containing a total of 81 components. This large number of tensor elements can be reduced by various considerations. Finally, for an isotropic material the constitutive equation can be rewritten by using just the Lame constants (λ, μ) as

$$\sigma_{ij} = \lambda e_{kk}\delta_{ij} + 2\mu e_{ij} = \lambda\theta\delta_{ij} + 2\mu e_{ij} \tag{2.2}$$

where θ is the dilatation (Stein and Wysession, 2007).

In order to solve the homogeneous equation of motion

$$\frac{\partial\sigma_{ij}(\mathbf{x},t)}{\partial j} = \rho\frac{\partial^2 u_i(\mathbf{x},t)}{\partial t^2} \tag{2.3}$$

Eq. 2.2 is required to express σ_{ij} in terms of displacement. The relation of the strain tensor to the displacement is given by $e_{ij} = \frac{1}{2}(\partial_i u_j + \partial_j u_i)$. Substituting for e_{ij} in Eq. 2.2 yields

$$\sigma_{ij} = \lambda\delta_{ij}\partial_k u_k + \mu(\partial_i u_j + \partial_j u_i) \tag{2.4}$$

By substituting Eq. 2.4 into Eq. 2.3 the equation of motion for an isotropic elastic medium is obtained (Stein and Wysession, 2007)

$$(\lambda + 2\mu)\mathbf{\nabla}(\mathbf{\nabla}\cdot\mathbf{u}(\mathbf{x},t)) - \mu\mathbf{\nabla}\times(\mathbf{\nabla}\times\mathbf{u}(\mathbf{x},t)) = \rho\frac{\partial^2\mathbf{u}(\mathbf{x},t)}{\partial t^2} \tag{2.5}$$

It is important to note that this equations neglects the gravity and velocity gradient terms and assumes a linear, isotropic Earth model and thus is an approximate expression (Shearer, 1999).

2.1.1. Body waves

According to (Aki and Richards, 2002) the displacement $\mathbf{u}(\mathbf{x}, t)$ can be expressed in terms of two other functions, ϕ and ψ, by using the Helmholtz decomposition theorem

$$\mathbf{u}(\mathbf{x}, t) = \boldsymbol{\nabla}\phi(\mathbf{x}, t) + \boldsymbol{\nabla} \times \boldsymbol{\psi}(\mathbf{x}, t) \tag{2.6}$$

Hence the displacement is the sum of the gradient of the scalar potential $\boldsymbol{\nabla}\phi(\mathbf{x}, t)$ and the curl of the vector potential $\boldsymbol{\nabla} \times \boldsymbol{\psi}(\mathbf{x}, t)$. Substituting the potentials into Eq. 2.5 and using the vector identities

$$\boldsymbol{\nabla}^2 = \boldsymbol{\nabla}(\boldsymbol{\nabla} \cdot \mathbf{u}) - \boldsymbol{\nabla} \times (\boldsymbol{\nabla} \times), \quad \boldsymbol{\nabla} \times (\boldsymbol{\nabla}\phi) = 0, \quad \boldsymbol{\nabla} \cdot (\boldsymbol{\nabla} \times \boldsymbol{\psi}) = 0$$

yields a solution for the seismic wave equation. In fact the elastic wave equation is turned into simpler equations for potentials.

For a harmonic plane wave the scalar potential satisfies the scalar wave equation

$$\nabla^2 \phi(\mathbf{x}, t) = \frac{1}{\alpha^2} \frac{\partial^2 \phi(\mathbf{x}, t)}{\partial t^2} \tag{2.7}$$

corresponding to P, or compressional, waves with the velocity

$$\alpha = \left(\frac{\lambda + 2\mu}{\rho}\right)^{1/2} \tag{2.8}$$

The scalar potential for a seismic wave propagating in the x direction is

$$\phi(x, t) = A e^{i(\omega t - kx)}$$

and the resultant displacement is the gradient

$$\mathbf{u}(x, t) = \boldsymbol{\nabla}\phi(x, t) = (-ik, 0, 0) A e^{i(\omega t - kx)} \tag{2.9}$$

with a non-zero component only along the propagation direction x. Since the dilatation is non-zero a volume change occurs within the material. The displacements in the direction of wave propagation cause alternating compressions and dilatations of the material (cf. Fig. 2.1 a)). Thus, the P waves are called compressional waves.

By contrast to the scalar potential, the vector potential satisfies the vector wave equation

$$\nabla^2 \boldsymbol{\psi}(\mathbf{x}, t) = \frac{1}{\beta} \frac{\partial^2 \boldsymbol{\psi}(\mathbf{x}, t)}{\partial t^2} \tag{2.10}$$

corresponding to S, or shear, waves with the velocity

$$\beta = \left(\frac{\mu}{\rho}\right)^{1/2} \tag{2.11}$$

The vector potential for a seismic wave propagating in the x direction is

$$\boldsymbol{\psi} = (x, t) = (A_x, A_y, A_z)\, e^{i(\omega t - kx)}$$

and the resultant displacement field is given by the curl

$$\boldsymbol{\psi}(x, t) = \nabla \times \boldsymbol{\psi}(x, t) = (0, ikA_z, -ikA_y)\, e^{i(\omega t - kx)} \tag{2.12}$$

where the component along the propagation direction vanishes. This implies that displacements related to a propagating shear wave arise perpendicular to the direction of wave propagation (cf. Fig. 2.1 b)). There is no change of volume induced by shear waves since the dilatation, $\nabla \cdot \mathbf{u}(z, t)$, is zero.
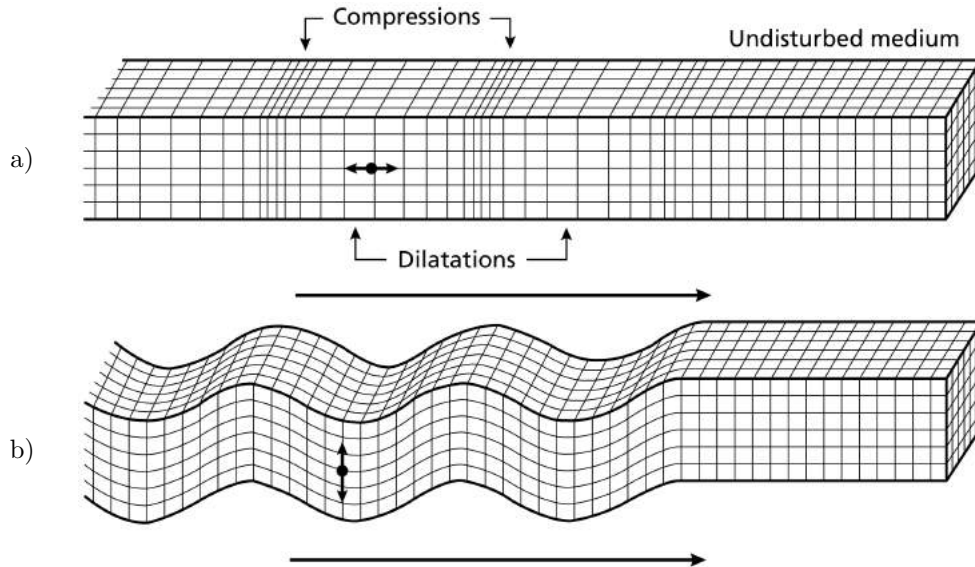
Figure 2.1.: *Elastic deformations and ground particle motions associated with the passage of body waves (Bolt, 1982):*
a) P wave
b) S wave

A wave is characterized by two directions as can be seen from the displacements for P and S wave. One direction is the propagation direction of the wave and the other one is the direction of change of the displacement field. The P wave is an example of a longitudinal wave since the displacement field varies in the direction of propagation. A sound wave in air described as a compressional (elastic) wave in an ideal fluid (see Chapter 3) is another example for this type of wave. The S wave is an example of a transverse wave. By contrast to the P wave the displacement field varies perpendicular to the propagation direction (Stein and Wysession, 2007).

Consider the representation of a generalized vibration with respect to an orthogonal reference system as shown in Fig. 2.2. In this sketch the two orthogonal components of the general S wave motion within a wavefront can be distinguished. Both components are perpendicular to the seismic ray, one lying in the horizontal plane and the other one lying in the vertical plane. Therefore, the former one is the so-called SV wave, whereas the latter one is denoted as the SH wave (Lowrie, 1997).
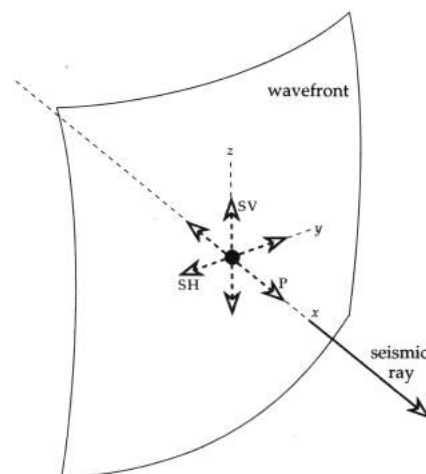
Figure 2.2.: *Sketch of seismic wave vibrations with respect to an orthogonal reference system (Lowrie, 1997)*

It would be permissible to choose any two orthogonal polarizations in the plane of S wave displacements. However, by using SV and SH it is possible to describe the coupling of P and SV waves when they interact with horizontal boundaries (Stein and Wysession, 2007).

2.1.2. Surface waves

As mentioned above P and SV waves tend to interact and give rise to another type of seismic waves. Hence, a seismogram resulting from an earthquake does not only consist of P and S wave arrivals where later arrivals are waves reflected and converted at interfaces within the Earth. In practice, seismograms are dominated by so-called surface waves that arrive after the body waves. The energy of these longer-period waves is concentrated near the Earth's surface.

Due to geometric spreading the energy spreads only in two dimensions and the amplitudes decay with distance r from the source approximately as $r^{-1/2}$. By contrast, the body wave energy spreads in three dimensions and the amplitude decay is approximately $r^{-1/4}$. The different decay rates of body and surface wave cause the amplitudes of surface waves to be more prominent in seismograms at large distances from the source.
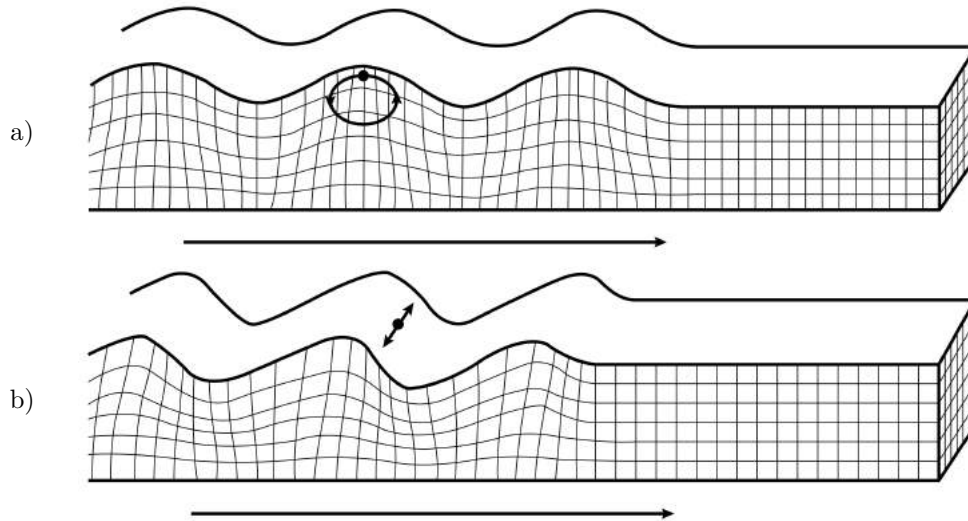
Figure 2.3.: *Elastic deformations and ground particle motions associated with the passage of surface waves (Bolt, 1982):*
a) Rayleigh wave
b) Love wave

The reflected wave energy of a P (or SV) wave arriving at the surface contains both, P and SV waves[12]. For two coupled inhomogeneous P and SV waves propagating along the surface of a half-space the wave equation can be solved as shown by Lord Rayleigh[13] more than 100 years ago (Bormann, Engdahl et al., 2002). Rayleigh waves exist at the top of a homogeneous halfspace as a combination of P and SV waves[14]. In order to describe this surface wave type the free surface is defined as $z = 0$, z is measured downwards and potentials for waves propagating in the x-z plane are used. Since they can satisfy the free surface boundary conditions and do not interact with SH waves only P and SV waves are considered. Combining the potentials of these wave types requires two conditions to be fulfilled. The first condition demands the energy to be trapped near the surface so it cannot propagate away from it. The other condition requires the free surface boundary conditions to be satisfied and subsequently the traction of the free surface to vanish[15] (Stein and Wysession, 2007). As can be seen in Fig. 2.3 a), in a plane perpendicular to the surface the particle motions are elliptical and contain the direction of wave propagation.

---

[12] Due to mode conversion
[13] John William Strutt, 3rd Baron Rayleigh, OM, PRS (1842–1919) English physicist
[14] They may also propagate along the boundary between two dissimilar solid media (Kearey et al., 2002)
[15] This condition arose for the P-SV reflection at a free surface

Note that the motion is retrograde at the surface and prograde at shallow depths, respectively. The propagation velocity of Rayleigh waves is lower than that of S waves and they would be non-dispersive in a homogeneous half-space. Due to velocity variation with depth in the Earth's interior Rayleigh waves travelling round the surface of the Earth show a dispersive behaviour (Kearey et al., 2002).

Love[16] waves are a second type of surface waves that results from the interactions of SH waves. A two-layer model with a top layer of thickness h of material with velocity β_1 underlain by a halfspace of material with velocity β_2, where $\beta_2 > \beta_1$, is the simplest geometry in which a Love wave occurs (Stein and Wysession, 2007). As shown in Fig. 2.3 b) the particle motion of these polarized shear waves is perpendicular to the direction of wave propagation and parallel to the free surface. Love wave velocities are an average of the shear wave velocity of the topmost (surface) layer and that of deeper layers. In contrast to Rayleigh waves Love waves are inherently dispersive (Kearey et al., 2002).

2.2. Seismic monitoring

Seismometry is the generic term for the design and development of seismic instrumentation.

Although it is common practice to denote a system recording ground motions as seismometers, the correct term is seismograph. The seismometer actually records the ground motion and thus is just one key component of the entire system called seismograph. Besides the ground motion sensor the seismograph also contains amplifying, timing, and recording components. Recording ground motion as a function of time yields a so-called seismogram. The seismogram depends upon the whole seismograph system and thus especially upon the frequency-dependent sensitivities of seismometers. Furthermore, a seismometer may record ground motion as displacement, velocity, acceleration or even various combinations of these quantities (Stein and Wysession, 2007).

2.2.1. Seismometer

Seismometers (frequently also referred to as geophones, detectors, phones or jugs) are used to detect seismic energy arriving at the surface. The first seismometers were mechanical instruments, but nowadays electromagnetic seismometers are used.

The equation of the mechanic seismometer

$$\ddot{z} + 2\epsilon\dot{z} + \omega_0^2 = -\ddot{u} \tag{2.13}$$

states that by measuring the mass displacement $z(t)$ and its time derivatives the Earth acceleration $\ddot{u}(t)$ can be recovered.

---

[16]Augustus Edward Hough Love FRS (1863–1940) English mathematician
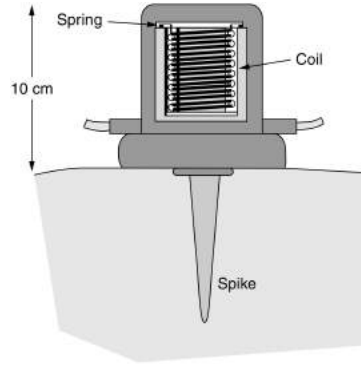
Figure 2.4.: *Schematic diagram of a moving-coil electromagnetic geophone (Milsom, 2003)*

Substituting the harmonic Earth displacement and the displacement response into Eq. 2.13 yields the frequency response function of the seismometer

$$T\left(\omega\right) = \frac{Z\left(\omega\right)}{U\left(\omega\right)} = \frac{\omega^2}{\omega_0^2 - 2\epsilon i\omega - \omega^2} \tag{2.14}$$

The complex frequency response function can be written in terms of the amplitude response

$$|T\left(\omega\right)| = \frac{\omega^2}{\left[\left(\omega^2 - \omega_0^2\right)^2 + 4\epsilon^2\omega^2\right]^{1/2}} \tag{2.15}$$

and the phase response

$$\phi\left(\omega\right) = -\tan^{-1}\frac{2\epsilon\omega}{\omega^2 - \omega_0^2} + \pi \tag{2.16}$$

Subsequently a geophone of the moving-coil electromagnetic type as shown schematically in Fig. 2.4 is considered. Since an electromagnetic transducer is used the equations discussed above have to be multiplied with ω. The geophone consists of a cylindrical permanent magnet with a circular slot cut into it (to separate the central South Pole from the annular North Pole). The coil is made up of a large number of turns of very fine wire and is suspended centrally in the slot by means of light leaf springs.

In order to detect seismic waves the geophone is placed on the ground in an upright position in firm contact with the soil. In the case of vertical ground movement the magnet moves but the coil tends to stay fixed due to its inertia. A voltage is generated between the terminals of the coil by the relative movement between the coil and the magnetic field. The output signal of an electromagnetic geophone is proportional to the velocity of the coil motion (Sheriff and Geldart, 1995).

In Fig. 2.5 the amplitude and phase response curves are plotted for an $1\,\mathrm{Hz}$[17] seismometer for values of h ranging from 1/4 to 4. h is the damping constant defined as $h = \dfrac{\epsilon}{\omega_0}$ and describes the strength of the damping relative to the stiffness of the spring. A seismometer is said to be critically damped if the damping constant is $h = 1$. Critical damping ensures a displaced mass to return to its initial position in the least possible time, hence oscillations of the mass about its rest position are prevented. A smaller damping constant ($h < 1$) causes an accordingly pronounced resonant peak occurs (Shearer, 1999).
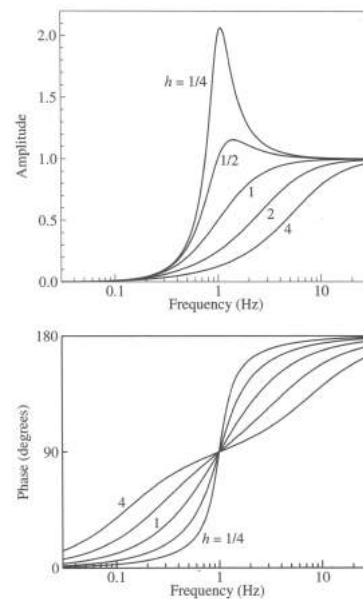
Figure 2.5.: *Amplitude (top) and phase (bottom) response functions for a 1 Hz seismometer (Shearer, 1999)*

2.2.2. Seismograph

Before the first digital systems were installed in the 1970s analog seismographs were used. The Wood[18]-Anderson[19] seismograph is a well-known example for an analog system since it was used by Richter for the definition of his famous Richter scale.

Modern digital seismographs produce easy to use digital data. Fig. 2.6 depicts this procedure. On the far left of the illustration the waveform represents the ground motion that is detected by the seismometer. The ground motion is converted into an analog electrical signal and is amplified afterwards. Aliasing can be avoided by using a combination of anti-aliasing filters. An analog anti-aliasing (AAA) filter in form of an initial frequency domain low-pass filter is commonly used by many seismographs.

---

[17]Heinrich Rudolf Hertz (1857–1984) German physicist
[18]Harry Oscar Wood (1879-1958) American seismologist
[19]John August Anderson (1876–1959) American astronomer

The next step is the transition from an analog system to a digital one. Digitisation of the filtered signal is achieved by oversampling the signal at a sampling rate of at least twice the AAA filter frequency in order to avoid aliasing. Afterwards a convolution of this signal and a digital anti-aliasing (DAA) filter[20] is performed. Finally, the signal is resampled at twice the desired Nyquist[21] frequency (Stein and Wysession, 2007).
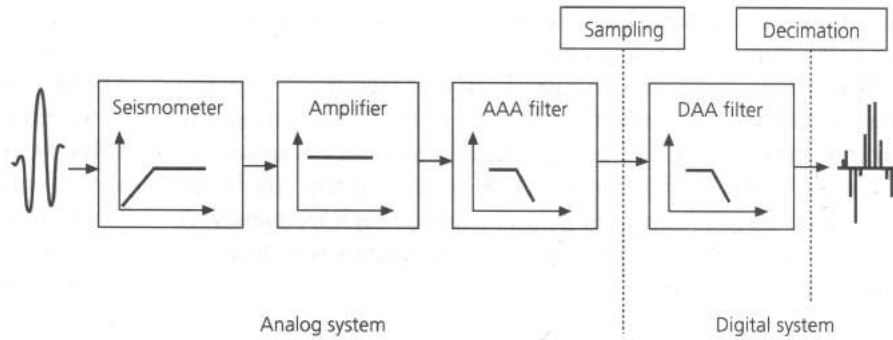
Figure 2.6.: *Schematic diagram depicting the analog-to-digital (ADC) process (Stein and Wysession, 2007)*

2.2.3. Seismic arrays

Essentially, a seismic array is equivalent to a seismic network since both consist of multiple sensors. The terms array and network can be distinguished by taking into account some basic characteristics.

The main difference between an array and a local network arises from the techniques used for data analysis. Hence, it is possible to analyse network data with array processing techniques as well as to use a sensor array as a network. Nevertheless, array processing techniques require high signal coherency across the single array stations. This circumstance gives rise to constraints concerning array geometry, spatial extent, and data quality. Data analysis with array processing techniques requires stable, high precision relative timing of all array stations during data acquisition since the differences between the arrival times are usually very small (Schweitzer et al., 2002). Array processing techniques are utilized if the hypocenter is located some distance away from the array site. If the hypocenter is located within the array layout array methods may not produce reliable results and network processing techniques have to be used.

Seismic arrays and the corresponding processing techniques are superior to single three component seismometers due to the enhancement of the signal-to-noise ratio (cf. Sec. 5.4.1). For this thesis another capability of sensor arrays is more important.

---

[20]often called a finite impulse response (FIR) filter
[21]Harry Nyquist (1889–1976) American physicist

By using sensor arrays it is possible to determine the receiver-to-source azimuth (hereinafter denoted as backazimuth) and the apparent velocity of different signal types. These results can be used for event location purposes and maybe for the classification of signal types (Schweitzer et al., 2002).

2.2.3.1. Fundamental terms

An array consists of a set of seismometers and in most cases is arranged following a geometric pattern. The sketch in Fig. 2.7 illustrates a seismic array with a circular station layout (blue dots) and the central station assigned as the reference site[22]. Array processing techniques use the relative distances $\mathbf{r}_j$ from the reference point to all other array sites (Schweitzer et al., 2002). Different array processing routines require the array positions to be given in different coordinate systems.
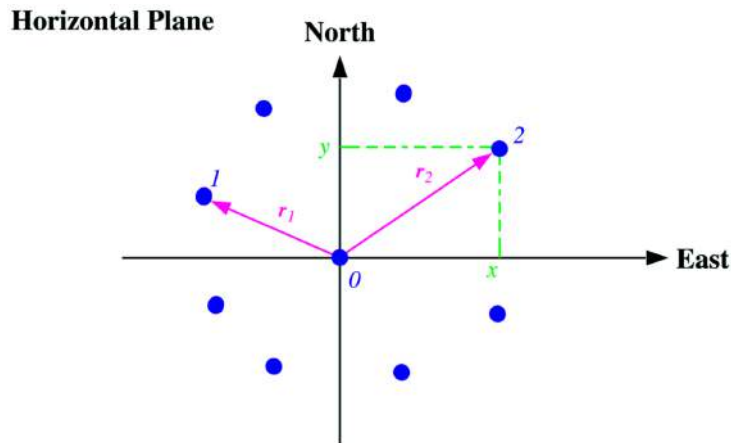
Figure 2.7.: *Sketch of an array of sensors (blue dots) in the horizontal plane (Schweitzer et al., 2002)*

For a start plane wave fronts are considered. A wave front coming from North-East and crossing the array in a South-Westerly direction projected onto the horizontal plane is illustrated in Fig. 2.8. The directions of approach and propagation are defined by the angles ϕ and θ. The backazimuth ϕ corresponds to the angle of wavefront approach and is measured clockwise between the North and the direction to the hypocenter in °. Based on the backazimuth the direction of propagation can be defined as $\theta = \phi \pm 180°$ (Schweitzer et al., 2002).

Comparing the distance from the array site to the source to the array size indicates if plane or circular wave fronts have to be considered by the array processing techniques. If the distance to the source is at least ten wavelengths the source an be considered to be at infinity, it is permissible to assume plane wave fronts as shown in Fig. 2.9 a) (Schweitzer et al., 2002).

---

[22]The center of the array equivalently can be assigned as the reference site (Rost and Thomas, 2002)
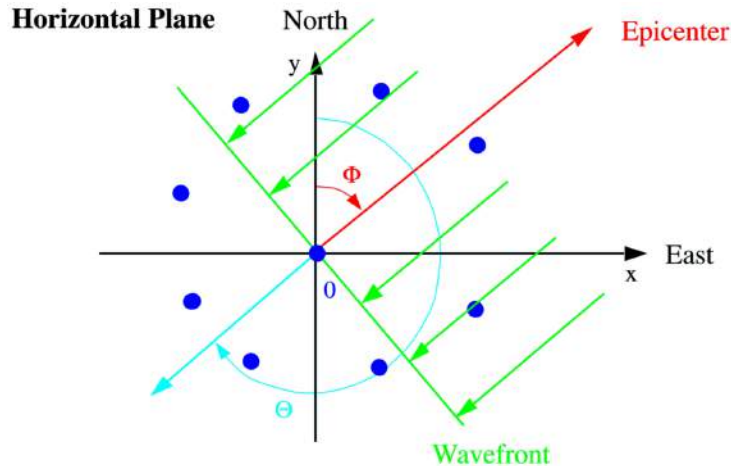
Figure 2.8.: *Direction of wavefront propagation θ and direction to the epicenter (backazimuth φ) in relation to a sensor array (Schweitzer et al., 2002)*

This assumption is not valid if the distance to the source compared to the array extent is smaller than ten wavelengths (cf. Fig. 2.9 b)). Due to the nearby source it is necessary to consider circular wave fronts (Almendros et al., 1999). For a distant source the array processing techniques are the so-called plane-wave-front methods (PWM) and in the case of a nearby source are referred to as circular-wave-front methods (CWM).
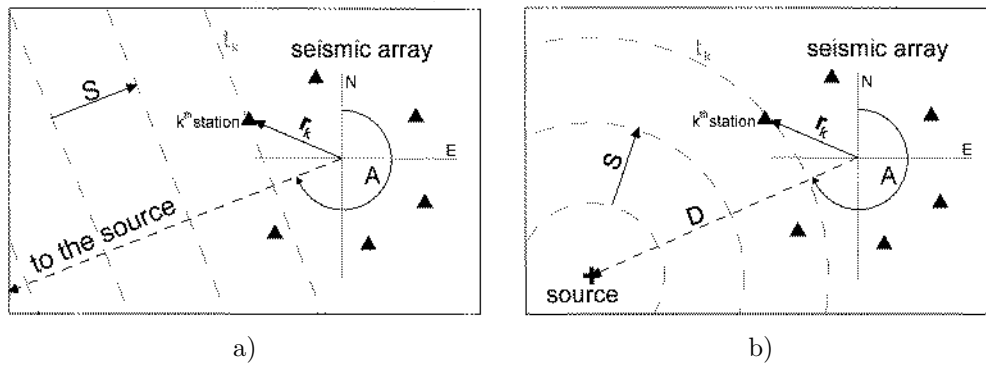
Figure 2.9.: *Illustration of wave front characteristics dependent on the distance to the source (Almendros et al., 1999):*
a) plane wave fronts for a distant source
b) circular wave fronts for a nearby source

The array and the wave front running across it projected onto the vertical plane are illustrated in Fig. 2.10. Using this illustration the angle of incidence i can be defined as the angle measured between the direction of approach and the vertical. The apparent velocity of a seismic wave is defined by the (upper) crustal velocity v_c and the angle of incidence i as

$$v_{app} = \frac{v_c}{\sin i} \qquad (2.17)$$
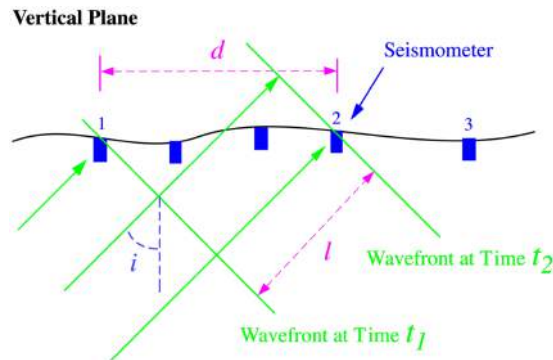
Figure 2.10.: *Sketch of a seismic plane wave running across a sensor array in the vertical plane (Schweitzer et al., 2002)*

The crustal velocity is measured in $\mathrm{km\,s^{-1}}$ and represents the velocity immediately below the array.

The slowness vector $\vec{p}$ of an incident seismic wave can be split in a horizontal p and a vertical component q (cf. Fig. 2.11), whereas the horizontal component is commonly denoted as the ray parameter. The ray parameter is the geometric property of a seismic ray that remains constant throughout its path[23]. It is invariant in transmission, reflection, refraction and transformation and is related to the apparent velocity by

$$p = \frac{1}{v_{app}} \tag{2.18}$$

Thus, the velocity of a seismic wave can be obtained via

$$s^2 = p^2 + q^2 = \frac{1}{v^2}$$
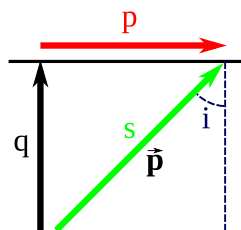
Figure 2.11.: *Relation between the incident angle i of a seismic plane wave and the ray parameter p (modified after Schweitzer et al., 2002)*

---

[23]Can be verified with Snell's law.

2.2.3.2. Modern developments in array seismology

The Basel Deep Heat Mining Project is a prominent example of induced seismicity in an urban region. Since an earthquake struck the city of Basel in 2006 a profound risk analysis was carried out (Baisch et al., 2009). Besides conventional seismic monitoring a microseismic survey was conducted with two mini arrays and the analysis was performed with a special software package yielding remarkable results (Häge et al., 2013). This method to detect microseisms in a certain region is called nanoseismic monitoring (Joswig, 2008) and was originally developed for the planned on-site inspections of the Comprehensive Test Ban Treaty Organization (CTBTO)[24].

2.3. Seismic sources

According to (Bormann, Baumbach et al., 2002) seismic sources can be subdivided into two main categories (as shown in Fig. 2.12), namely natural and man-made events. Each main category comprises four subcategories whereupon most of them discriminate the different types of earthquakes. Note that dividing earthquakes into natural and man-made events is a bad practice with regard to the present thesis. Besides the controlled sources the subcategories storm microseisms and cultural noise are of special interest. The term storm microseisms mainly refers to the effect of wind acting on the natural or artificial topography producing seismic signals. Anthropogenic activities, e.g. traffic, inducing seismic signals are denoted as cultural noise. Obviously, none of these subcategories covers the impact of acoustic signals on ground movement.

For the subsequently given discussion of seismic sources the classification of Bormann is substituted by an alternative subdivision. By contrast, the sources are divided into three main categories, namely Seismic Noise, Controlled Sources and Natural Sources. By using the new classification it is possible to include sound-induced events.

2.3.1. Seismic noise

Seismic noise is caused by many factors that range from solar and lunar tides within the solid Earth and temperature and atmospheric pressure fluctuations to human activities, storms and ocean waves (Zhang et al., 2009). Since these factors are constantly acting on the Earth the crust is continually reverberating. Investigations showed that noise mainly occurs at periods between 1 s and 10 s. The associated seismic waves are called microseims (Stein and Wysession, 2007).

These seismic signals are poorly localized in space and can not be fixed to a specific origin time. Thus, in most cases noise sources give rise to more or less permanently proceeding non-coherent interfering signals.

---

[24]http://www.ctbto.org
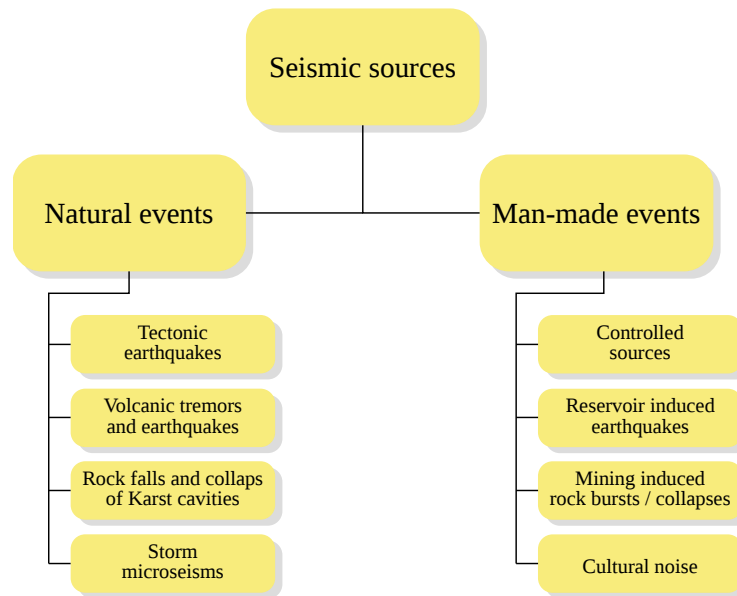
Figure 2.12.: *Conventional subdivision of seismic sources, after (Bormann, Baumbach et al., 2002)*

Season (natural noise) and/or time of day (cultural noise) often control the intensity of the seismic noise. Per definition noise practically is present all the time but it is not felt by people since the associated displacement amplitudes are usually by far smaller than those caused by other natural and controlled sources. Depending on the source which produced the seismic noise natural and cultural (or anthropogenic) noise are distinguished. Cultural seismic noise denotes seismic signals due to human activities such as industry, traffic, energy infrastructure etc. On the other hand rivers, water falls, wind etc. are sources that produce natural seismic noise without human intervention (Bormann, Baumbach et al., 2002).

2.3.2. Controlled sources

At the beginning of modern seismological surveys small charges of dynamite were used as seismic sources. Although impact and vibratory sources are more popular nowadays, explosives are still widely used (Milsom, 2003).

In most cases the choice of a seismic source relies on five desirable characteristics (Gadallah and Fisher, 2009)

Signal High amplitude and broad frequency bandwidth

Safety Hazards associated with usage, storage and maintenance do not require excessive precautions

Cost Low overall cost for equipment (acquisition, operation and maintenance) and supplies

Operation Simple, fast and thus efficient operation

Environment Source should cause minimal physical and biological damage to the surroundings

2.3.2.1. Explosives

Usually explosives are loaded at the bottom of a drilled hole. Thus, at least one drill mounted on a truck is required. Since most drills use a drilling fluid (mud) another truck has to deliver water to the drill so that the fluid can be made. A two-person crew is able to operate the drill. Explosives commonly used as charge are dynamite or ANFO[25]. Drill depth and shot medium define the size of the charge. The preferred approach is to drill through the low-velocity zone (weathering layer). Using an uphole geophone (cf. Fig. 2.13) the travel time through the low-velocity zone can be measured directly[26]. Since the seismic wave only once passes through the weathering layer signal attenuation and generation of surface waves are reduced. A significant part of the explosion energy is transmitted as seismic waves omnidirectionally radiating outward with spherical wavefronts as shown in Fig. 2.13. Note that a considerable part of this energy is lost in form of permanent deformation and hole blow-out (Gadallah and Fisher, 2009). In order to reduce this loss of energy and produce seismic waves much more efficiently the shots are sometimes fired in flooded drills. Drilling below the water table and firing the shots in the groundwater would be even more effective.
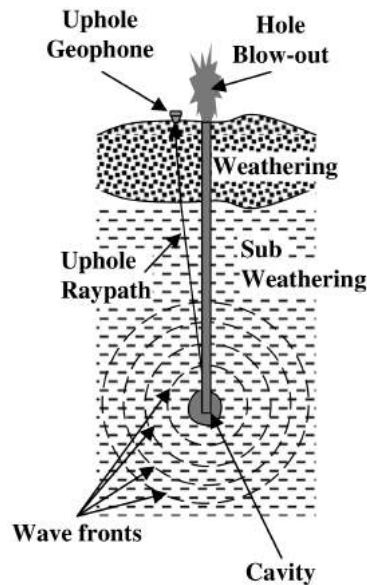
Figure 2.13.: *Operation of an explosive source loaded at the bottom of a borehole (Gadallah and Fisher, 2009)*

---

[25]More information on ANFO (Ammonium Nitrate/Fuel Oil) explosives can be found in (Petri et al., 2010)
[26]A very valuable information used in seismic data processing (Gadallah and Fisher, 2009)

A much safer explosive source than normal gelignite are cord explosives[27]. These explosives can be fed into shot holes produced with metal rods or crowbars driven into the ground (Milsom, 2003). An example for an explosive cord is Geoflex that detonates at a rate of about $6400\,\mathrm{m\,s^{-1}}$. Geoflex is a small but very efficient charge plowed into the ground about $0.5\,\mathrm{m}$ deep in order to attenuate horizontal noise, e.g. ground roll (Gadallah and Fisher, 2009).

2.3.2.2. Impact sources

For small-scale surveys sledgehammers (e.g. $5\,\mathrm{kg}$ in weight) may be used as source. The strength of the hammer stroke, the skill of the performer as well as the ground conditions determine the useful amount of energy that is produced. Sledgehammers provide a suitable source where energy has to travel up to approximately $100\,\mathrm{m}$. Usually the sledgehammer is not aimed at the bare soil, but at a flat plate. The plate is used to stop the sledgehammer abruptly in order to produce a definite and repeatable shot. Thick rubber discs that are less painfully noisy can be used instead of aluminium or steel plates.

Large-scale surveys require more powerful impact sources than common sledgehammers. The large weights of up to several hundreds of kilograms are raised by (portable) hoisting units and then dropped. In practice the weight is dropped from a minimum release height of approximately $4\,\mathrm{m}$. Even if sufficient energy could be achieved by a shorter drop long drops allow the vibrations caused by the rebound of the support (due to the release of the weight) to die away before the impact occurs. Another alternative are weights of approximately $20\,\mathrm{kg}$ to $25\,\mathrm{kg}$ falling in evacuated tubes (Vakimpac). Since the upper surface of the weight is exposed to the air the weight is additionally accelerated by a force of hundreds of kilograms of atmospheric pressure (Milsom, 2003).

2.3.2.3. Vibroseis

By contrast to other controlled seismic sources Vibroseis passes energy into the ground at least for $7\,\mathrm{s}$ instead of trying to deliver energy to the ground within the minimum amount of time (Telford et al., 1990).

Basically, the vibrator is a truck-mounted hydraulic energy source producing a signal that is usually several seconds long (the so-called sweep). The base plates (or pads) are lowered and firmly pressed to the ground. In order to provide an reactive mass the trucks are jacked-up to place the weight of the trucks on the pads. The energy input to the base plates is the mechanical energy converted from hydraulic energy by the vibrator actuator (Gadallah and Fisher, 2009).

Vibroseis produces low-energy density, thus it can be deployed in areas where other source may cause extensive damage. Nowadays Vibroseis is the most popular land seismic source (Telford et al., 1990).

---

[27]Used in quarry blasting to introduce delays into firing sequences (Milsom, 2003)

2.3.3. Natural sources

Natural seismic activity is caused by tectonic and volcanic earthquakes as well as other non-man-made processes on or below the Earth's surface. Due to the increasing human interference with nature in some cases these natural sources may be referred to as man-made. Although man-made, these events cannot be classified as controlled sources since they may trigger larger events getting beyond human control (Bromley and Mongillo, 2008).

2.3.3.1. Earthquakes

Earthquakes are natural sources of seismic waves triggered by a sudden release of a large amount of energy. Nevertheless, earthquakes appear on both sides of the digram shown in Fig. 2.12. Since earthquakes may also arise for example from mining activities, geothermal or fracking projects this kind of classification seems permissible. Approximately 90 % of all earthquakes occur due to tectonic events and the remaining 10 % are associated with volcanism and collapse of subterranean cavities of man-made events(Lowrie, 1997). Hence only a small portion of the overall earthquake activity is caused by mankind and in general earthquakes are referred to as natural events.

Earthquakes are recorded by using the sensors discussed in Sec. 2.2.2. In order to describe how large an earthquake is two methods can be utilized. The intensity of an earthquake describes the severity of its effects on mankind and the environment. Thus it is a subjective parameter that is based on an evaluation of visible effects. By contrast the magnitude is a more objective parameter determined instrumentally. Although it says little about the severity of the ensuing effects the magnitude is widely used to report the size of an earthquake (Lowrie, 1997). Modern earthquake observatories use two or more magnitude scales, all differing from the original Richter scale. It is common practice to measure the P wave amplitude since it is not affected by the focal depth of the earthquake. This P wave magnitude is called m_b and can be used to quantify earthquakes with deep and shallow foci, respectively. For shallow earthquakes the amplitude of the largest swing in the surface wave train is measured too, yielding the surface-wave magnitude M_S (Bolt, 2000).

Nowadays seismologists favour a more physical measure known as the seismic moment M_0. The definition of the moment magnitude M_w is based on the seismic moment via the equation

$$M_w = \frac{2}{3} \log_{10} M_0 - 10.7$$

given by (Aki and Richards, 2002). The moment magnitude is a more appropriate measure for the description of very large earthquakes. In scientific evaluation of earthquake size M_w has largely replaced M_S. However, the surface-wave magnitude is widely used in media reports (Lowrie, 1997).

Elastic rebound theory

The elastic rebound theory was developed by Reid in order to describe the rupture process of a fault causing earthquakes. An illustration of the model is shown in Fig. 2.14 in form of changes to five parallel lines. These lines are drawn perpendicular to the fault (dashed line) and cross it at points A to E (cf. Fig. 2.14 a)). The block on the left side of the fault moves northward, on the right side the movement is southwards as indicated by the double-dashed lines in Fig. 2.14 b). Next to the fault the parallel lines are bent due to this strain, whereas at some distance the lines remain straight and parallel. Obviously the strain cannot grow indefinitely, hence, in terms of Fig. 2.14 c), at point C the breaking point of the crustal rocks is exceeded and a rupture occurs[28] resulting in a violent displacement on the fault plane. Between the blocks next to the fault the relative displacement is a process taking place over several years or even decades. Since on the fault plane itself the same displacement is achieved in a few seconds the strained rocks rebound suddenly and release the accumulated strain energy at their seismic speed. Comparing Fig. 2.14 b) to Fig. 2.14 c) unveils a compression of segments BC and C'D and a dilatation of segments CD and BC'. Since the points furthest away from point C, namely A and E, do not move the strain energy stored at these points is not released. This implies that the fault plane is not entirely displaced but only the region where the breaking point has been exceeded. The magnitude of an earthquake is directly proportional to the length of the activated fault plane (Lowrie, 1997).
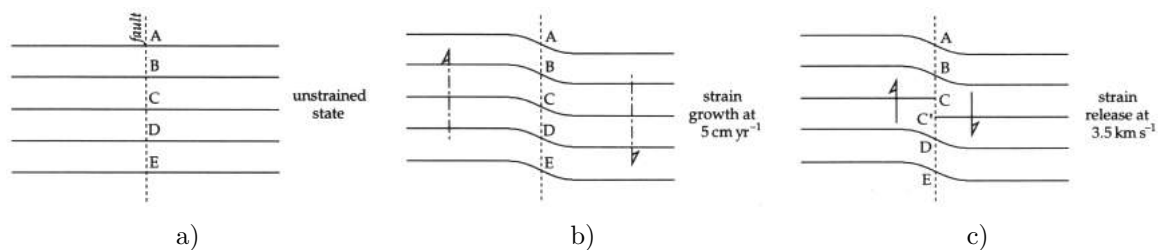
Figure 2.14.: *Elastic rebound model of the origin of earthquakes (Lowrie, 1997):*
a) unstrained state of a fault segment
b) accumulation of strain
c) rebound of strained segment

Anthropogenic earthquakes

According to (Fritschen and Rüter, 2010) possible causes of anthropogenic earthquakes may, for example, be dam construction, tunnel construction, gas and petroleum production, mining or fracking. Like natural earthquakes induced seismic events arise from rupture processes in the bedrock. But instead of being completely determined by the tectonic stress field these events occur mainly due to human activities.

---

[28]Either the rocks next to the point of greatest strain or the weakest rocks break

Human activities may trigger the faulting of a nearby natural tectonic disturbance. In practice, fluid overpressure triggers nearby tectonic faults. Without human impact the natural faulting may occur at a later time or even never. A third possibility is that another tectonic fault is triggered. Intensive monitoring may not be a sufficient method in order to control triggered seismicity since even a fast reaction to an increasing number of microseismic events may be too late (Mulargia and Bizzarri, 2014). Usually the magnitudes associated with anthropogenic earthquakes are smaller than the magnitudes of naturally occurring earthquakes but sometimes may be felt since they occur at shallower depths. In order to detect and localize these weak seismic activities suitable monitoring and evaluation techniques are utilized.

2.3.3.2. Further natural seismic sources

Apart from earthquakes and natural seismic noise (microseisms) further non-man-made sources are, for example, landslides and snow avalanches.

The primary cause of landslides is slope saturation by water. Nevertheless, the seismic activity in mountainous landslide-prone regions may increase the likelihood that landslides occur. The most devastating types of landslides are caused by volcanic activity (Highland, 2004). Low-frequency seismograms indicate that landslides are characterised by a complex source and may be described best as multiple events. Landslides which include the submarine part of a slope may also produce tsunamis (La Rocca et al., 2004). Further analysis of seismograms suggests landslides to be described by at least two distinct seismic sources. The first one corresponds to the initial rupture and is associated by an elastic rebound during the detachment. The other one can be attributed to the rock impact on the slope (Deparis et al., 2008). Rock falls are a specific type of landslide. Seismic signals generated by rock fall events show specific characteristics in the time-domain. Furthermore, the time-frequency evolution of these signals is different from that of other seismogenic sources, e.g. earthquakes and impacts of single rocks (Vilajosana et al., 2008).

Snow avalanches are also known to produce seismic signals. Extensive investigations showed that snow avalanches following identical paths produce similar seismic signals. Thus, a relationship between amplitude, frequency content and wave trains of avalanche-produced seismic signals and the avalanche path exists (Suriñach, Sabot et al., 2000). Based on the running spectra of these seismic signals it is possible to distinguish between avalanches and earthquakes, although they have the same frequency content but a different frequency evolution (Biescas et al., 2003).

Chapter 3

Acoustics

The basic aspects of acoustics discussed in this chapter are based on (Kuttruff, 2007). Acoustics is the science of sound investigating the origin of sound and its propagation. The field may subdivided based on the medium in which the sound propagates and on the sound frequency. The present thesis mainly deals with sound propagating in air[1] within the frequency range of human hearing (16 Hz to 20 000 Hz).

3.1. Fundamentals of acoustics

A sound wave propagating in a medium causes displacements of particles within this medium. This displacement can be specified by the displacement vector $\mathbf{s}\,(\xi, \mu, \zeta)$. Consider sound propagation in a fluid (either a gas or a liquid). The non-synchronous motions of neighbouring particles cause deformations consisting of local compressions and dilatations. Thus the variation of the density $\Delta\rho$ is found as an acoustical variable. A change of fluid density is accompanied by a change of the pressure in the fluid Δp. With p_0 and ρ_0 denoting the pressure and density values for a medium at rest the total pressure and density are $p = p_0 + \Delta p$ and $\rho = \rho_0 + \Delta\rho$, respectively. The pressure variation is called the sound pressure (measured in Pa) and is of particular interest since it is accessible to direct measurements.

The differential equation

$$\boldsymbol{\nabla}^2 p\,(\mathbf{x}, t) = \frac{1}{c^2} \frac{\partial^2 p\,(\mathbf{x}, t)}{\partial t^2} \tag{3.1}$$

is known as the acoustical wave equation where c denotes the speed of sound. Eq. 3.1 must not only be satisfied by the sound pressure but also by all other acoustical variables. Since the propagation medium is considered to be a fluid the second Lamé constant μ is zero. As a consequence, acoustic signals propagate through the air in form of compressional waves travelling at the speed of sound and the particle motion occurs only in the direction of wave propagation.

---

[1]Or more generally, in gases

The speed of sound c is solely dependent on the first Lamé constant and can be written as

$$c = \left(\frac{\lambda + 2 \cdot 0}{\rho}\right)^{1/2} = \left(\frac{\lambda}{\rho}\right)^{1/2} \tag{3.2}$$

A more common computation method for the speed of sound is given subsequently.

3.1.1. Speed of sound

This section follows the equations used to quantify the temperature and humidity dependence of the speed of sound presented in (Bohn, 1988).

In an ideal gas the speed of sound c is

$$c = \left(\frac{\gamma P}{\rho}\right)^{1/2} \tag{3.3}$$

where P is the ambient pressure, ρ the gas density and γ the ratio of the specific heat of gas at constant pressure to that at constant volume. Dry air mostly consists of diatomic molecules and thus is called a diatomic gas. Since diatomic gases have five degrees of freedom ($d = 5$) the equation for the specific heat ratio

$$\gamma = \frac{d+2}{d} \tag{3.4}$$

yields $\gamma = 1.4$ for dry air. Substituting for γ in Eq. 3.3 gives an experimentally verified value for the speed of sound in dry of $c = 331.45 \pm 0.05\,\mathrm{m\,s^{-1}}$. This value holds for audio frequencies, at $0\,°\mathrm{C}$ and $1.013\,25 \times 10^5\,\mathrm{Pa}$ with $0.03\,\mathrm{mol-\%}$ of carbon dioxide. With the equation of state of an ideal gas ($PV = RT$) and the definition of the density ρ as the mass per unit volume Eq. 3.3 can be written as

$$c = \left(\frac{\gamma R T}{M}\right)^{1/2} \tag{3.5}$$

R denotes the universal gas constant ($R = 8.31\,\mathrm{N\,m\,mol^{-1}\,K}$), T is the absolute temperature and M the mean molecular weight of the gas at sea level. This equation shows the pressure independence of the speed of sound. Since R and M are constants the speed of sound has a first order dependence on temperature

$$c = C_0 \left(1 + \frac{t}{273.16}\right)^{1/2} \tag{3.6}$$

with C_0 being the reference speed of sound under defined conditions ($C_0 = 331.45\,\mathrm{m\,s^{-1}}$) and t is the temperature given in $°\mathrm{C}$.

Besides the air temperature moisture affects the speed of sound in air. The density of moist air is lower than the one of dry air and thus according to Eq. 3.3 the speed of sound increases. A decreasing specific-heat ratio due to moisture would cause the speed of sound to decrease. Since the decrease in density dominates the speed of sound increases with increasing moisture.

Eq. 3.5 is correct for dry air. In order to accurately include the effects of moisture the specific heat ratio γ and M of different types of molecules in the air have to be modified, whereas R and T remain unchanged.

For wet air the average number of degrees of freedom per molecule increases to $d = h + 5$ where h denotes the water molecule fraction. Substituting for d in Eq. 3.4 gives the specific heat ratio for wet air

$$\gamma_w = \frac{h + 7}{h + 5} \tag{3.7}$$

The water molecule fraction is given by

$$h = \frac{0.01 f e(t)}{p} \tag{3.8}$$

where f is the relative humidity measured in %, $e(t)$ is the water vapor pressure at temperature t and p denotes the ambient pressure. While f needs to be measured and $p = 1.013 \times 10^5 \, \text{Pa}$ for $1 \, \text{atm}$ reference pressure, $e(t)$ can be retrieved via

$$e(t) = 610.5 \cdot 10 \exp\left(\frac{7.5t}{237.3 + t}\right) \tag{3.9}$$

Table 3.1.: *Composition of dry air*

Type of gas	Percentage [%]	Molecular weight
Nitrogen	78	28
Oxygen	21	32
Argon	1	40

The modification of the mean molecular weight M still needs to be done. The composition of dry air is summarized in Tab. 3.1. By using these values for the mean molecular weight of dry air follows

$$M_d = 0.78 \cdot 28 + 0.21 \cdot 32 + 0.01 \cdot 40 = 28.96 \approx 29$$

Considering the water's molecular weight of 18 the (total) mean molecular weight decreases by

$$M_w = 29 - (29 - 18) \, h = 29 - 11h$$

With γ_w and M_w Eq. 3.5 can be rewritten to be valid for wet air

$$c = \left(\frac{\gamma_w R T}{M_w} \right)^{1/2} \tag{3.10}$$

The separately examined effects of temperature and moisture on the speed of sound can be summed in order to show the total effect (see Tab. 3.2).

Table 3.2.: *Increase of the speed of sound due to the combined influence of temperature and humidity expressed in %*

Temperature [°C]	Relative humidity [%]					
	0	30	40	50	80	100
5	0.91	0.952	0.966	0.980	1.02	1.05
10	1.81	1.87	1.89	1.91	1.97	2.01
15	2.71	2.79	2.82	2.85	2.93	2.98
20	3.60	3.71	3.75	3.79	3.90	3.98
30	5.35	5.55	5.62	5.69	5.90	6.03
40	7.07	7.43	7.54	7.66	8.03	8.27

3.1.2. Doppler effect

If the sound source and the observer are moving with respect to each other a change in frequency occurs. This phenomenon is an everyday observation and is known as the Doppler[2] effect.
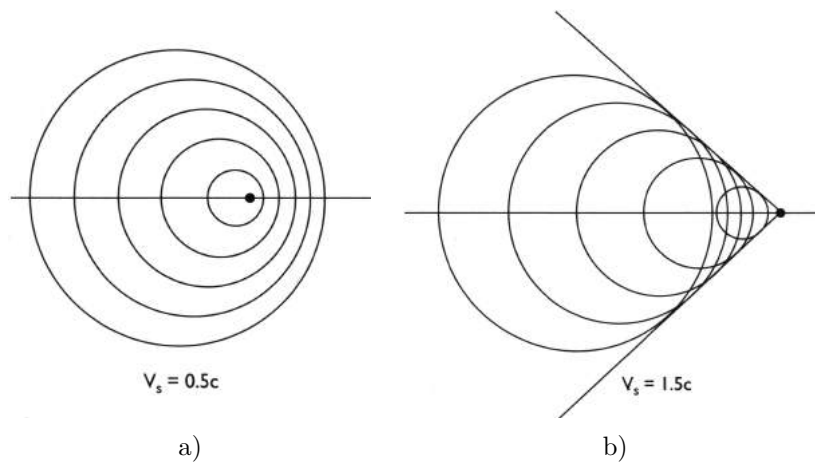
Figure 3.1.: *Moving point source (Kuttruff, 2007):*
a) $V_s < c$
b) $V_s > c$

---

[2]Christian Andreas Doppler (1803-1853) Austrian mathematician and physicist

A sound source in form of a point source at rest emits concentric spherical wave fronts. For a moving point source the emitted wavefronts are also spherical, but asymmetrically arranged as depicted in Fig. 3.1 a). Consider the time interval between the emission of two subsequent pressure maxima (marked by the circles in the illustration) to be the period T. The source moves the distance given by $V_s T$ during the time interval T, where V_s is the speed of the sound source. On the right side of the figure the spatial distance between two wavefronts drops and thus the wavelength is reduced to

$$\lambda' = (c - V_s)\, T$$

This yields an increase of the sound frequency on the right given by

$$f' = \frac{f}{1 - V_s/c} \tag{3.11}$$

The speed of the sound source is negative if the source moves away from the observer. In this case the observer is to the left hand side of the source in Fig. 3.1 a) and Eq. 3.11 yields a decreased frequency. Examples may be a motor vehicle passing the observer or a airplane flying over the observer, respectively. In the case of the motor vehicle the pitch of the sound falls noticeably in the moment of the passing, whereas the pitch continously decreases in the case of the airplane. For a sound source moving at supersonic speed it applies $V_s > c$ and thus it is overtaking the wavefronts it emits (cf. Fig 3.1 b)). The envelope of the circles consists of a cone with an aperture given by the angle α with

$$\sin \frac{\alpha}{2} = \frac{c}{V_s} \tag{3.12}$$

The emitted sound field is limited by the boundaries of the cone which moves with the speed of the sound source V_s from left to right. This kind of Doppler effect (moving source and an observer at rest) applies to the phenomena recorded during the in-situ experiments (cf. Sec. 6).

In the opposite case the observer is moving with the speed V_r towards a sound source at rest. Since the observer is moving with respect to both, the source and the medium, this case is not equivalent to the situation descibed above. It may be described via a sound source embedded in a medium flowing towards the resting observer with the speed V_r. Thus the speed at which the wavefronts arrive at the observer is the sum of the speed of sound and the flow velocity of the medium yielding a frequency

$$f' = \frac{c + V_r}{\lambda}$$

Substituting for the wavelength $\lambda = c/f$ gives the frequency experienced by the resting observer or, equivalently, by a observer moving towards the stationary source while the medium is at rest

$$f' = \left(1 + \frac{V_r}{c}\right) f \qquad (3.13)$$

3.2. Microphones

Microphones are sensors capable of converting pressure variations into electrical signals. Due to the variety of different types of microphones the main subject of this section is to describe microphones used to record airborne sound in the range of audible sounds.

3.2.1. Mechanical principles of microphones for airborne sound

The performance of an microphone can be quantified by several characteristic features. The first one is the sensitivity defined (for pressure microphones) as the ratio of the open-circuit voltage to the applied sound pressure and measured in units of $\mathrm{V\,Pa^{-1}}$ or $\mathrm{mV\,Pa^{-1}}$, respectively. The frequency dependence of the sensitivity is another characteristic feature. Ideally the sensitivity is constant within a certain limited frequency range. The third feature is the directivity of a microphone which is important for practical applications.
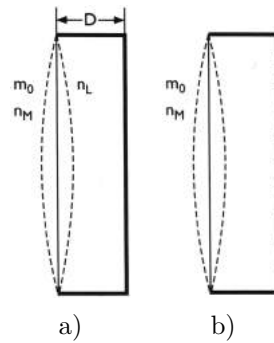
Figure 3.2.: *Schematic illustration of microphone capsules (Kuttruff, 2007):*
a) closed
b) perforated rear side

For the discussion of the behaviour of a microphone in the sound field its dimensions are assumed to be small compared to the acoustical wavelengths. From the mechanical point of view a microphone for airborne sound consists of a small box with a diaphragm forming one side of this box as sketched in Fig. 3.2 a). For a first examination the box is considered to be tightly closed and the air within to be at atmospheric pressure. A sound wave causes a deviation p from the static pressure p_0 and the force $F = Sp$ acts on the diaphragm, with S denoting the area of the diaphragm.

Depending on the sign of the pressure the diaphragm is deformed inward or outward. The resonant frequency of such a system is

$$\omega_0 = \frac{1}{(m_0 n_0)^{1/2}} \tag{3.14}$$

where m_0 is the mass of the diaphragm and n_0 the total compliance. With the frictional resistance[3] r the mechanical input impedance of the capsule can be written as

$$Z_m = \frac{F}{j\omega\xi} + j\left(\omega m_0 - \frac{1}{\omega n_0}\right) \tag{3.15}$$

If $\omega \ll \omega_0$ the frictional resistance and the mass term $j\omega m_0$ in Eq. 3.15 can be neglected and the elongation of the diaphragm ξ is

$$\xi = n_0 S \cdot p \tag{3.16}$$

In this frequency range the system is referred to as a pressure receiver.

Fig. 3.2 b) illustrates a box with a perforated rear side. The inner side of the diaphragm is exposed to the same pressure as the rear side of the box and hence the force acting on the diaphragm is

$$F = S\Delta p \approx S\frac{\partial p}{\partial x}D \tag{3.17}$$

where Δp is the pressure difference between the two sides of the box, D the thickness of the box and $\partial p/\partial x$ the pressure gradient in the sound field in the x-direction. Due to the perforation the air is no longer enclosed in the capsule and loses its restoring force causing the diaphragm to be less stiff. Assuming $\omega \ll \omega_0$ the elongation of the diaphragm is now

$$\xi = n_0 F = n_0 SD \cdot \frac{\partial p}{\partial x} \tag{3.18}$$

This system is sensitive to the gradient of the sound pressure. A single plane wave arriving at the diaphragm under an angle θ is given by

$$p(x, y) = \hat{p}e^{-jk(x\cos\theta + y\sin\theta)}$$

and the gradient of the sound pressure at the capsule ($x = y = 0$) is

$$\frac{\partial p}{\partial x} = -jkp \cdot \cos\theta \tag{3.19}$$

---

[3]Represents all mechanical losses due to radiation etc.

Substitution into Eq. 3.18 yields

$$\xi = -jkn_0 SD \cdot p \cdot \cos\theta \qquad (3.20)$$

Form this equation the essential features of a gradient receiver can be deduced, namely the increase of the diaphragm elongation with the angular frequency $\omega = ck$ and the dependence on the angle of incidence θ.

If the openings in the rear are long and narrow the frequency dependence of the pressure sensitivity vanishes. In this case the diaphragm elongation is controlled by the flow resistance r which the air experiences when it is forced through the openings and is written

$$\xi = -\frac{SD}{cr} \cdot p \cdot \cos\theta \qquad (3.21)$$

3.2.2. Condenser microphones

In order to become a microphone the system diaphragm plus capsule discussed in the previous section must be combined with an electroacoustic transducer that takes up the membrane motion.

Converting acoustic signals into electrical signals can be achieved by placing a metal plate inside the capsule, parallel to the diaphragm (cf. Fig. 3.3 a)). In combination with the membrane it forms a parallel-plate capacitor and the resultant system behaves like an electrostatic transducer.
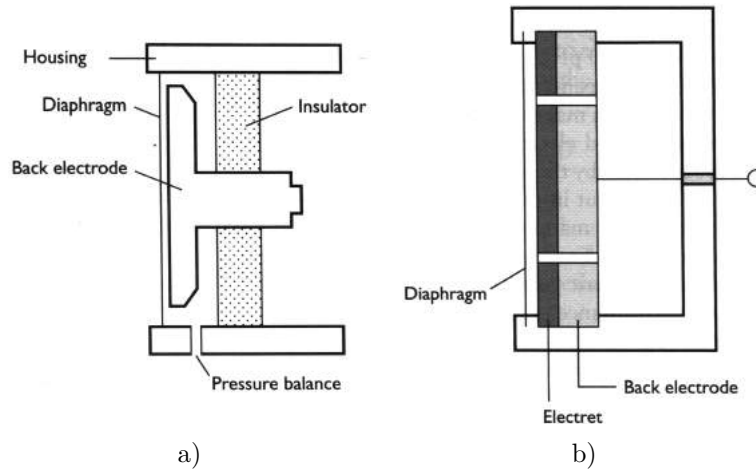
Figure 3.3.: *Schematic illustration of a(Kuttruff, 2007):*
a) condenser microphone
b) electret microphone

In closed box conditions the condenser microphone detects the diaphragm elongation ξ that is proportional to the pressure (with Eq. 3.16)

$$U_{I=0} = \frac{n_0 U_0 S}{d} \cdot p \tag{3.22}$$

For low frequencies ($\omega \ll \omega_0$) the microphone is a pressure receiver with frequency-independent sensitivity.

For a perforated rear side of the capsule Eq. 3.18 is considered and the resultant voltage is

$$U_{I=0} = \frac{n_0 U_0 S D}{d} \cdot \frac{\partial p}{\partial x} \tag{3.23}$$

As a consequence the microphone is referred to as pressure gradient sensor. A typical example of an condenser microphone is shown in Fig. 3.3 a).

Nevertheless, another type, the so-called electret microphone (invented by Sessler[4] and West[5]), is eminent for this thesis. This type of sensor operates without a bias voltage applied to the system. The polarising field U_0/d (see. Eq. 3.22 and Eq. 3.23) is created by an electret. The electret is very similar to a magnet. While a magnet carries a magnetic polarisation the electret carries a permanent electrical polarisation. Partially filling the space between two electrodes of a parallel-plate capacitor with an electret material[6] gives rise to an permanent electrical field in the empty space. For practical usage two main types of electret microphones bear a meaning. In the first one the diaphragm of the microphone is formed from a thin metallised electret foil. The second type is sketched in Fig. 3.3 b). In this case the electret material is placed on the backplate of the condenser microphone.

Electret microphone come in different sizes and forms. Due to their relatively low price and their small size they are widely used for recording sounds.

---

[4]Gerhard Martin Sessler (1931-) German inventor and scientist
[5]James Edward Maceo West (1931-) American inventor and acoustician
[6]Suitable polarized polymers

4

Ground motion induced by seismic and acoustic sources

In this chapter an alternative source classification is introduced that forms the basis for finding appropriate classification criteria. Based on the proposed criteria the basic experiment design is outlined and the required and/or available equipment is described.

4.1. Source types

As discussed in Sec. 2.3 a multitude of seismic sources exists. In order to be able to establish a classification procedure relying on seismic and acoustic data it is necessary to define rather general source classes/types which still cover the majority of the known seismic sources. Basically, five source types producing signals that can be detected by seismic sensors are distinguished. Schematic sketches describing the basic ray paths for each source type are shown subsequently. These sketches use a star as symbol for a signal source and a black triangle to depict the sensor site. If the star symbol is surrounded by three thin circles the source is considered to emit acoustic signals, too. The signals propagating through the air and the subsurface are recorded with acoustic and seismic sensors, respectively. The ray paths are illustrated with different thickness in order to emphasize if the main excitation has to be expected for the acoustic or the seismic part of the produced signal.

As shown in Fig. 4.1 signals produced by a high altitude acoustic source reach the sensor site by propagating through the air. Although no seismic signals may be induced directly below the source the pressure variations in the air may cause ground motions at the sensor site that are detectable by the seismic sensor. Hence, seismic and acoustic data comprising signals associated with this source type may bear high resemblance in the time-domain as well as in the frequency-domain.
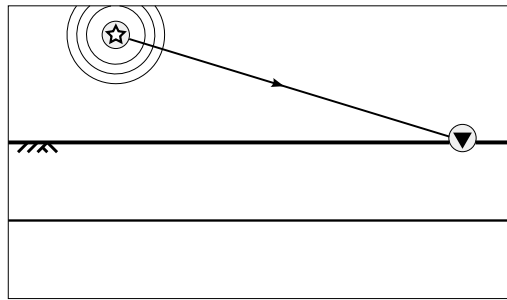
Figure 4.1.: *Basic ray paths in the case of a high altitude acoustic source for a simple two-layer subsurface model*

As can be seen from Fig. 4.2 the signals produced by a low altitude acoustic source mainly propagate through the air. Nevertheless, the pressure variations in the air caused by the source may induce seismic signals directly below the source. Hence, apart from ground motions described for the high altitude source also seismic signals that propagated through the subsurface may be detected by the seismic sensor at the sensor site.
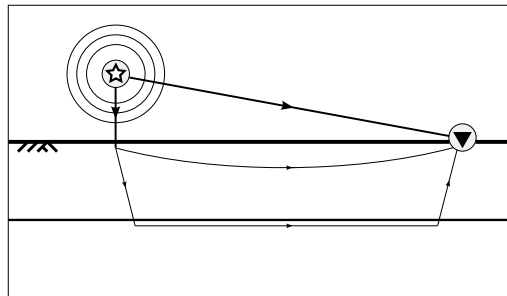
Figure 4.2.: *Basic ray paths in the case of a low altitude acoustic source for a simple two-layer subsurface model*

A seismic-acoustic surface source produces both, seismic and acoustic signals (cf. Fig. 4.3). As indicated by the ray path thickness the produced signals equally propagate through the ground and the air, respectively. The recorded seismic signals can comprise different wave phases that may be distinguishable. Hence, the waveforms associated with this source type may be differently shaped in the seismic and acoustic data. Note that this source type describes the surface source most commonly used in small scale seismic surveys, namely a hammer in combination with a plate.

Another type of seismic surface source that ideally would emit no sound at all is shown in Fig. 4.4. In practice, every seismic surface source produces at least a small amount of acoustic noise. Hence, the signals produced by this source type mainly propagate through the subsurface while only a small portion reaches the sensor site through the air. The signal characteristics described above apply for this surface source type, too.
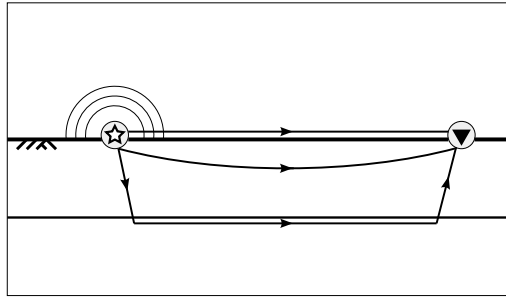
Figure 4.3.: *Basic ray paths in the case of a seismic surface source producing ambient acoustic noise for a simple two-layer subsurface model*
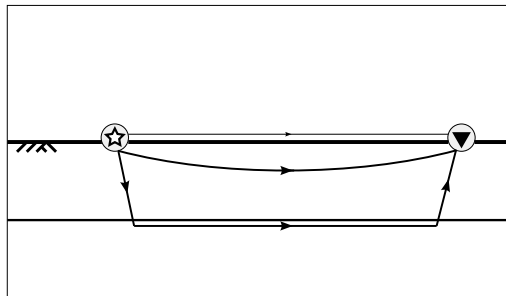
Figure 4.4.: *Basic ray paths in the case of a seismic surface source for a simple two-layer subsurface model*
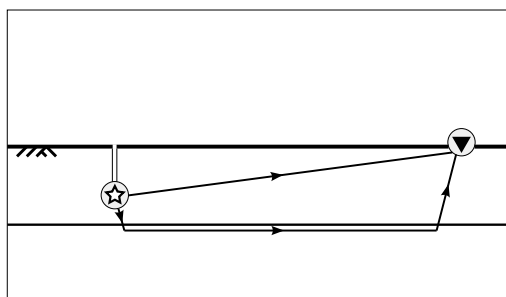
Figure 4.5.: *Basic ray paths in the case of a seismic subsurface source noise for a simple two-layer subsurface model*

As shown in Fig. 4.5 a seismic subsurface source is assumed to emit no acoustic signals. The produced signals reach the sensor site only by propagating through the subsurface since this source type causes no excitation of pressure variations in the air.

From this considerations it seems permissible to state a dependency of the amplitude sizes in seismic and acoustic data on the source type. Source types mainly producing acoustic signals may cause higher amplitudes in the acoustic data than in the seismic data. A reversed behaviour may be found for source types that mainly produce seismic signals. Hence, measuring the amplitudes of the seismic and the acoustic signals and computing the ratio may provide a time-domain criterion that supports the identification of source types.

It is assumed that the frequency content of signals produced by an acoustic source is reproduced in a similar way in both, the seismic and acoustic data. By contrast, for a signal produced by a seismic source the frequency content of the different sensor data is assumed to bear small or even no resemblance. As a result, the correlation of frequency-domain representations of seismic and acoustic data sets may be another criterion to indicate the source type. Following the nomenclature of the present thesis this criterion is hereinafter denoted as the amplitude spectrum similarity (ASS).

Since different seismic wave types propagate at different velocities this parameter may also provide information on the source that produced the investigated signal. Discriminating different source types can be achieved by comparing the velocity computed from the seismic data and the one computed from the acoustic data.

4.2. Experiment design

Based on the defined source types and the assumed classification criteria an experiment has to be defined that forms the basis for the verification of the assumptions made above.

The primary purpose of the experiment is to produce data which can be used to verify whether and to what extent the criteria described in Sec. 4.1 can support the identification of source types. Additionally, the experiment should verify the capabilities of sensor arrays and three component seismic sensors. All in all, the experiment is carried out to obtain a better understanding of the relation between seismic and acoustic signals in order to establish an easy-to-use and reliable procedure for the classification of signal sources.

The experiment design is dependent on the classification criteria and source types discussed in Sec. 4.1. Since all criteria rely on the comparison of seismic and acoustic data the monitoring site has to be equipped with both, seismic sensors (geophones) and acoustic sensors (microphones). By simultaneously recording seismic and acoustic signals two criteria, namely the amplitude ratio and the amplitude spectrum similarity can be computed.

The third criterion requires the velocity of different signal types to be determined. Hence, instead of using only a single seismic and acoustic sensor, sensor arrays have to be installed at the monitoring site. Since the usability and capability of sensor arrays with a high number of array stations and large spatial extent are well known this experiment utilises minimal array installations. Thus, three seismic and acoustic sensors should be deployed in form of equilateral triangles forming minimal sensor arrays with identical positions. Using at least one 3C-geophone provides the possibility to investigate the particle motions associated with the recorded signals.

The source types described in the previous section need to be implemented as controlled sources. In order to produce a sufficiently large data set each of the controlled sources should be applied at least three times at one location. In order to verify the capability of a minimal array layout the controlled sources have to be applied at multiple shot points around the array.

As already discussed in Sec. 3.1.1 the speed of sound is subject to variations related to the temperature and the relative humidity. Thus, these meteorological quantities should be also measured at the monitoring site.

4.3. Equipment

Subsequently the equipment used for the realisation of an experiment is described. The selection of the equipment relies on the experiment design given above and the components that were actually available for usage. Theoretical basics concerning the sensor components can be found in Sec. 2.2 (seismic sensors) and Sec. 3.2 (acoustic sensors). The equipment used for the implementation of the experiment at the Knödelhütte is shown in Fig. 4.6. Except for the tools used for signal generation (hammer, plate) the equipment is identical for the Altlengbach experiment.

4.3.1. Signal generation

The controlled seismic sources described in this section are used in order to produce data that contains seismic, acoustic and mixed signals.

As discussed in Sec. 2.3.2 impact sources are a common type of seismic sources. In particular hammers are a convenient source for small scale seismic surveys. Thus, the hammer (see. Fig. 4.6) is traditionally used as a pure seismic source. Within this experiment the hammer is aimed at bare soil and at a metal plate. Aiming the hammer at a plate is common practice in seismic surveys since a definite and repeatable shot is produced. In terms of this experiment the hammer aimed at bare soil is denoted as a seismic surface source. Besides ground movement a hammer stroke on a metal plate also causes a strong acoustic signal. Hence, the combination of hammer and plate is addressed as a seismic-acoustic surface source.

Figure 4.6.: *Equipment used for the in-situ experiment at the Knödelhütte (Vienna)*

A pure acoustic signal is produced by using a 26 " orchestra drum similar to the one shown in Fig. 4.7. In order to suppress the transmission of vibrations of the drum body into the ground the drum itself must not touch the ground. Therefore the drum has to be suspended approximately 50 cm above the Earth's surface during the excitation.

Since a high altitude acoustic source and a subsurface source cannot be implemented without extensive effort these source types are not considered to contribute to the experiment as controlled sources.

Figure 4.7.: *26 " orchestra drum used for producing acoustic signals*

A summary of the signal sources that should be used in the experiment is provided in Tab. 4.1.

Table 4.1.: *Seismic and acoustic sources used for signal generation*

Source	Source type	Abbreviation
Hammer	seismic	H
Hammer + Plate	seismic-acoustic	HP
Drum	acoustic	D

4.3.2. Data recording

Digitizing and recording of the produced signals is accomplished by using REF TEK 130S seismic recorders. The REF TEK 130S DAS units are rugged (protection class IP67), portable, and versatile data recorders that can be reconfigured for various types of applications. The used 130S DAS units incorporate two 24-bit delta sigma type analog-to-digital converter boards providing a total of six channels per unit. Digitized data are written in PASSCAL file format on two compact flash (CF) disks. The 130S recorder uses both a high-precision TCXO[1] and an external reference provided by the GNSS[2] receiver that uses GPS[3] for time, frequency, and position reference. Hence accurate timing to better than $10\,\mu s$ can be maintained over a long period (*REF TEK 130S Users Guide* 2014).

For the experiments two REF TEK 130S seismic recorders can be utilised.

4.3.3. Ground motion detection

Ground motion is detected with Geospace GS11D $4.5\,Hz$ geophones with a damping of $70\,\%$ and a coil resistance of $4000\,\Omega$. The corresponding frequency response curve in Fig. 4.8 is indicated with a *C*. For field operation three GS11D geophones are installed in the waterproof GS-3C triaxial land case that has three 3″ spikes to assure secure ground coupling. Each geophone is associated with either the North-South, East-West, or Up-Down direction.

The largest cable length available for experiments is $10\,m$. Since two REF TEK 130S DAS units can be used for the experiments the spatial extent of the geophone array is limited to a lateral length corresponding to the cable length of the 3C-geophones.

---

[1]Temperature Compensated Crystal Oscillator
[2]Global Navigation Satellite System
[3]Global Positioning System
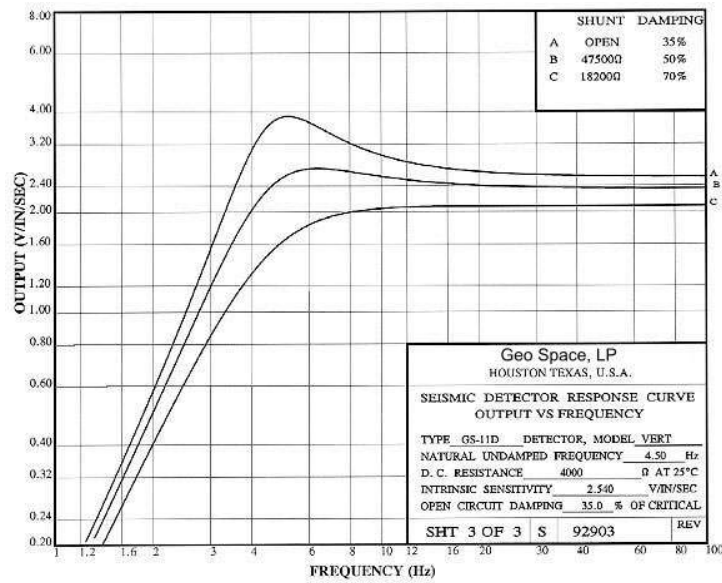
Figure 4.8.: *Frequency response curcve of the Geospace GS11D* 4.5 Hz *geophone (taken from* `http://www.geospace.com/tag/gs-11d/`

4.3.4. Sound detection

For the sound measurements low-cost self-made microphones are used. Core element is the Kingstate KECG2738PBJ-A electret condenser electret microphone with a basic frequency range of 20 Hz to 20 000 Hz (cf. Fig. 4.9). The microphone circuitry diagrams published by the VEMG[4]
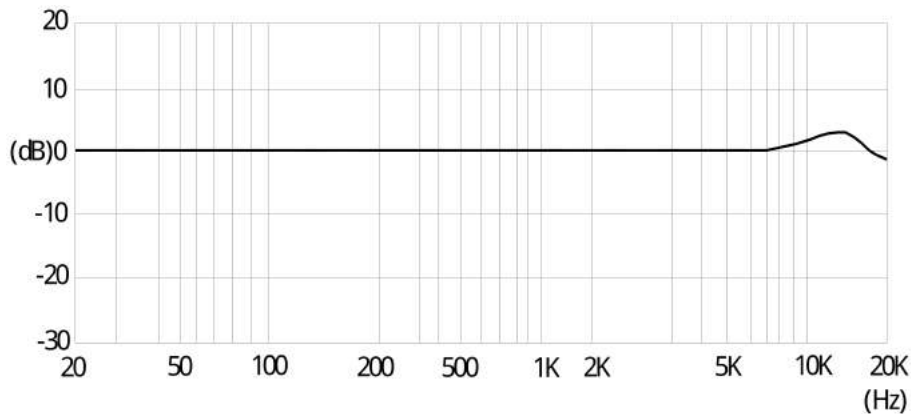
Figure 4.9.: *Frequency response curve of the Kingstate condenser electret microphone*

at the University of New Hampshire[5] were the main input for the construction of the microphones used in this study. The final DIY microphones are based on the Basic J1 microphone that has been successfully deployed at various volcanoes.

---

[4]Volcanic Eruption Modeling Group

[5]`http://volcanomodels.sr.unh.edu/jbj/MICROPHONES/microphone_list.html`

The corresponding modified circuitry diagram is shown in Fig. 4.10.
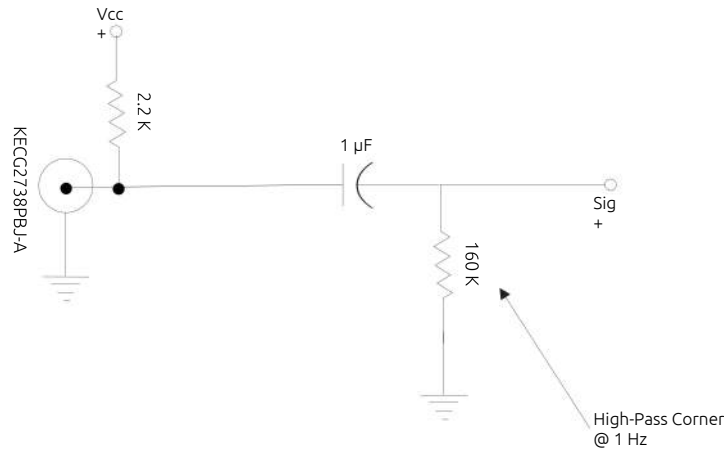
Figure 4.10.: *Circuitry diagram of the microphone used in this study*

Note that the acoustic sensor should be placed near the surface in an upright position in order to avoid that one specific direction is privileged. The microphone array is installed with the same lateral length as the geophone array.

4.3.5. Annotations

The seismic and acoustic sensors introduced above measure different physical quantities. The geophone measures the velocity of the displacement whereas the microphone detects the sound pressure. As a consequence, assumptions have to be made with regard to the comparison of the different sensor data.

As already mentioned in this chapter, the amplitude ratio of seismic and acoustic data may be a possibility to identify the source type that produced the signal. The signal amplitudes in the recorded data are given in the non-physical unit counts. With the known sensitivity of the used sensors it is possible to convert counts into physical units. In the case of the geophone the resultant unit would be $\mathrm{m\,s^{-1}}$. For the sound pressure the conversion would yield Pa or dB, respectively. In order to be able to compare signal amplitudes with different units a further conversion of the sound pressure unit is necessary. Converting the sound pressure to displacement (and subsequently to the velocity of the displacement) requires knowledge on how the ground reacts to sound pressure variations. Dissimilar reactions of different types of ground (e.g. lawn and bare, compact soil) are assumed. As a consequence the relation between sound pressure variations and ground displacement requires extensive empirical research that would go beyond the scope of the present thesis. Hence, the proposed amplitude ratio is not an absolute measure but is dependent on the used equipment and the ground conditions at the experiment site. By this means, the signal amplitude comparison carried out within this thesis yields a relative dimensionless amplitude ratio.

Similar considerations have to be made with regard to the amplitude spectra of the different sensor types. An illustrative example as well as the consequences are discussed in Sec. 6.2.2.2.

Chapter 5

Data analysis techniques

This chapter provides information on and descriptions of the techniques used for processing and analysing the data, respectively. The visualisations were generated by using synthetic data similar to the data expected from the in-situ experiments. The modules presented subsequently were developed by using the Python programming language. For common scientific computing and visualisation tasks the Python-based open-source software ecosystem SciPy was used (Jones et al., 2001–). The core packages of SciPy most frequently used in this study are NumPy (base N-dimensional array package), Matplotlib (Hunter, 2007) and the SciPy library. Seismology specific data handling, standard data processing as well as some more sophisticated processing tasks were accomplished with the ObsPy package (Beyreuther et al., 2010).

5.1. Synthetic data

In order to demonstrate the capabilities of data analysis techniques it is necessary to provide synthetic sample data. The synthetic signal should bear resemblance to real on-site recorded data produced by a controlled source. For instance a basic pulse is given by Eq. 5.1 (modified after (Almendros et al., 1999)). This equation offers a high degree of customization by variation of the parameters B, t_0 and f_0.

$$S(t) = \left(\frac{t}{t_0}\right)^B \exp\left(-\frac{t}{t_0}\right) \sin\left(2\pi f_0 t\right) \tag{5.1}$$

A synthetic signal with natural appearance as shown in Fig. 5.1 is generated by combining three basic pulses with different parameter settings. The values assigned to these parameters for each signal component are summarized in Tab. 5.1. The cyan coloured line in Fig. 5.1 represents the envelope of the synthetic signal. It clearly delineates the three main phases of the signal. By applying different filter types to the data the resultant envelope can be customised.
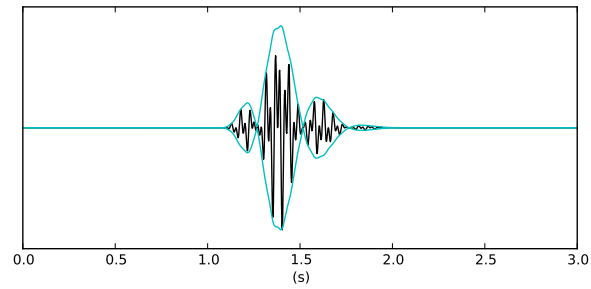
Figure 5.1.: *Synthetic signal generated from a combination of three basic pulses with different parameter settings:*
black ... synthetic pulse
cyan ... envelope

Table 5.1.: *Paramter values used for the generation of a synthetic signal*

Parameter	Cmp1	Cmp2	Cmp3	Unit
B	2	4	1	[ ]
t_0	0.15	0.15	0.15	s
f_0	11	29	2	Hz

The envelope of a signal is computed by adding the squared amplitudes of the signal itself and it's Hilbert transform and then taking the square root (Kanasewich, 1981).

In the time domain the transform is

$$\tilde{x}(t) = \text{HT}[x(t)] = \frac{1}{\pi}\text{pp}\left\{\frac{1}{t}\right\} = \frac{1}{\pi}\text{pv}\left\{\int_{-\infty}^{+\infty}\frac{x(s)}{t-s}ds\right\} \tag{5.2}$$

where pv and pp are the abbreviations of principle value[1] and principle part[2], respectively. Thus, the envelope is written as

$$e(t) = \left[x^2(t) + \tilde{x}^2(t)\right]^{1/2} \tag{5.3}$$

and represents a instantaneous measurement of the amplitude of the signal $x(t)$. In the past, a major advantage of computing envelopes was the significantly lower memory requirement for seismic section displays[3]. Another advantage that is still important for seismic data analysis is the disregard of the sign or the phase of the events and the emphasising of strong events (Mari et al., 1999).

---

[1] The principle value integration is the limit of the sum of two integrals from $-\infty$ to $-\epsilon$ and from ϵ to $+\infty$ as ϵ tends to zero (to exclude the point $s=0$)

[2] The integration of the convolution is done as a principle value

[3] Nowadays a less critical factor

5.2. Standard data-visualisation and spectrogram

The processing module described in this section is a combination of a mere visualisation tool and a standard analysis tool.

The upper plot in Fig. 5.2 shows the generated example data consisting of three single pulses. The lower plot of the figure is the spectrogram computed for the data and shows the frequency content of the data with respect to time. Time-domain representation and spectrogram for the synthetic data with added noise are shown in Fig. 5.3. Despite a higher noise level the base frequencies of the signal are still clearly visible.
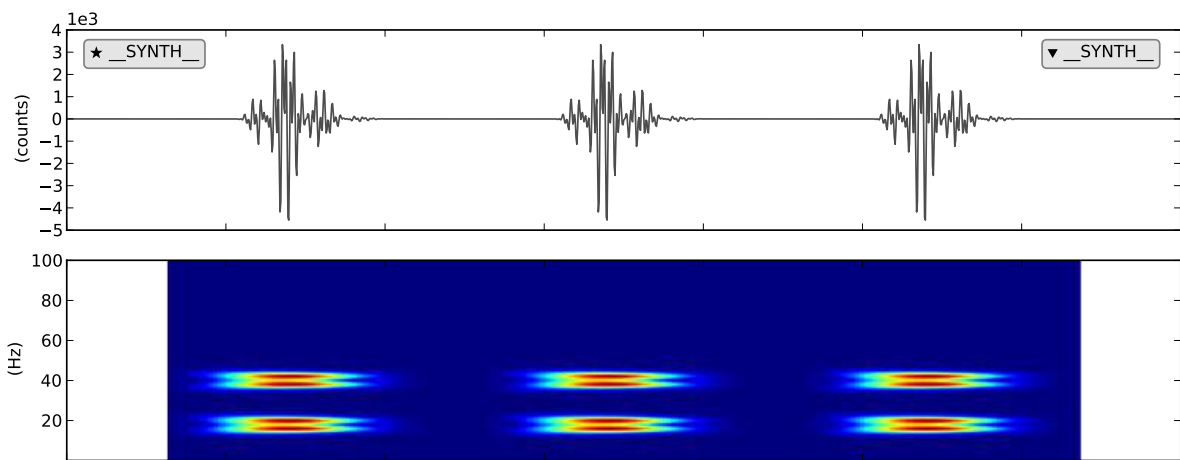
Figure 5.2.: *Combined visualization of the synthetic data and the corresponding spectrogram*
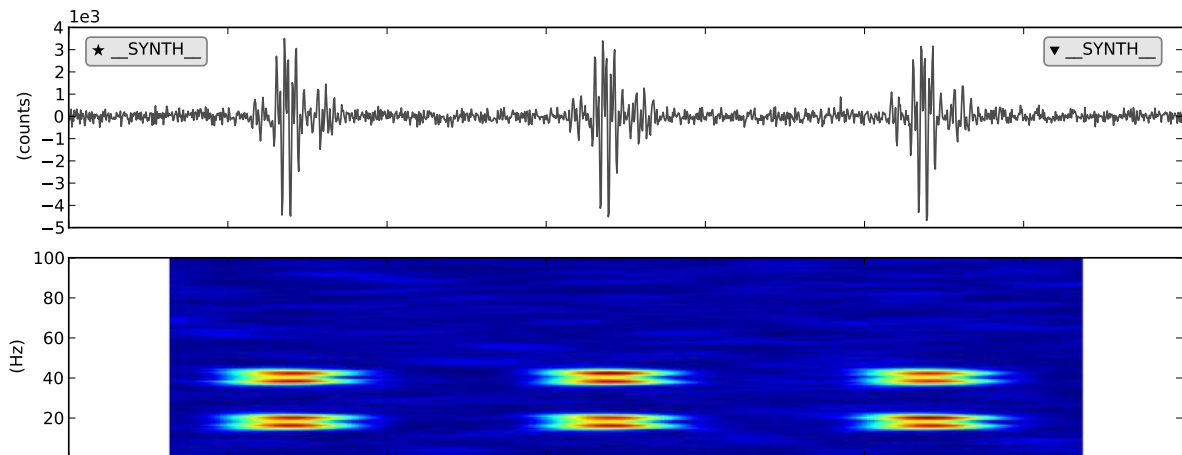
Figure 5.3.: *Combined visualization of the synthetic data with added noise and the corresponding spectrogram*

This module offers the possibility to gain information on the signal characteristics. From the spectrogram the time-dependent behaviour of the frequency content of a recorded signal can be deduced.

5.3. Amplitude spectra

Although the spectrogram provides information on the frequency content of a signal, in some cases a non-time-dependent representation is needed. The frequency spectrum of a time-domain signal can be obtained by computing the one-dimensional discrete Fourier[4] Transform (DFT) with the efficient Fast Fourier Transform (FFT) algorithm (Cooley and Tukey, 1965). The absolute value of the complex frequency spectrum is the amplitude spectrum.

The amplitude spectrum plotted versus frequency for the synthetic example data is shown in Fig. 5.4 a). The main frequencies of the signal can be metered more precisely from this illustration than from the spectrogram shown above. The effect of added noise on the amplitude spectrum can be seen in Fig. 5.4 b). Since strictly random noise was added to the synthetic data set no peaks arising from the noise component can be found in the amplitude spectrum.
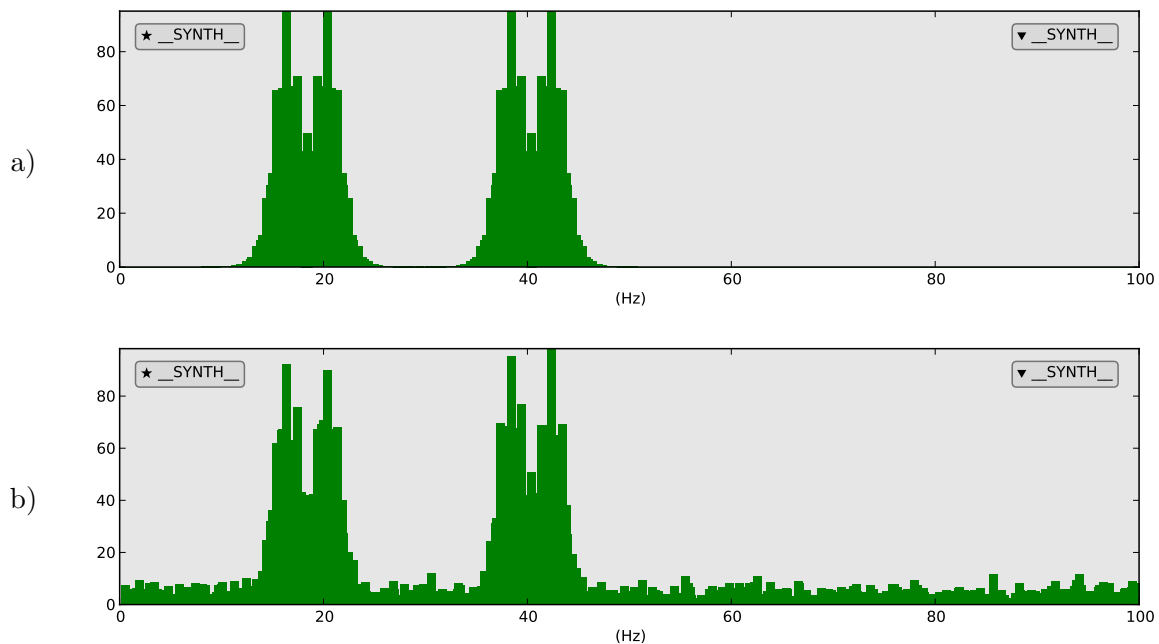
Figure 5.4.: *Amplitude spectra of the pure and the noisy synthetic signals:*
a) signal without noise
b) noisy data set

This frequency-domain representation of the data unveils the spectral composition of the data and is the base for appropriate filtering in later processing steps.

---

[4]Jean-Baptiste Joseph Fourier (1768–1830) French mathematician and physicist

5.4. Array processing

Data recorded with a sensor array comprise information on velocity and direction of a wave travelling across this array. Before the module used for processing the array data recorded as part of this thesis is discussed in detail, the principles and advantages of beamforming techniques are emphasised.

5.4.1. Beamforming

Beamforming techniques enhance the signal-to-noise ratio (SNR) by suppressing the noise in the data and preserving the signal. Hence these techniques are fundamental for the superior signal detection capability of arrays (Schweitzer et al., 2002).

A plane wave front approaches an array with specific slowness and backazimuth values to the single array stations causing differential travel times. These travel times are used by beamforming techniques to shift the single station-recordings in time for a certain slowness-backazimuth combination. If the shifting is done appropriately all signals with the the corresponding backazimuth and slowness will sum constructively (Rost and Thomas, 2002).

If all array sites are considered to be in the same horizontal plane travel time differences due to elevation differences (cf. Fig. 2.10) can be neglected. Therefore, the vertical apparent velocity cannot be measured and the corresponding slowness component becomes $q = 0$. Note that the influence of elevation differences is small for surface waves but could be severe for body waves. Hence, the assumption of equal station altitudes should only be made if the elevation differences are negligible with respect to the observed waves. From Fig. 5.5 the travel time delay τ_4 (measured in seconds) between the center site 0 and array site 4 is found to be

$$\tau_4 = \frac{t_4}{v_{app}} = \frac{r_4 \cdot \cos \beta}{v_{app}}, \; with \; r_4 = |\mathbf{r}_4|$$

Further evaluation with the subscript 4 omitted gives

$$\alpha + \beta + \theta = 90°, \; r \cdot \cos \beta = d, \; r \cdot \cos \alpha = x, \; d = \frac{x \cdot \cos \beta}{\cos \alpha} \qquad d = y \cdot \cos \theta + x \cdot \sin \theta$$

Substituting for the direction of propagation $\theta = \phi \pm 180°$ the horizontal distance travelled by the seismic plane wave is $d = x \cdot \sin \phi - y \cdot \cos \phi$. Without an elevation difference relative to the reference array site the travel time delay τ_j at any array site j with the horizontal coordinates (x, y) is

$$\tau_j = \frac{d_j}{v_{app}} = \frac{-x_j \cdot \sin \phi - y_j \cdot \cos \phi}{v_{app}} \tag{5.4}$$
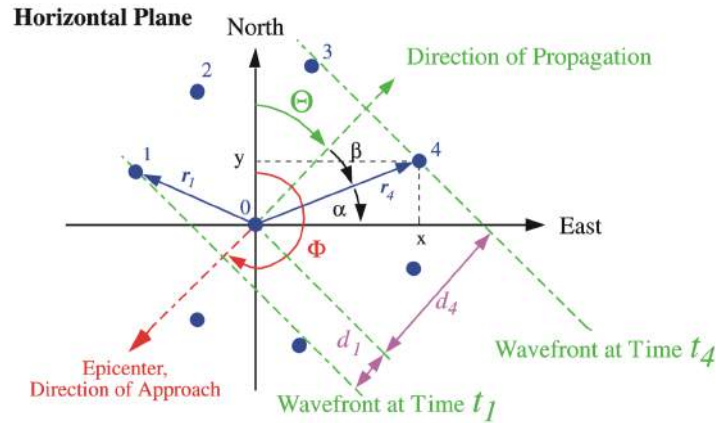
Figure 5.5.: *Sketch of a plane wave projected onto the horizontal plane, coming from south-west (backazimuth φ), running across an array and propagating in a north-easterly direction θ (Schweitzer et al., 2002)*

For the subsequent considerations the formal vector syntax of the delay times τ_j is more useful. With the parameters position vector $\mathbf{r}_j$ and slowness vector $\mathbf{s}$ the delay times are

$$\tau_j = \mathbf{r}_j \cdot \mathbf{s} \tag{5.5}$$

Geometrically, the delay times are defined as the projection of the position vector onto the slowness vector. By solving Eq. 5.5 (or Eq. 5.4) for a specific slowness-backazimuth combination, delay times τ_j for each array station can be estimated. Depending on the position of the single array sites in relation to the reference site and on the backazimuth, the calculated τ_j can be positive (advance of the signal) or negative (delay of the signal). Based on these delay times a 'delay and sum' process can be defined in order to compute an array beam. The digital sample of the seismogram recorded at array site j at time t is $w_j(\mathbf{r}_j, t)$. Hence the array beam is defined as

$$b(t) = \frac{1}{M} \sum_{j=1}^{M} w_j(t + \mathbf{r}_j \cdot \mathbf{s}) = \frac{1}{M} \sum_{j=1}^{M} w_j(t + \tau_j) \tag{5.6}$$

Applying the τ_j and summing the time shifted recordings of the M instruments is called beamforming (Schweitzer et al., 2002).

Subsequently the beamforming process and its advantages over a plain sum of seismograms are demonstrated with real array data. The traces recorded at the Gräfenberg array (GRF) of an event in the Lake Tanganyika region (Tanzania/Burundi) are depicted in Fig. 5.6. The event occurred on 2nd October 2000 at 02:25 UT with $M_b = 6.1$ in a depth of $34\,\mathrm{km}$ at $\delta = 59.9°$ and $\theta = 157.35°$.
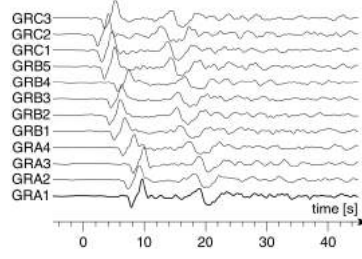
Figure 5.6.: *Example of data recorded at the Gräfenberg array (GRF) for an event in the Lake Tanganyika region, Tanzania/Burundi (Rost and Thomas, 2002)*

If the traces are just summed the resultant is a low-amplitude trace with distorted waveforms as can be seen from Fig. 5.7 a). Shifting the single traces for slowness and backazimuth before the summation aligns the wavelet and produces a so-called array beam (cf. Fig. 5.7 b)). The array beam is the resultant of the delay and sum method characterised by a clear waveform with a high amplitude (Rost and Thomas, 2002).
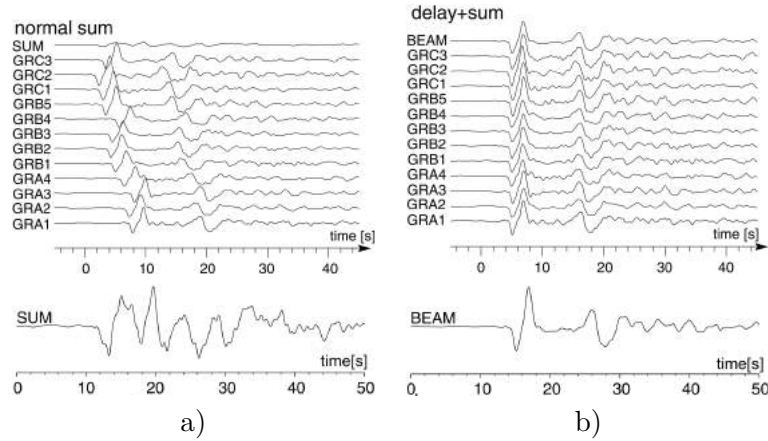
Figure 5.7.: *Seismograms recorded at the Gräfenberg array (GRF) (Rost and Thomas, 2002):*
a) Plain sum method applied leading to distorted waveforms
b) Delay and sum method applied giving the array beam

This example outlines the noise as the limiting factor. Consider the seismic waves as harmonic waves $S(t)$ without noise, no attenuation and an identical response at the array sites. Then the beamforming process would reproduce the signal $S(t)$ accurately. However, the observations are noisy signals $w(t) = S(t) + n(t)$ and the noise conditions affect the quality of the array beam (Schweitzer et al., 2002). Assume perfectly coherent signals $f(t)$ at every array station and thoroughly uncorrelated noise $n(t)$. Then the improvement of the SNR of the whole array (S) compared to the SNR of a single array station (s) is $S \approx \sqrt{M} \cdot s$ for an M-component array (Harjes and Henger, 1973).

5.4.2. fk analysis

As demonstrated in the section above, based on the slowness vector **s** beamforming enhances the amplitude of a given signal. This method requires all components of the slowness vector for the wave phase of interest to be known (Rost and Thomas, 2002). The fk analysis (frequency-wavenumber analysis) is one possibility to simultaneously determine the complete slowness vector (slowness and backazimuth) of an arriving wave. A basic description of the fk analysis is given in (Capon, 1969). According to (Rost and Thomas, 2002) the fk analysis "calculates the power distributed among different slownesses and directions of approach (Capon, 1973; Harjes and Henger, 1973; Aki and Richards, 2002)". A derivation of the fk analysis based on (Kelly, 1967) and (Harjes and Henger, 1973) can be found in (Rost and Thomas, 2002), whose key points are outlined subsequently.

Based on the principles of array seismology (Sec. 2.2.3) the formula for computing the array beam (Eq. 5.6) was found. By calculating the total energy recorded at an array by integration of the squared summed amplitudes over time (Parseval's[5] theorem) the array response function[6] (ARF)

$$|A\left(\mathbf{k}-\mathbf{k}_0\right)|^2 = \left|\frac{1}{N}\sum_{n=1}^{N}e^{2\pi i(\mathbf{k}-\mathbf{k}_0)\cdot\mathbf{r}_n}\right|^2 \tag{5.7}$$

is obtained, where

$$\mathbf{k} = (k_x, k_y) = \omega\cdot\mathbf{s} = \frac{\omega}{v_0}\left(\cos\theta, \sin\theta\right) \tag{5.8}$$

is the wave number vector. Hence, the total energy recorded at an array can be written in terms of the power spectral density $|S\left(\omega\right)|^2$ and the ARF as

$$E\left(\mathbf{k}-\mathbf{k}_0\right) = \frac{1}{2\pi}\int_{-\infty}^{+\infty}|S\left(\omega\right)|^2|A\left(\mathbf{k}-\mathbf{k}_0\right)|^2 d\omega \tag{5.9}$$

The power spectral density as a function of slowness and backazimuth is the result of the fk analysis. From the wavenumber vector $\mathbf{k} = (k_x, k_y)$ the slowness is calculated as

$$|\mathbf{k}| = \left(k_x^2 + k_y^2\right)^{1/2} = \frac{2\pi}{p} = \frac{\omega}{v_{app}} \tag{5.10}$$

where p is the apparent horizontal slowness. The backazimuth is computed as

$$\phi = \arctan\frac{k_x}{k_y} \tag{5.11}$$

---

[5]Marc-Antoine Parseval des Chênes (1755–1836) French mathematician
[6]influenced by aperture, configuration and interstation spacing of the array

The resultant baz-s plot[7] is a polar plot with the backazimuth plotted on the azimuth axis and the slowness plotted on the radial axis. The baz-s plot can be explained with the sketch depicted in Fig. 5.8. Assume an incident wave travelling through an imaginary halfsphere beneath an array. In an baz-s plot this halfsphere is projected onto the surface. The slowness is given by the distance of the maximum energy from the origin. The angle from North gives the backazimuth.
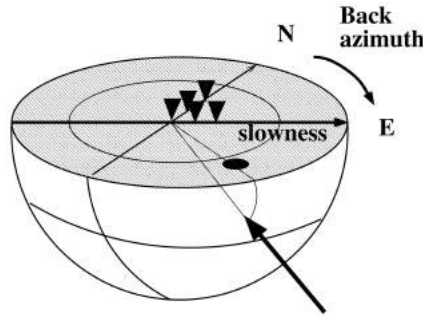
Figure 5.8.: *Explanatory sketch of the resultant baz-s plots (Rost and Thomas, 2002)*

5.4.3. Array analysis

This module was largely adopted from the ObsPy tutorial *Beamforming - FK Analysis*[8] provided by The ObsPy Development Team (Beyreuther et al., 2010). Based on the geometry information and the array data the fk analysis is carried out. The positions of the array stations may either be given as longitude/latitude or cartesian coordinates. Furthermore, it is possible to use a local coordinate system instead of a superordinate one.

The array analysis results are the backazimuth and the slowness illustrated in form of polar plots (hereinafter referred to as baz-s plots). The resultant baz-s plots for the pure and the noisy synthetic data set are shown in Fig. 5.9 a) and Fig. 5.9 b), respectively. A comparison of the baz-s plots points out the effect of noise on the array analysis results. The backazimuth (measured in °) is counted clockwise between the North and the direction towards the source, the slowness (measured in $s\,m^{-1}$) is metered along the radial axis. The colour-coded relative power indicates correct values of these parameters for the given data. If the location of the source is known the corresponding backazimuth is indicated by a blue dot.

---

[7]The power spectral density displayed in a polar coordinate system
[8]`http://docs.obspy.org/tutorial/code_snippets/beamforming_fk_analysis.html`
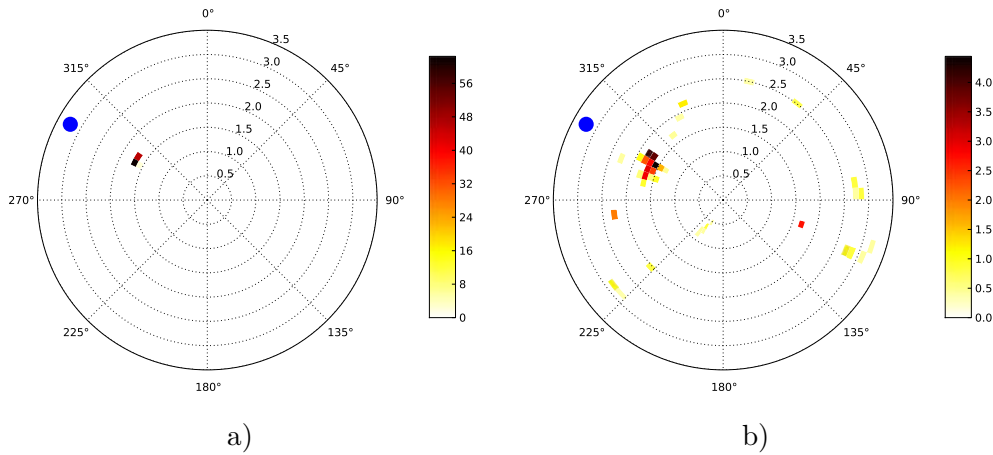
Figure 5.9.: *Resultant baz-s plots of the synthetic example data set with the known back-azimuth indicated by a blue dot:*
a) signal without noise
b) noisy data set
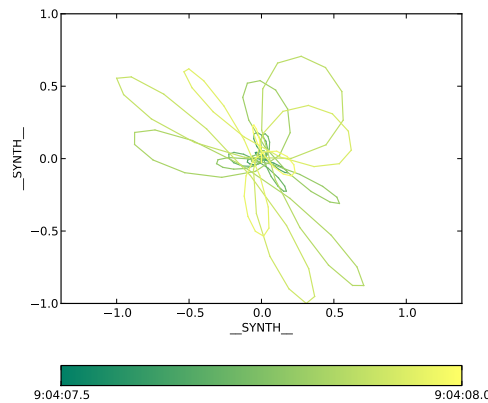
Figure 5.10.: *Particle motion exemplarily vizualised for the first* 0.5 s *of the synthetic data*

5.5. Particle motion

Particle motion plots are created by plotting the seismograms for two components of motion in one diagram. One component is plotted on the horizontal axis the other one on the vertical axis. These diagrams are used to determine seismic phases (Braile, 2010). In this thesis diagrams like the one shown in Fig. 5.10 are used. These diagrams illustrate the particle motions as a colour-coded line. As can be seen from the example plot the color code illustrates the first particle motions by using greenish colors and the last ones by using yellowish colors. Particle motion plots can be used to determine the seismic wave type associated with a certain part of the seismic data. In practice, mostly the particle motions in the E–N plane and in the E–Z plane[9] are investigated.

---

[9]In the R–Z plane if the seismograms are rotated

In-situ experiments

The subsequent sections give information on the experiment sites and the experiment set-up. The main topics are the presentation and discussion of the data analysis results.

6.1. Altlengbach

Due to its spatial proximity to a main motorway (A1) the ALPAACT station ALBA (blue dot in Fig. 6.1) is predestined to verify the capabilities of the seismological equipment and the data analysis techniques with regard to seismic noise sources. The small display detail shows the motorway running from West to South-East with respect to the station ALBA.
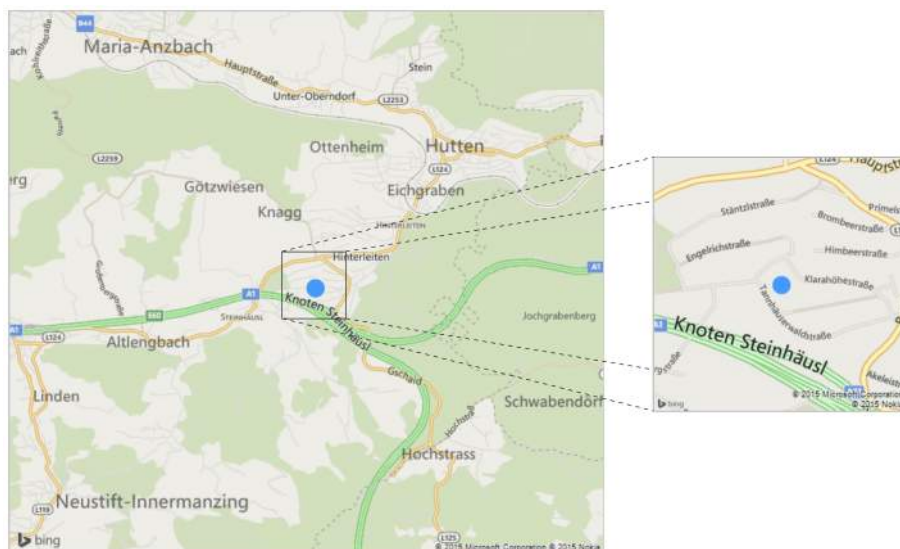
Figure 6.1.: *Area map of of ALPAACT station ALBA (Altlengbach, Lower Austria)*

According to the description of the geological vicinity in (Brückl et al., 2014) the ALPAACT station ALBA "is located in the Lower Austrian Rhenodanubischen flysch zone of the Wienerwald. The Greifenstein nappe is the dominant tectonic unit. It is composed of the Greifenstein

Formation (404), a succession of thick bedded turbidites, and calcareous turbidites of the Zementmergelserie (407). The Altlengbach Formation (406) consists of a heterogeneous succession of calcareous siliciclastic sandstones, claystone and marlstone with a thickness up to 1500m. Towards south, the Greifenstein nappe is seperated from the Laab nappe (413) by the Gresten Klippenzone (300)" (cf. Fig. 6.2).
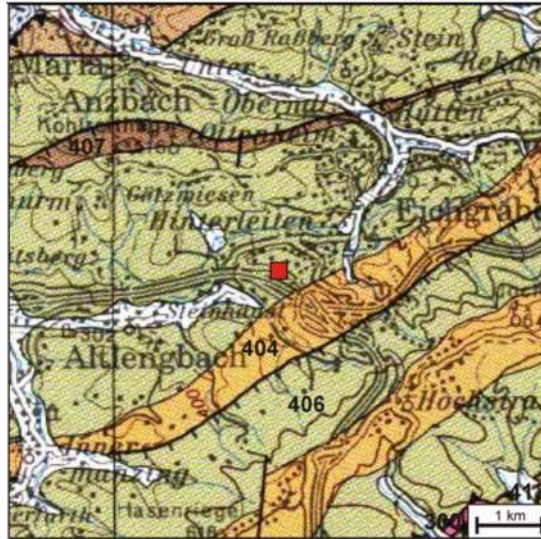
Figure 6.2.: *Geological map of the vicinity of ALPAACT station ALBA, taken from (Schnabel, 2002)*

A seismic and geological profile of the station site is depicted in Fig. 6.3. From this diagram the increase of v_p (P wave velocity) and v_s (S wave velocity) with depth can be seen (note the double scale of v_s).

6.1.1. Experimental setup

On 8th July, 2014 a minimal seismic array consisting of three 3C-geophones arranged in form of an equilateral triangle with about 10 m lateral length was installed at the ALBA station site (subsequently denoted as ALBA array). The seismic data were recorded with two REF TEK 130S DAS units at a sampling rate of 200 sps. The positions of the ALBA array stations were determined with geodetic GNSS measurements.

6.1.2. Data analysis

Since the motorway is a seismic source that continuously generates seismic noise only a small representative part of the recorded data was used for the detailed analysis. Based on two main criteria, namely to gain a high degree of visual interpretability and to obtain array analysis results within a reasonable amount of time, a data subset of 120 s was chosen.
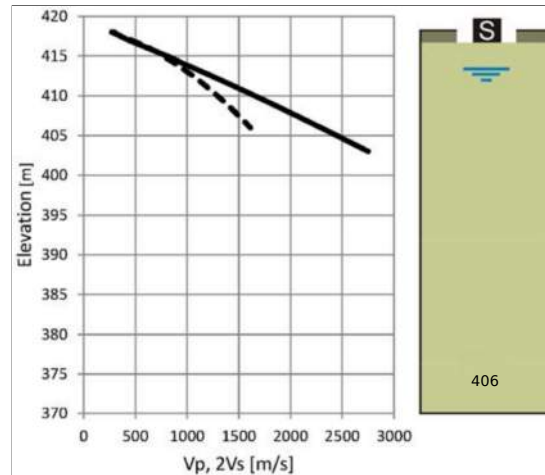
Figure 6.3.: *Seismic and geologic profile of ALPAACT station ALBA (Altlengbach, Lower Austria), taken from (Brückl et al., 2014):*
v_p... solid line
$2v_s$... dashed line

The data recorded in the period from 09:50 UTC to 09:52 UTC and the corresponding spectrogram are shown in Fig. 6.4. This data subset detected with the geophone's vertical component is thought to contain the seismic noise generated by the near-by motorway. Especially the second half of the data subset shows a clearly visible waveform. The appearance of this waveform is accompanied by an increase of low frequencies in the spectrogram (approximately 10 Hz). The spectrogram shows the same characteristics for the first 30 s of the data subset corresponding to a waveform with lower amplitude. A motorway also produces acoustic noise that may be strong enough to be visible in the seismic data. The vehicles on the motorway passing the ALBA array behave like a moving source to an observer at rest. If the low-frequency waveform is caused by the traffic on the motorway the arising Doppler effect should be perceptible in the spectrogram. Indeed the spectrogram shows weak high-frequency (approximately 70 Hz to 90 Hz) Doppler effect characteristics corresponding to the waveforms. Thus, a first evidence for the motorway being the source of the seismic noise may has been found.

The amplitude spectrum of the 120 s noise data set is depicted in Fig. 6.5. The recorded seismic data consist mainly of frequencies below 20 Hz. The Doppler effect is to weak to be visible in the amplitude spectrum. From this diagram the frequency range associated with the motorway is found to be 8 Hz to 12 Hz.

The effect of applying a corresponding bandpass filter to the data subset is shown in Fig. 6.6. By omitting the high-frequency part of the noise the previously identified waveforms become distinctly visible.
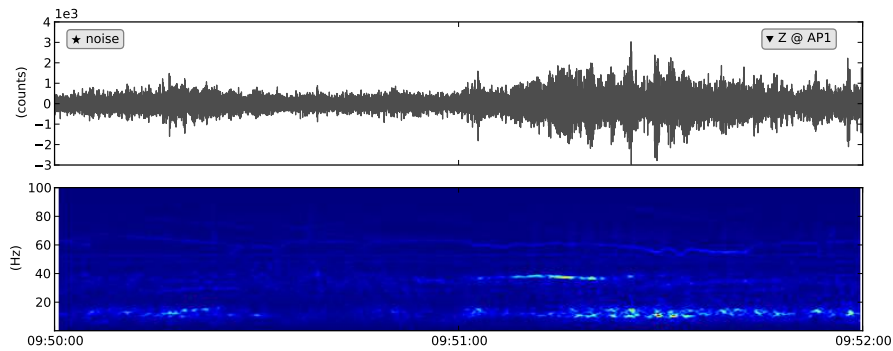
Figure 6.4.: *Time-domain representation and spectrogram of the noise recorded at array point AP1 with the geophone's vertical component*
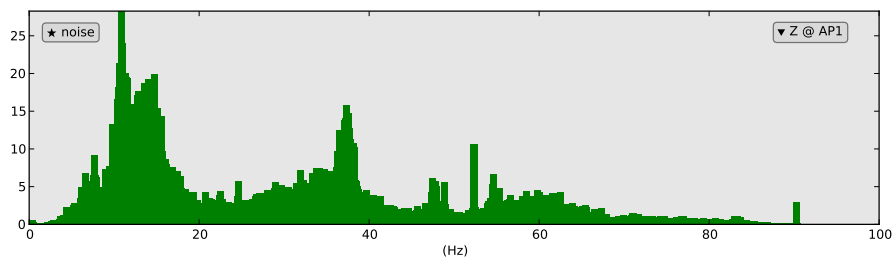
Figure 6.5.: *Amplitude spectrum of noise recorded at array point AP1 with the geophone's vertical component*
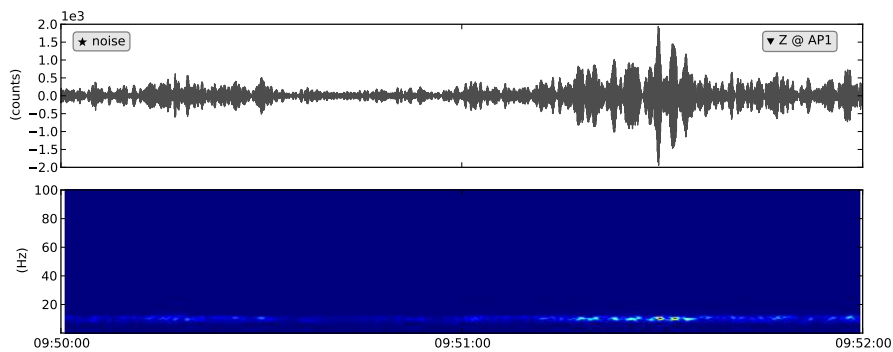
Figure 6.6.: *Time-domain representation and spectrogram of the 8 Hz to 12 Hz bandpass filtered noise recorded at array point AP1 with the geophone's vertical component*

Using the unfiltered noise for array analysis yields the baz-s (backazimuth-slowness) plot depicted in Fig. 6.7 a). The slowness of the recorded seismic waves ranges approximately from $0.5\,\mathrm{s\,km^{-1}}$ to $1.75\,\mathrm{s\,km^{-1}}$ which correspond to velocities of about $600\,\mathrm{m\,s^{-1}}$ to $2000\,\mathrm{m\,s^{-1}}$. According to the diagram the backazimuth from the ALBA array to the noise generating source is approximately 225°. The baz-s plot shown in Fig. 6.7 b) is the result of the array analysis using the bandpass filtered seismic data. The applied bandpass filter significantly influences the array analysis. The recovered seismic velocities span a smaller range with a center velocity of approximately $1300\,\mathrm{m\,s^{-1}}$. This value can be confirmed by the velocity model shown in Fig. 6.3. For the filtered noise the backazimuth to the source is no distinct value since a broad range of backazimuth values was computed. The backazimuth values range from approximately 160° to 260°. Comparing the resultant baz-s plot with the small display detail in Fig. 6.1 shows the high coincidence between the locations of the source resulting from the array analysis and the actual location of the motorway.

a)   b)
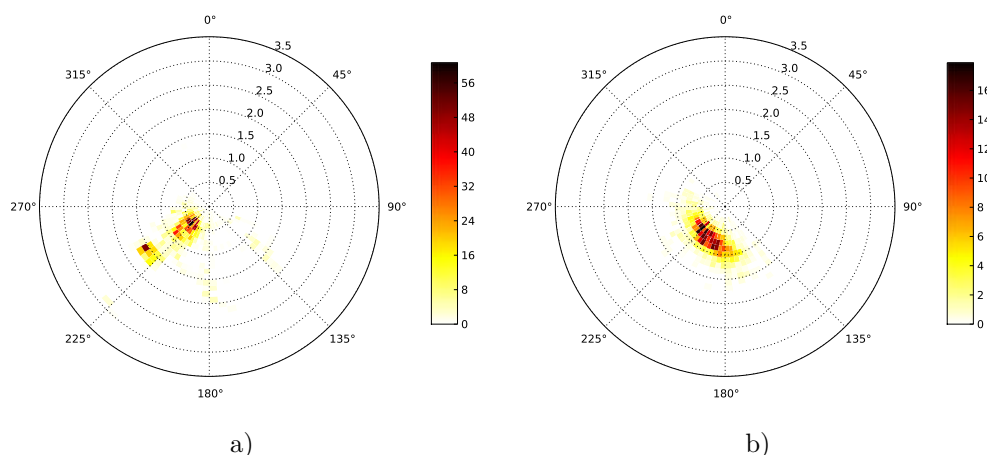
Figure 6.7.: *baz-s plot of the signals produced by a nearby motorway observed with the ALBA geophone array:*
a) unfiltered
b) 8 Hz *to* 12 Hz *bandpass-filtered*

Road and rail traffic are assumed to produce ground motion that primarily consists of Rayleigh waves. Thus, by investigating the particle motions associated with the noise produced by the motorway it may be possible to verify the existence of this surface wave type. The particle motion in the East-West–North-South plane for the unfiltered 120 s noise data subset is illustrated in Fig. 6.8 a). The particles are not following a clear pattern and the motion appears to be rather random in the time-domain. Applying the 8 Hz to 12 Hz bandpass filter on the data yields the particle motion plot shown in Fig. 6.8 b). In this illustration the main particle motions occur in the North-East–South-Western direction. By comparing this direction to the location of the motorway and the computed backazimuth values, respectively, the direction of the particle motion can be assumed to point toward the noise source.

a)   b)
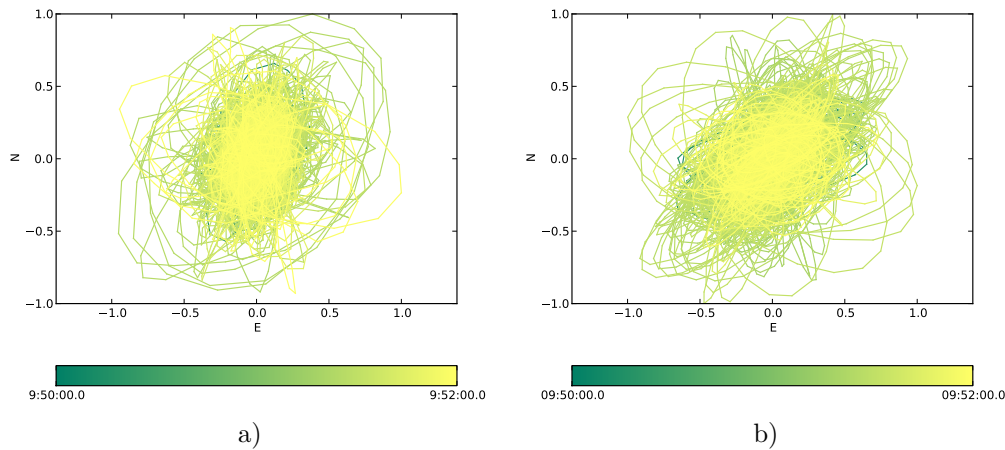
Figure 6.8.: *Particle motion in the EW-NS plane:*
a) unfiltered
b) 8 Hz *to* 12 Hz *bandpass-filtered*
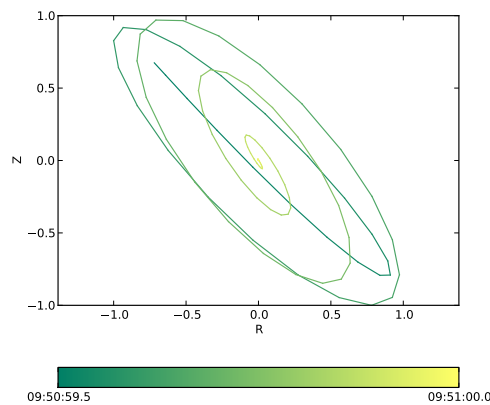
Figure 6.9.: *Particle motion in the R–Z plane of the* 8 Hz *to* 12 Hz *bandpass-filtered seismic data (seismograms rotated by* 200°)

In order to verify the type of seismic wave crossing the ALBA array the NS and EW geophone component seismograms have to be transformed to radial (R) and transversal (T) seismograms by a rotation toward the source. The seismograms are rotated on the basis of the backazimuth range recovered from the bandpass filtered data via array analysis.

The particle motion associated with the motorway was determined by using a 0.5 s (100 samples) section of the 8 Hz to 12 Hz bandpass filtered noise data. The seismograms are rotated by 200° and the resultant particle motion in the R–Z plane is depicted in Fig. 6.9. The color coded time information can be used to identify the direction of the particle motion by following the line from the greenish to the yellowish colors. By this means the particle motion associated with the traffic on the motorway passing the ALBA array is retrograde. Due to the inclination of the ellipse the wave cannot distinctly be referred to as a Rayleigh wave. Most probably, the particle motion indicates a superposition of Rayleigh and SV waves.

6.2. Knödelhütte

Knödelhütte is the name of a forestal test facility that belongs to the University of Natural Resources and Life Sciences (BOKU[1]). The areal is located in the 14th district at the western edge of urban Vienna (see Fig. 6.10). A small part of this property was generously dedicated for the implemenation of experiments.
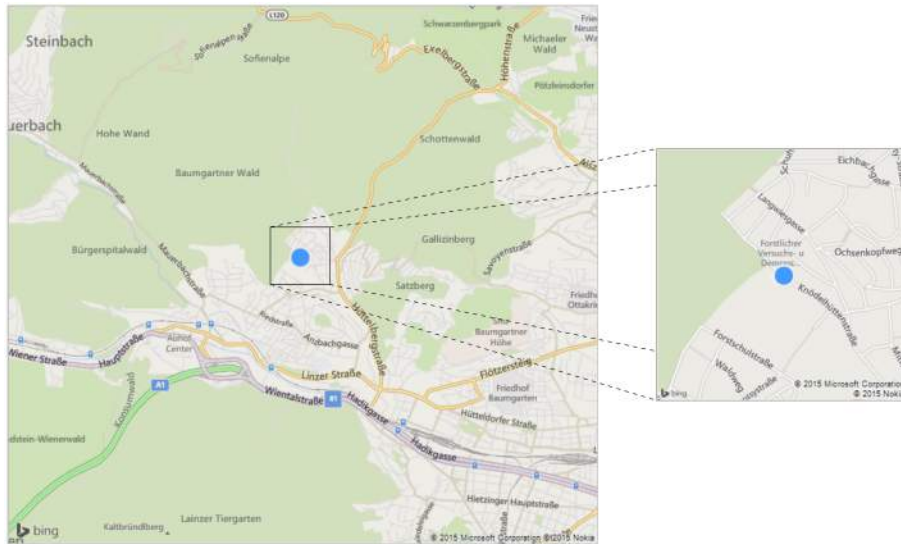
Figure 6.10.: *Area map of station KNH at the test site Knödelhütte (Vienna)*

The Knödelhütte is situated in the Rhenodanubischen flysch zone of the Wienerwald (cf. Fig. 6.11). A detailed description of the geological settings in the vicinity of the Knödelhütte can be found in (Wagreich, 2008). The Knödelhütte array (indicated by a blue dot and hereinafter denoted as KNH array) itself is located in the area of the Agsbach Formation (yellow) that consists of marl and sandstone (Late-Middle Eocene).

6.2.1. Experimental setup

On 25th September, 2014 a minimal seismic array consisting of three 3C-geophones arranged in form of an equilateral triangle with about 10 m lateral length was installed on the premises of the experimental garden Knödelhütte. Additionally, a microphone was installed at each station of the array. The seismic and acoustic data were recorded with two REF TEK 130S DAS units at a sampling rate of 500 sps. Artificial signals were produced by using the sources described in Sec. 4.3.1 at five different sites around the KNH array.

The positions of the KNH array stations as well as the positions of the shot points were determined relative to each other and were converted into a local coordinate system afterwards. The overall layout of array points (AP) and shot points (SP) is depicted in Fig. 6.12.

---

[1]abbreviation from the german name of the university
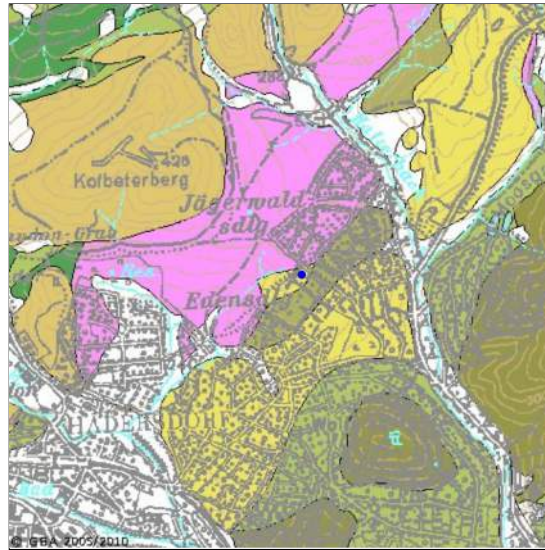
Figure 6.11.: *Geological map of the vicinity of test area at the Knödelhütte (blue dot), taken from (Schnabel, 1997)*
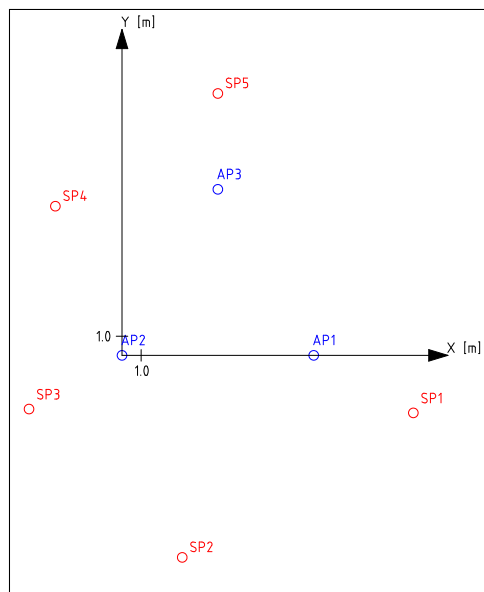
Figure 6.12.: *Array point (AP) and shot point (SP) layout of the Knödelhütte experiment*

The microphones installed at the three array points were connected to one data logger to guarantee uniformly timestamped acoustic data. In order to be able to record high frequencies while the amount of data produced being moderate $500\,\text{sps}$[2] were taken during the Knödelhütte experiment.

6.2.2. Data analysis

For the Knödelhütte experiment three different controlled sources (cf. Tab. 4.1) were applied at five shot points (SP) distributed around the KNH array. In the subsequent sections signals produced by hammer + plate (HP, seismic-acoustic surface source), hammer (H, seismic surface source) and drum (D, low altitude acoustic source) are investigated by using the data analysis techniques discussed in Sec. 5. Additionally, cultural seismic noise was recorded during the experiment. The bus stop in front of the Knödelhütte areal is periodically served by a bus providing a (moving) seismic-acoustic surface source. A helicopter overflight representing a (moving) high altitude acoustic source produced an additional data set, too.

6.2.2.1. Analysis of signals produced by the seismic surface sources HP and H

Since the source HP is the standard source type in small scale seismic surveys it is the first one to be investigated within this study. Simultaneously, source H is investigated in order to show similarities and differences of these seismic surface sources.

The signals produced by sources HP and H recorded with the geophone at array point AP2 and the corresponding spectrograms are presented in Fig. 6.13 a) and Fig. 6.13 b), respectively. The hammer strokes produce signals with similar waveform regardless of the plate being used or not. The signal amplitudes in the seismic data are in the same range for both seismic surface sources (10^5 counts). In both cases the pulses produced by the hammer strokes clearly exceed the environmental noise level present on the seismic sensor. Although the signals reproduce as distinct pulses the resultant waveform appears to comprise low amplitude first arrivals (body waves), a high amplitude portion (surface waves) and coda. Particularly the first arrivals and the high amplitude portion are subject of further investigation in this section later on. The spectrograms of the recorded hammer strokes confirm the similarity of the produced signals also in the frequency domain. According to this diagrams the frequencies primarily forming the signals in the seismic data are below $100\,\text{Hz}$. Hence, neither the signals nor the spectrograms provide a criterion that allows for a discrimination of the seismic surface sources.

A more detailed view of the frequency content of the signals is provided by the amplitude spectra presented in Fig. 6.14. The amplitude spectra verify the frequency characteristics deduced from spectrograms. From Fig. 6.14 a) it can be seen that there is no significant contribution to the signal of frequencies above $120\,\text{Hz}$.

---

[2]samples per second
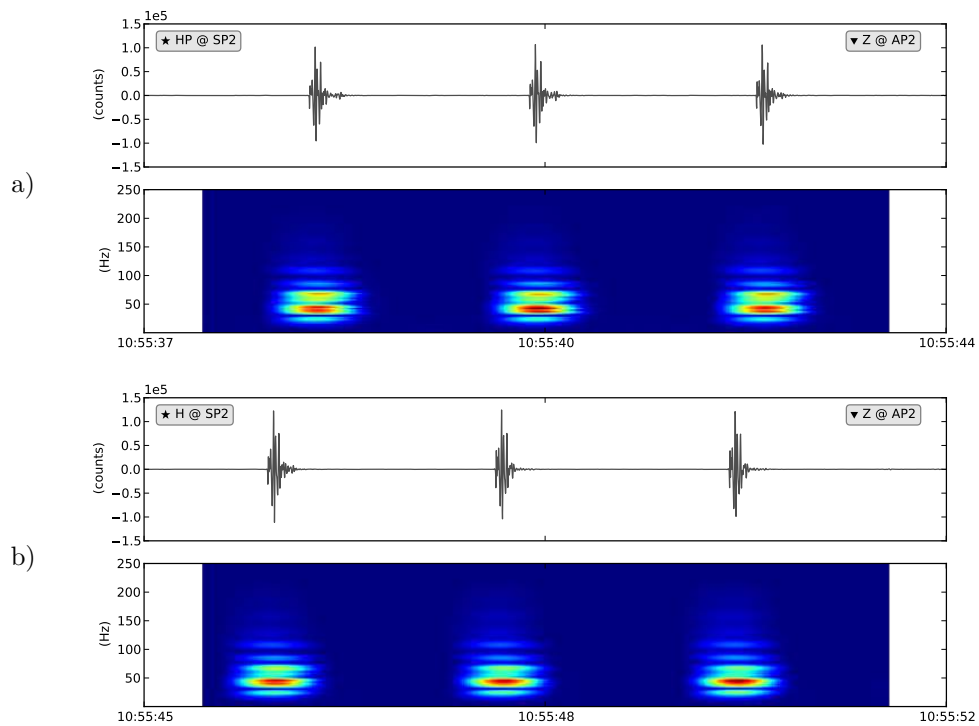
Figure 6.13.: *Signals and spectrograms produced by sources HP and H at shot point SP2:*
a) source HP
b) source H
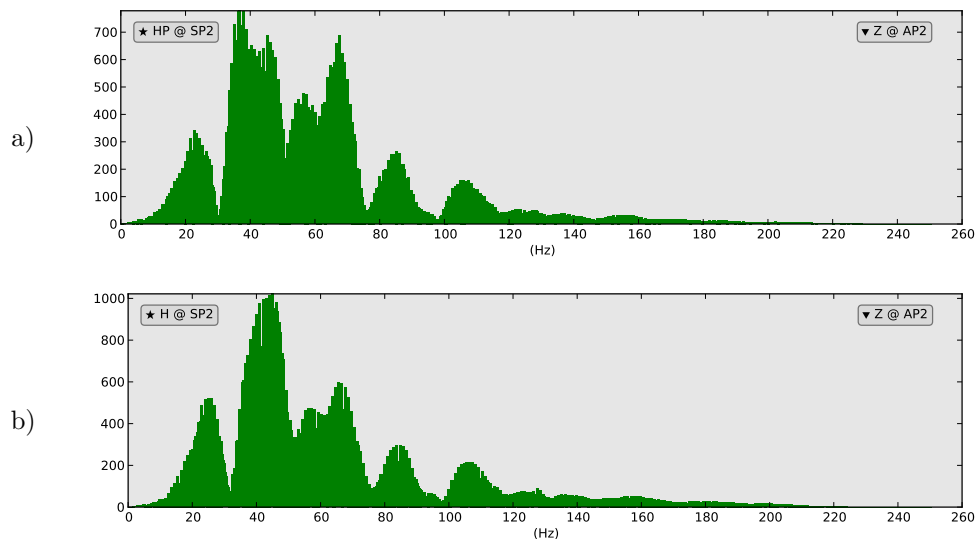
Figure 6.14.: *Amplitude spectrum of the signal produced by sources HP and H at shot point SP2 recorded with the vertical geophone component:*
a) source HP
b) source H

The main frequencies occur in the range from 40 Hz and 60 Hz. The frequency peaks at 20 Hz and 60 Hz are similar for both sources whereas the remaining part of the amplitude spectra seems to be slightly shifted with respect to each other.

In order to investigate the first arrivals a more detailed illustration of a single hammer stroke is required. The detailed view of a signal produced by source HP at shot point SP2 is shown in Fig. 6.15. The seismic data are shown as black lines whereas the acoustic data are illustrated as blue lines. From this diagram it can be easily seen that the first arrivals in the seismic data precede the first arrivals in the acoustic data. Nevertheless, the acoustic sensor detects the signals before the largest amplitudes occur in the seismic data. Initially, only the seismic data are considered. For a detailed discussion the signal recorded at AP1 is used. The AP1 seismogram is an excellent example to define the different phases of a seismic wave. The pulse produced by the hammer stroke at SP2 consists of a portion with low amplitude (body waves) and another one with more than twice the amplitude (surface waves).

The existence of different seismic wave phases can be verified by separately investigating these signal portions. In order to suppress non body wave portions in the data an appropriate window was defined in the time-domain. The window is illustrated as a red line in Fig. 6.15. Equally, a similar window was defined for the surface wave portion of the pulse (green line in Fig. 6.15). Applying these windows on the seismic data offers the possibility to verify the existence of body and surface waves via particle motion plots and array analysis. The signals produced by source H recorded at the three KNH array stations and an illustration of the corresponding windows can be found in the appendix (Sec. A.1).

If the body wave portion mainly consists of P waves, the ground movement associated with this wave type should occur in the direction of wave propagation. Perpendicular to this direction the particle motion should be small or even zero. The particle motions in the East-West–North-South plane associated with the body wave portion of the pulse are shown in Fig. 6.16 a). Since the signals are dominated by low frequencies the particle motion plot for the low-pass filtered data set is shown in Fig. 6.16 b). The ground movement illustrated in this diagram is similar to the one expected for P or SV waves. The main movement occurs in the North-South direction, while the movement in the East-West direction is zero. Hence, the P wave assumption can be confirmed. The body wave particle motion does not correctly indicate the location of the source. The discrepancy is approximately 20°.

Assuming Rayleigh waves as the dominating surface wave type in the signal retrograde particle motions should be visible in a plane perpendicular to the direction of wave propagation. The seismograms used for the surface wave particle motion plots are rotated towards the (known) location of the source (corresponds to a backazimuth of 200°). The particle motions in the R–Z plane associated with the surface wave portion of the pulse are shown in Fig. 6.17 a).
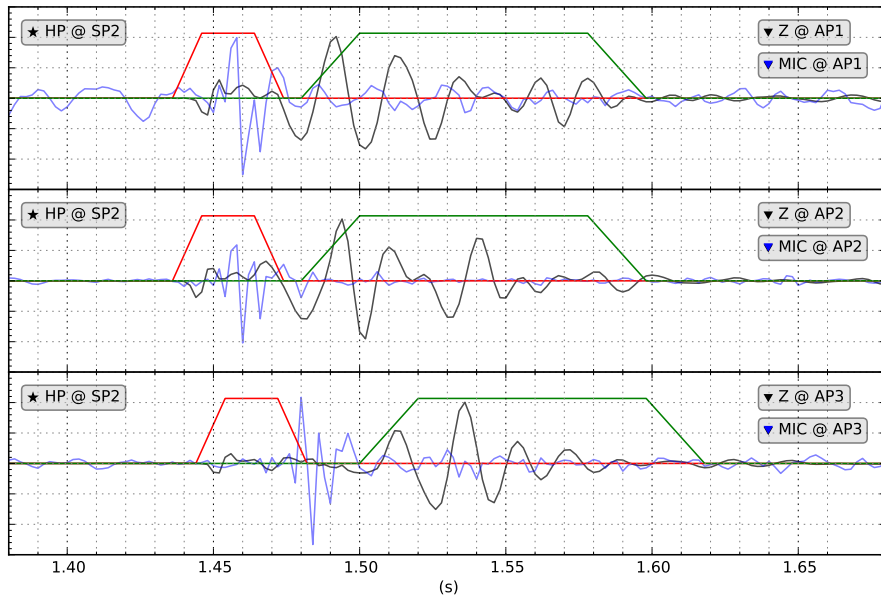
Figure 6.15.: *Signals produced by source HP (single hammer stroke) at shot point SP2 recorded with the KNH geophone and microphone array:*

black	*...*	*seismic data*
blue	*...*	*acoustic data*
red	*...*	*body wave filter*
green	*...*	*surface wave filter*
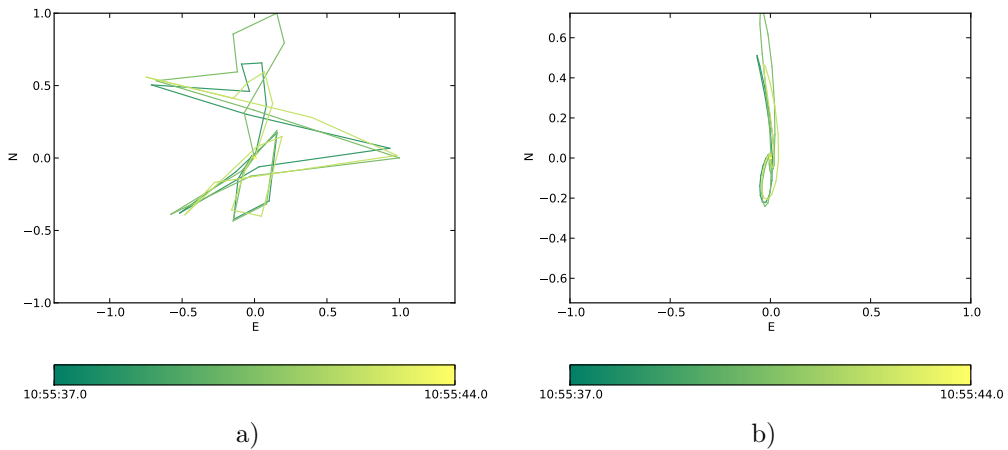
Figure 6.16.: *Particle motion associated with the body wave produced by source HP at shot point SP2:*
a) E–N plane
b) E–N plane (low-pass filtered)
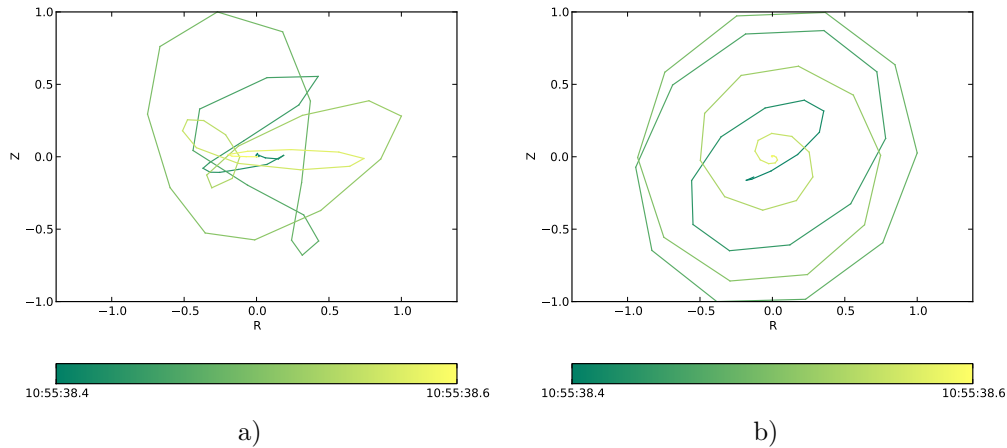
Figure 6.17.: *Particle motion associated with the surface wave produced by source HP at shot point SP2:*
a) R–Z plane (baz=200°)
b) R–Z plane (baz=200°, bandpass filtered)

The particle motion plot for the low-pass filtered data set is depicted in Fig. 6.17 b). From this illustration a retrograde particle motion is clearly visible. Hence, the highest amplitudes in the surface wave portion exhibit a particle motion similar to Rayleigh waves. The particle motions related to the data sets produced by source H yielded similar results. The resultant particle motion plots are provided in the appendix (Sec. A.2).

Based on the baz-s plots obtained via array analysis the existence of body and surface waves in the hammer stroke signals can be verified, too. For the body wave portion the baz-s plots should give a lower slowness than for the surface wave portion. Additionally, the direction to the source (backazimuth) is recovered from the given data set and illustrated in the the baz-s plot. Both, the data set produced by source HP and the one produced by source H are used for the array analysis. Due to the similarities of the data the results of the array analysis should yield similar results. For the body wave portion of the signals generated by source HP the resultant baz-s plot is shown in Fig. 6.18 a). The computed slowness is $0.7\,\mathrm{s\,km^{-1}}$ corresponding to a velocity of approximately $1300\,\mathrm{m\,s^{-1}}$ (P wave velocity). The baz-s plot resulting from the array analysis of the surface wave portion in the HP signals is presented in Fig. 6.18 b). Note that the radial axis spans a larger slowness range in this illustration. The slowness corresponding to the surface wave portion is approximately $4.3\,\mathrm{s\,km^{-1}}$ or in terms of velocity $240\,\mathrm{m\,s^{-1}}$. The low body wave slowness and the higher surface wave slowness confirm the existence of the postulated wave phases. The computed backazimuth corresponds to the actual location of shot point SP2. The resultant baz-s plots for the body wave and surface wave portion of the signals produced by source H are shown in Fig. 6.19 a) and Fig. 6.19 b), respectively. As can be seen, the computed slowness and backazimuth values are identical for sources HP and H.
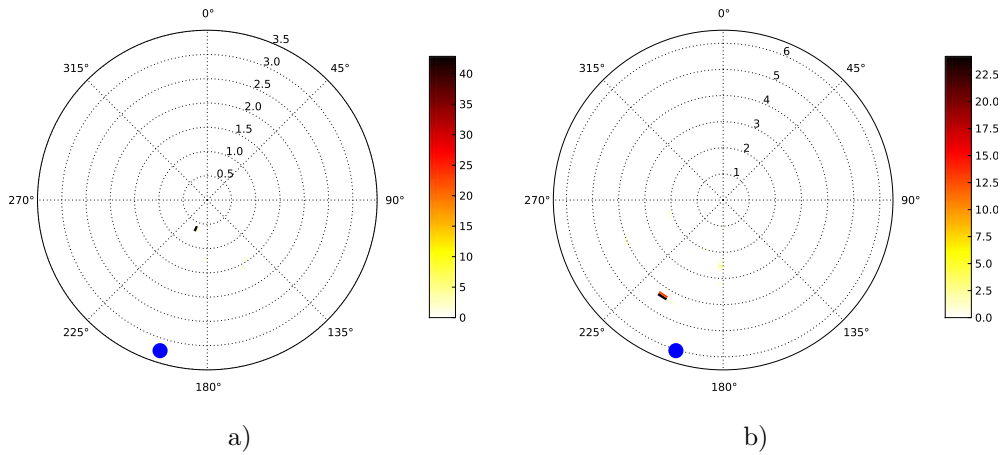
Figure 6.18.: *baz-s plots of the body wave and surface wave portions of the signal produced by source HP at shot point SP2 observed with the KNH geophone array (actual backazimuth indicated by a blue dot):*
a) body wave portion
b) surface wave portion
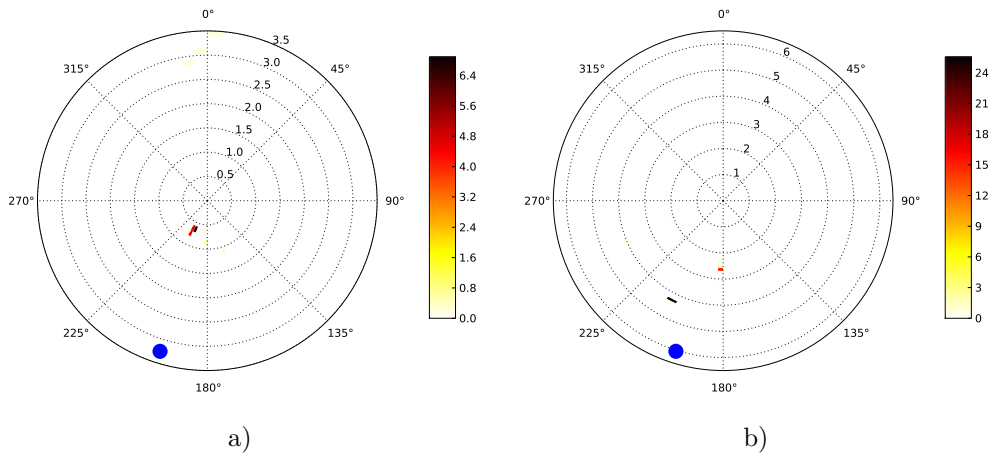
Figure 6.19.: *baz-s plots of the body wave and surface wave portions of the signal produced by source H at shot point SP2 observed with the KNH geophone array (actual backazimuth indicated by a blue dot):*
a) body wave portion
b) surface wave portion

A body wave window was not only defined for source HP at shot point SP2 but also for the signals produced by source HP at the other shot points arranged around the KNH array. Hence, it is possible to map all shot points side by side by using the resultant baz-s plots obtained via array analysis. The resultant baz-s plots for the body wave portion of the signals produced by source HP at shot points SP1 to SP5 are shown in Fig. 6.20 a) to e). Although some baz-s plots also depict wrong solutions for slowness and backazimuth the correct backazimuth values could be found for every shot point. Comparing the analytically found directions to the sources with the actual shot point positions in Fig. 6.12 confirms the usability of a minimal sensor array. The computed slowness values for the different source locations vary from $0.6\,\mathrm{s\,m^{-1}}$ to $1.2\,\mathrm{s\,m^{-1}}$ (P wave slowness values).

The signals recorded with the microphone at array point AP2 and the corresponding spectrogram are presented for sources H and HP in Fig. 6.21 a) and Fig. 6.21 b), respectively. A single hammer stroke recorded with a microphone reproduces as a sharp pulse without significant oscillations before or after the main pulse. The signals produced by sources H and HP depict with amplitudes in the same size range. Based on the impression of the sound emitted by these sources a significant difference in the signal amplitudes would be expected. The maximum amplitudes for each source exhibit the HP amplitudes being approximately larger by a third than the H amplitudes. Thus, a difference can be detected although it is a weaker discrepancy than assumed. This may be due to the anti-aliasing filter used by the recorder as pointed out subsequently.

The spectrograms show similar characteristics, namely a narrow low frequency band and a broader high frequency band. Taking into account the contribution of different frequency ranges to the signals the spectrograms provide an interesting criterion in order to characterise the investigated sources. The ratio of contribution of the low frequency band and the high frequency band to the signal is different for sources H and HP. While the ratio is nearly balanced for source H there is a larger contribution of the high frequency band to the signal in the case of source HP. Since the hammer stroke on a metal plate produces a high frequency sound this frequency-domain characteristics are comprehensible. For a more detailed investigation of the frequency content amplitude spectra can be used.

The amplitude spectra depicted in Fig. 6.22 are computed for a single hammer stroke for each source. From these diagrams it is obvious that in the case of source HP primarily higher frequencies contribute to the signal. In the case of source H low and high frequencies contribute to the signal in the same way. The reason for the higher frequency signals produced by source HP is the usage of the plate. Executing a hammer stroke on a plate produces a high frequency sound if compared to a hammer stroke on bare soil. Hence, frequency analysis of microphone measurements may provide basic information on environmental noise sources. The high frequency band of the H signal spans from approximately 120 Hz to 225 Hz whereas the one for the HP signal has the same maximum frequency but a different minimum frequency of about 90 Hz.
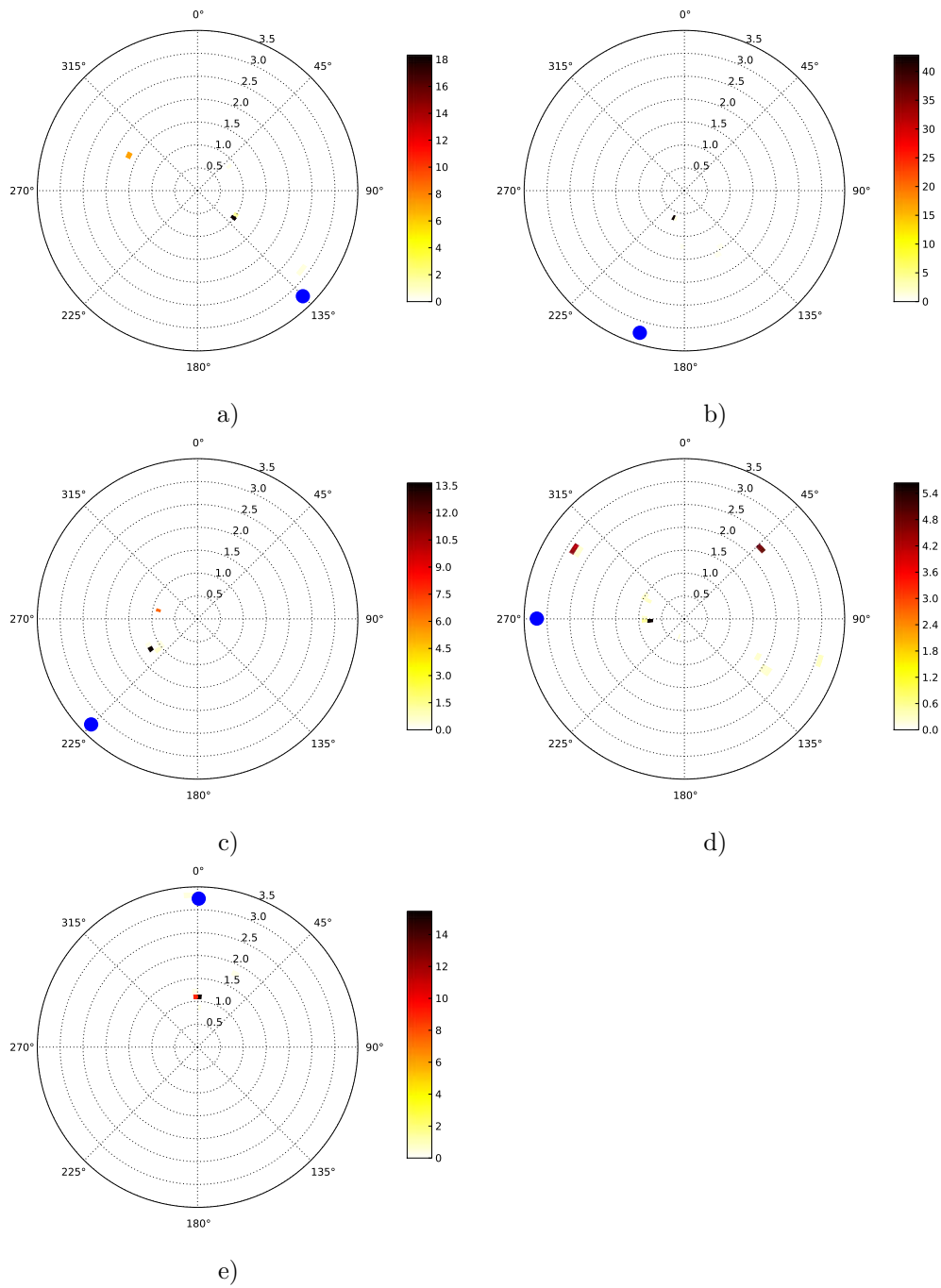
Figure 6.20.: *baz-s plots of the body wave and surface wave portions of the signal produced by source HP at different shot points observed with the KNH geophone array (actual backazimuth indicated by a blue dot):*
a) to e) depict the results for SP1 to SP5
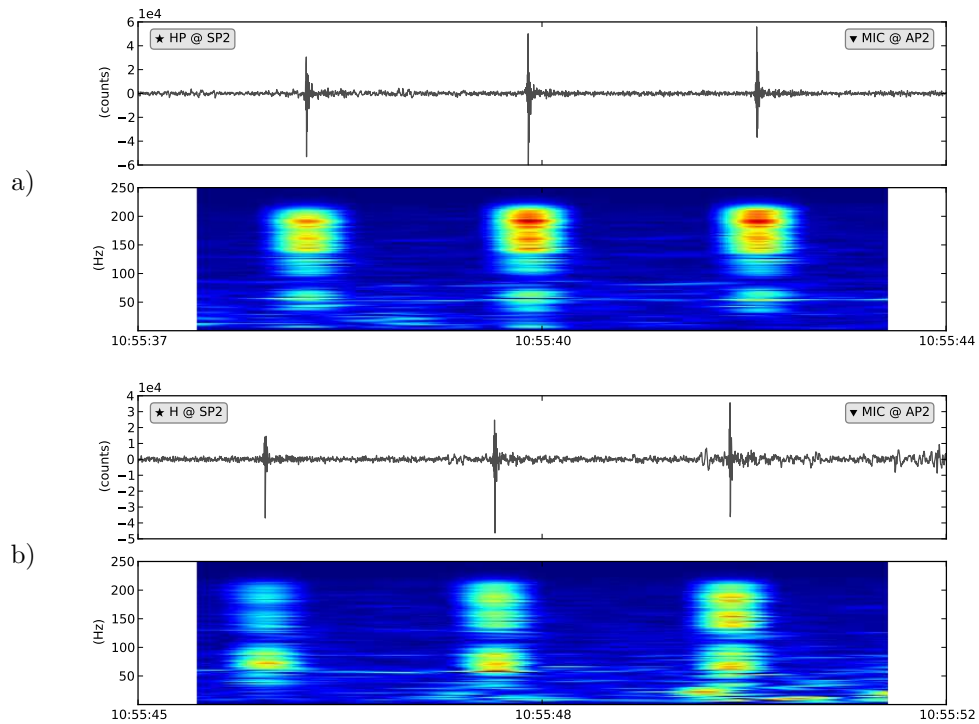
Figure 6.21.: *Signals and spectrograms produced at shot point SP2 recorded with an acoustic sensor:*
a) source HP
b) source H
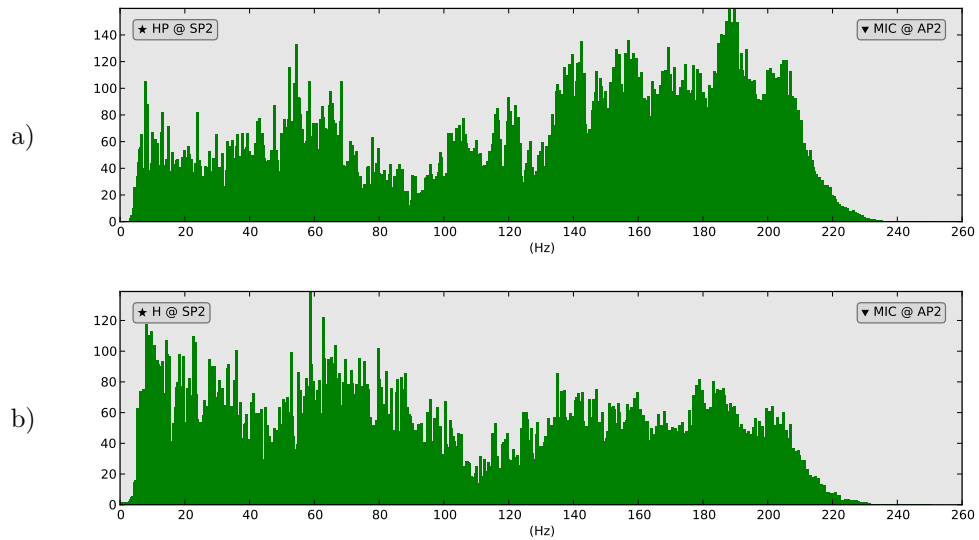
Figure 6.22.: *Amplitude spectrum of the signal produced by sources HP and H at shot point SP2 recorded with a microphone:*
a) source HP
b) source H

The data were recorded at a sampling rate of 500 sps giving a Nyquist[3] frequency of 250 Hz. However, the frequency spectra already decline before this frequency. Especially in the case of HP the spectrogram gives the impression that the signal consists of even higher frequencies that could not be recorded due to the sampling rate. The similar decline of both frequency spectra indicates that an anti-aliasing filter is used by the recording unit. As a consequence also the signal amplitudes may be influenced by the anit-aliasing filter. The most obvious difference between the acoustic amplitude spectra (Fig. 6.22) and seismic amplitude spectra (Fig. 6.14) is the smoother appearance in the case of the seismic data. This circumstance may be due to the lower noise level present in the seismic data indicating a better SNR than for the acoustic data. Judged by visual inspection the overall similarity between the seismic and acoustic amplitude spectra is low.

For both sources the array analysis is carried out by using the whole frequency content. The baz-s plot for the signal produced by source HP is shown in Fig. 6.23 a), the one for the H signal can be found in Fig. 6.23 b). A backazimuth of 180° was computed via array analysis for both, the H and the HP signal. This backazimuth value deviates from the backazimuth computed from the seismic data sets as well as from the actual location of shot point SP2 (cf. Fig. 6.12)

a)   b)
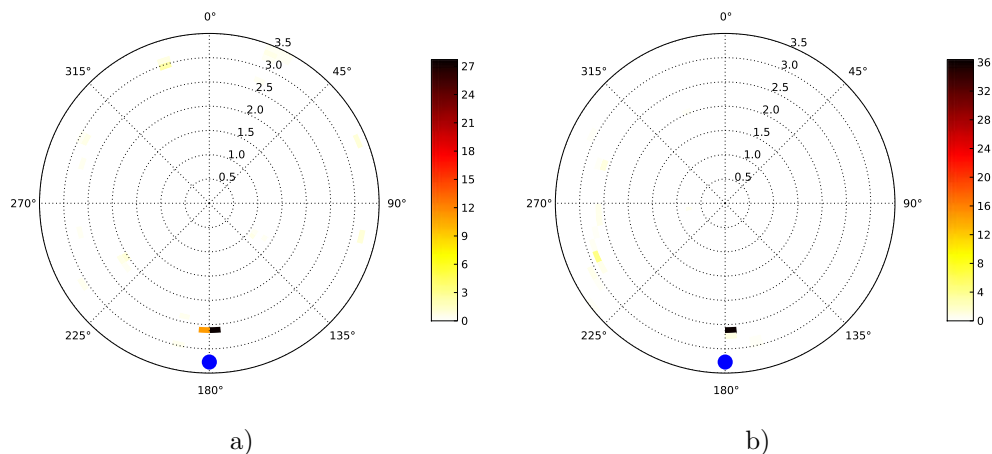
Figure 6.23.: *baz-s plots of the signals produced by sources HP and H at shot point SP2 observed with the KNH microphone array (actual backazimuth indicated by a blue dot):*
a) source HP
b) source H

From the baz-s plots shown in Fig. 6.23 the slowness of the acoustic wave is found to be approximately $2.65 \, \mathrm{s \, km^{-1}}$. Hence, the computed speed of sound would be about $380 \, \mathrm{m \, s^{-1}}$. Based on meteorological data collected during the experiment the speed of sound at standard conditions ($C_0 = 331.45 \, \mathrm{m \, s^{-1}}$) can be adjusted for the local atmospheric conditions during the experiment.

---

[3]Harry Nyquist (1889–1976) American physicist

According to Tab. 3.2 the increase of the speed of sound due to the measured temperature of $13\,°C$ and relative humidity of $80\,\%$ is approximately $3.0\,\%$. Hence, the adjusted speed of sound is about $340\,\mathrm{m\,s^{-1}}$. However, the discrepancy to the value determined via array analysis is still large ($40\,\mathrm{m\,s^{-1}}$). A possible reason may be the minimal array layout (only three traces available for array analysis).

Since the computed speed of sound is not reliable a velocity of $340\,\mathrm{m\,s^{-1}}$ is used to determine the source time of HP at shot point SP2. The record section in Fig. 6.24 contains the acoustic signals recorded at the KNH array stations. Due to the constellation of array and shot points two seismograms are shown at the same distance to the source. Only the signals of one hammer stroke with their corresponding envelopes are shown in the record section. The red line corresponds to an acoustic signal travelling across the KNH array at $340\,\mathrm{m\,s^{-1}}$. The first onsets in the acoustic seismograms coincide with the computed speed of sound. Hence, the determined source time can be considered as correct.
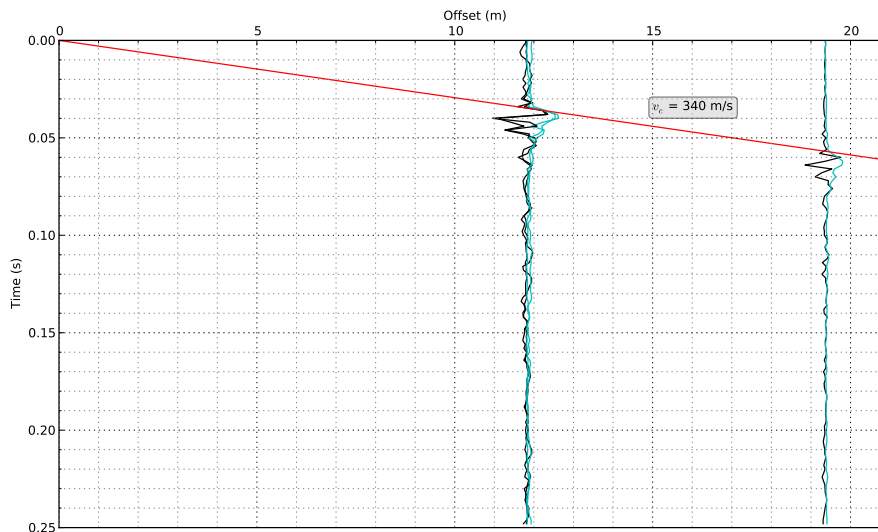
Figure 6.24.: *Record section depicting the a hammer stroke performed at shot point SP2 detected with the KNH microphone array:*
black   . . .   acoustic data
cyan   . . .   envelope
red   . . .   first arrivals

The record section in Fig. 6.25 contains the seismograms recorded at the KNH array stations. As for the acoustic data the signals produced by one hammer stroke and the corresponding envelopes are shown in the record section. By contrast to the microphone record section, two solid red lines and one dashed red line are shown in this diagram. The flatter solid line corresponds to the P wave travelling across the KNH array. The P wave velocity was computed as $1300\,\mathrm{m\,s^{-1}}$ from the slowness obtained via array analysis. Since the first onsets of the signals coincide with the flatter red line the slowness computed via array analysis can be considered as correct.

The surface wave velocity was computed as $240\,\mathrm{m\,s^{-1}}$ via array analysis and is illustrated by the steeper solid red line in the record section. Since the array analysis relies on the fk analysis the resultant slowness values are considered to be values of the phase slowness. As can be seen, the first red line does not correspond to any wave phase visible in the surface wave part of the signal. Based on the maximum amplitude peaks of the surface wave portion the surface wave slowness also was manually determined. From the resultant slowness value the corresponding surface wave velocity was found to be approximately $180\,\mathrm{m\,s^{-1}}$. The analytically and manually computed velocities differ by $50\,\mathrm{m\,s^{-1}}$. Both values are appropriate estimates for surface wave velocities. Although the slowness computed via array analysis differs from the actual phase velocity it still can be used for a valid identification of the wave type.
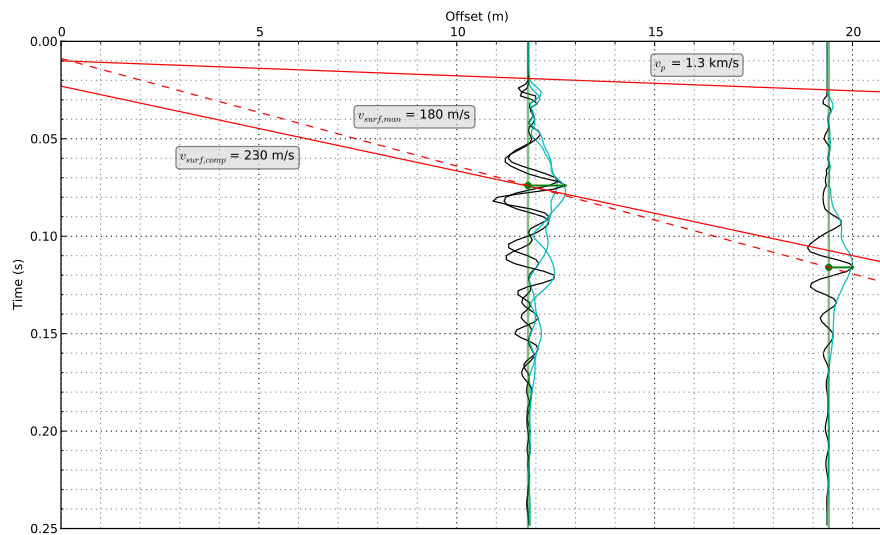
Figure 6.25.: *Record section depicting a hammer stroke at shot point SP2 detected with the KNH geophone array:*
black ... seismic data
cyan ... envelope
red ... first arrivals

6.2.2.2. Analysis of the signals produced by the low altitude acoustic source D

In this section the signals produced by the controlled low altitude acoustic source D are investigated. The main subject is to unveil information on how these acoustic signals are detected with the seismic and the acoustic sensor.

The signals produced by source D at shot point SP2 recorded with geophone and microphone as well as the corresponding spectrograms are visualized in Fig. 6.26 a) and Fig. 6.26 b), respectively. From these diagrams the waveforms of the signals produced by the drumbeats are found to be similar for the seismic and acoustic data sets. The amplitude of the signal in the acoustic data is higher than in the seismic data by the factor 10^2. Since source D is a pure acoustic source with no direct contact to the ground this characteristic is comprehensible.

The spectrograms show similar characteristics for the data recorded with the different types of sensors. A narrow frequency band with a main frequency of approximately 50 Hz is visible for both, the seismic and the acoustic data. The frequencies ranging from about 150 Hz to 200 Hz are more prominent in the frequency content of the seismic data than in the acoustic data although the seismic sensor should be more sensitive to low frequencies.
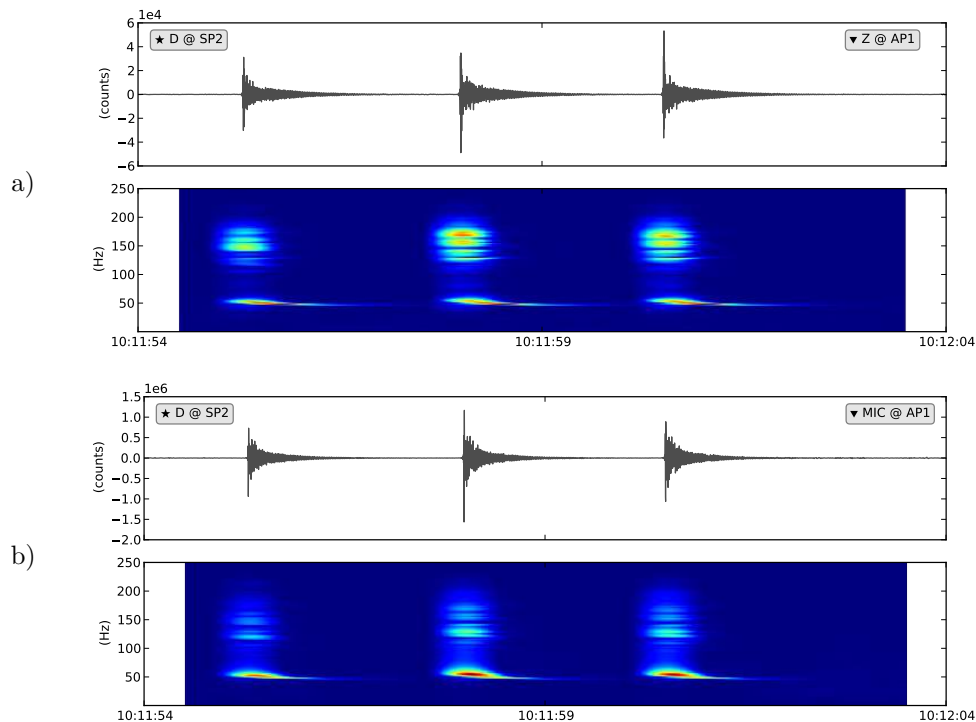
Figure 6.26.: *Signal and spectrogram produced by source D at shot point SP2 recorded at array point AP1:*
a) with the geophone's vertical component
b) with the microphone

The amplitude spectra shown in Fig. 6.27 provide a more detailed look at the frequency content of the data. Again the narrow low frequency band is visible for both types of sensor data with a more gentle slope towards higher frequencies for the microphone. The higher frequency band is depicted well in both amplitude spectra with a lower limit frequency of approximately 120 Hz.
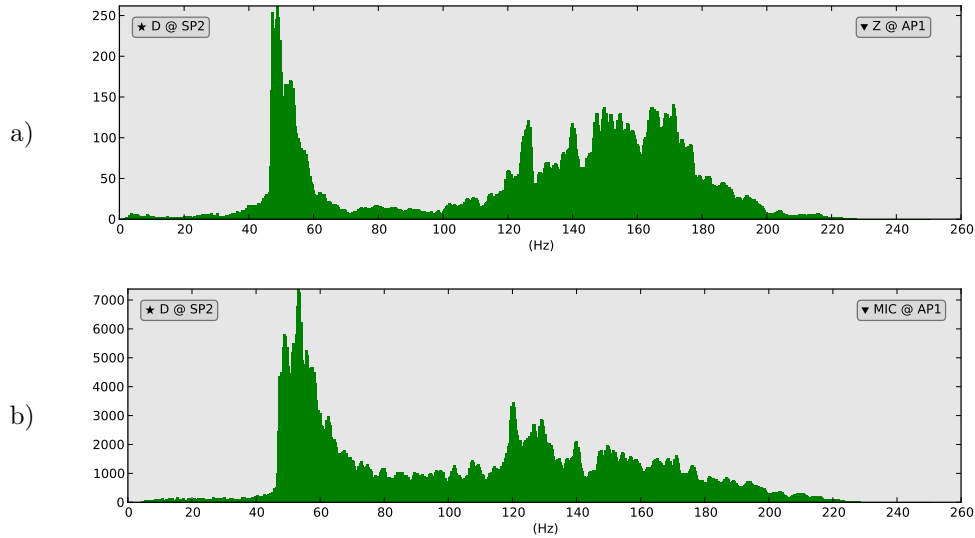
Figure 6.27.: *Amplitude spectrum of the signal produced by source D at shot point SP2 recorded at array point AP1:*
a) with the geophone's vertical component
b) with the microphone

From Fig. 6.27 a) the high proportion of the upper frequency band with respect to the low frequencies is distinctly visible. In case of the acoustic data the upper frequency band contributes less to the signal with respect to the low frequencies. A possible reason may be that the geophone measures the velocity of the ground movement whereas the microphone detects the sound pressure which corresponds to the ground displacement itself. The integrated seismic amplitude spectrum is shown in Fig. 6.28. Hence, this diagram illustrates the frequency content of the acoustic signal associated with the ground displacement. The high frequencies contribute to the signal to a lesser extent in case of the displacement than in case of the velocity of the displacement (with respect to the low frequency band). The integrated amplitude spectrum corresponds to the expectation of the seismic sensor being less sensitive in the high frequency range. Hence, the reason for the unexpectedly high contribution of the upper frequency band to the seismic data is the geophone being a velocity sensor. Since the differences between the geophone amplitude spectrum and the integrated amplitude spectrum are negligibly small the integration of the spectra is not necessary in order to compare the amplitude spectra of the seismic and acoustic data [4].

---

[4]See the computation of the amplitude spectra similarity in Sec. 6.3.2
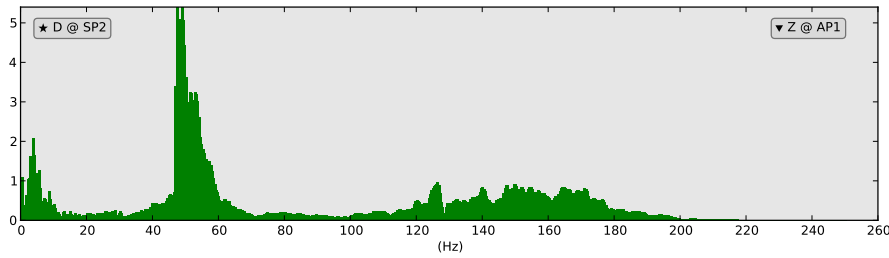
Figure 6.28.: *Integrated amplitude spectrum of the signal produced by source D at shot point SP2 recorded with the geophone's vertical component*

Fig. 6.29 provides a closer look at a drum beat performed at shot point SP2. According to the first arrivals the unprocessed signals are dominated by the waves arriving at the speed of sound. Waves arriving at higher speeds may be visible before the main-pulse of the sound-induced signal. Subsequently the term pre pulse oscillation (hereinafter referred to as PrePO) will be used to refer to this effect. A more detailed investigation of the PrePO will be carried out in this section later on. The most prominent feature in signals is the long-lasting post pulse oscillation (hereinafter referred to as PPO). Taking a look back at the spectrograms in Fig. 6.26 the PPO seems to oscillate at approximately 50 Hz. An important question concerning the PPO is how it influences the array analysis.

In order to separate the different portions of the signal produced by source D three windows were defined (see Fig. 6.29). The red one is used to extract the PrePO portion of the signal. Since the PrePOs are weak compared to the remaining part of the signal the window spans a relatively large time range, so even very weak signal parts are covered. The magenta coloured window covers the signal part that can be denoted as the main pulse. This portion is characterised by jagged high-frequency oscillations. By contrast the rear part of the signal (PPO) covered by the green coloured window consists of smooth oscillations at lower frequencies (as can be seen in the spectrograms).

The effect of the PrePO and the PPO on backazimuth and slowness can be determined by applying the main pulse window on the data before the array analysis is carried out. The baz-s plot computed for the unfiltered data is shown in Fig. 6.30 a). Based on this illustration it would be valid to assume a multitude of sources since at least five distinct slowness-backazimuth pairs are depicted. With the main pulse window applied to the data a different array analysis result is obtained as can be seen in Fig. 6.30 b). The phantom sources vanished and just the most probable backazimuth value (according to the location of SP2) remains visible in the baz-s plot. The associated slowness is within a range of $2.0\,\mathrm{s\,km^{-1}}$ to $2.3\,\mathrm{s\,km^{-1}}$. The acoustic data were used for the array analysis in the same way, namely once with the raw data and a second time with the main pulse window applied. The resultant baz-s plot for the raw data in Fig. 6.31 a) depicts the phantom sources already seen in Fig. 6.30 a), too. The difference in relative power of these phantom sources and the real source is larger than it is for the seismic data.
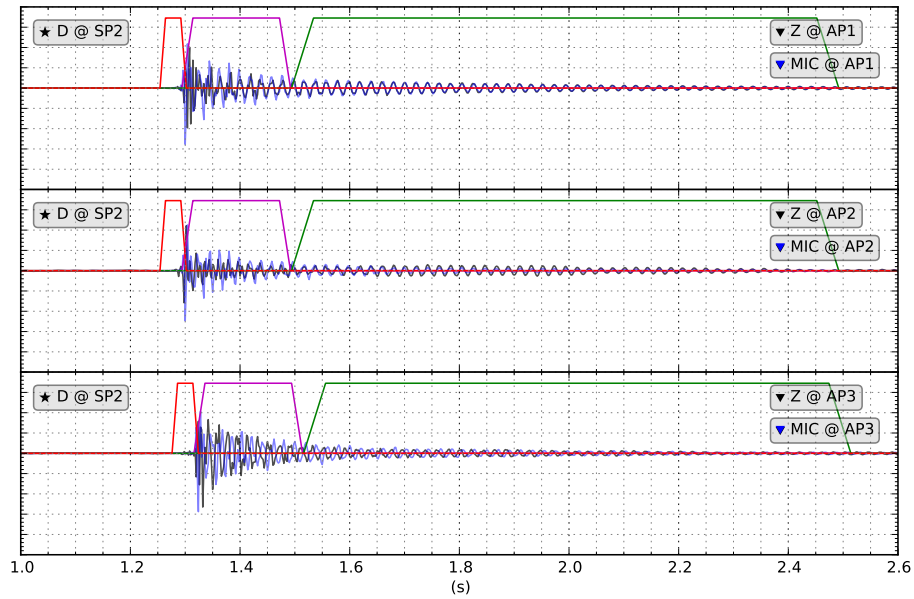
Figure 6.29.: *Signal produced by D (single drum beat) at shot point SP2 observed with the KNH geophone and microphone array:*

black	...	*seismic data*
blue	...	*acoustic data*
red	...	*PrePO filter*
magenta	...	*main pulse filter*
green	...	*PPO filter*

a)   b)
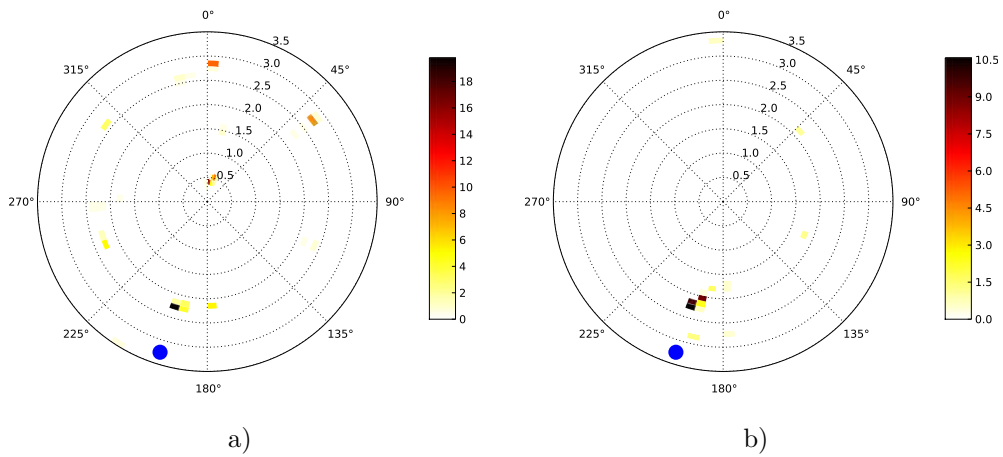
Figure 6.30.: *Effects of the main pulse window on the array analysis of KNH geophone array data (actual backazimuth indicated by a blue dot):*
a) raw data
b) main pulse window applied

Applying the main pulse window and rerunning the array analysis yields the baz-s plot presented in Fig. 6.31 b). As can be seen the phantom sources have vanished. By contrast to the results for the seismic data there is no significant change of the computed slowness values for the acoustic data with the main pulse window applied. Both baz-s plots in Fig. 6.31 indicate a slowness of about $2.6\,\mathrm{s\,m^{-1}}$ or expressed as velocity approximately $380\,\mathrm{m\,s^{-1}}$. This velocity deviates from the speed of sound at standard conditions (cf. Sec. 6.2.2.1). Comparing the backazimuth computed from the different sensor data unveils a difference of approximately $20°$.
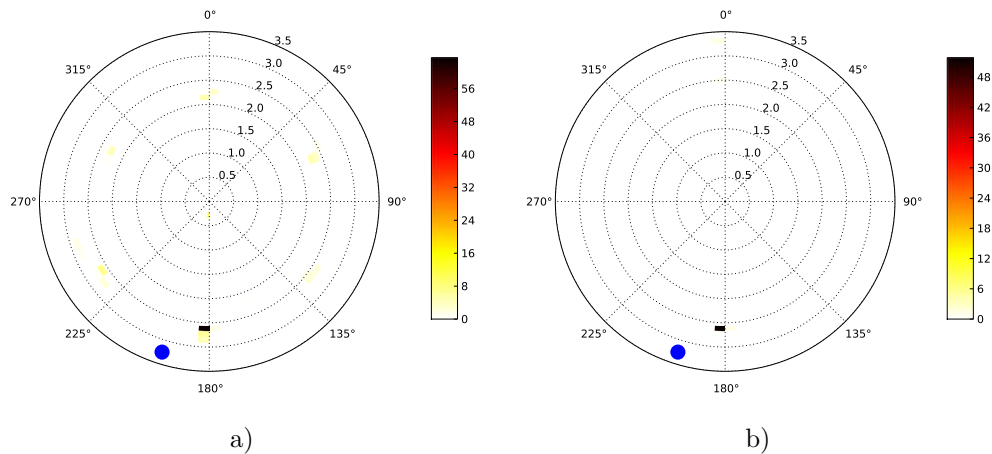
Figure 6.31.: *Effects of the main pulse filter on the array analysis of KNH microphone array data (actual backazimuth indicated by a blue dot):*
a) without filter
b) main pulse filter applied

The most interesting fact about the PPO is how it influences the results of the array analysis. Therefore, the PPO window is applied on the seismic and acoustic data sets and the array analysis is carried out for the seismic and acoustic data sets. The resultant baz-s plot for the seismic data set is shown in Fig. 6.32 a) whereas Fig. 6.32 b) contains the baz-s plot for the windowed acoustic data set. Note that the slowness range in the left baz-s plot is extended up to $6\,\mathrm{s\,km^{-1}}$ in order to be able to map high slowness values possibly associated with surface waves. Using just the PPO portion of the seismic signal yields similar backazimuth values for the seismic and acoustic data sets. The computed slowness is approximately $2.0\,\mathrm{s\,km^{-1}}$ or $500\,\mathrm{m\,s^{-1}}$. In case of the acoustic data set the applied PPO filter has no effect on the baz-s plot resulting from the array analysis. The computed seismic slowness of $2.0\,\mathrm{s\,km^{-1}}$ is slightly too low to be associated with a seismic body wave.

The computed slowness values indicate that surface waves are induced in the ground by source D. Thus, particle motion plots were used to verify the existence of surface waves. The particle motion in the R–Z plane for the main pulse portion of the seismic signal is shown in Fig. 6.33. The left particle motion plot relies on the unfiltered seismic data, whereas the right plot visualises the particle motion based on the bandpass filtered data.
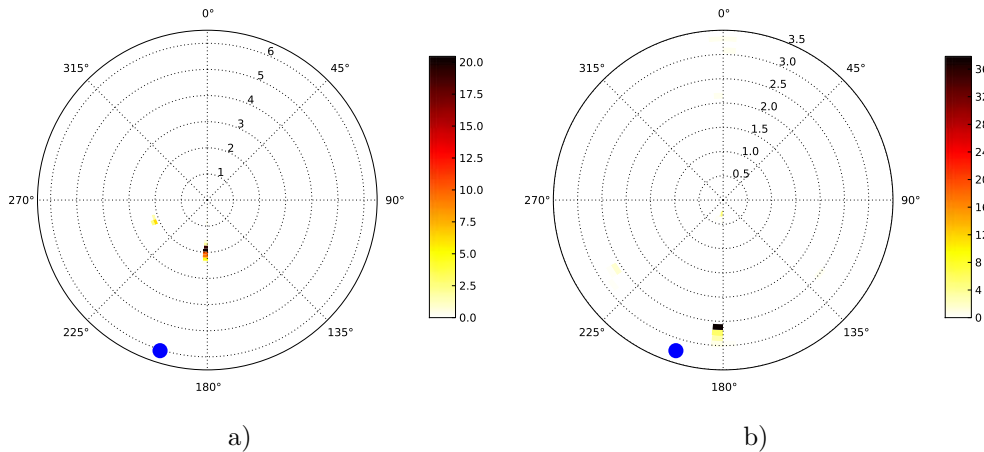
Figure 6.32.: *Effects of the PPO window on the array analysis (actual backazimuth indicated by a blue dot):*
a) KNH geophone array data
b) KNH microphone array data

The unfiltered seismic data exhibits no distinct particle motions. By contrast, a retrograde particle motion can be seen from the bandpass filtered seismic data. Since the illustrated particle motion does not resemble an upright elliptical retrograde motion the induced seismic wave can not be referred to as a Rayleigh wave. Based on the inclination of the particle motion and the slowness computed beforehand, the low altitude acoustic source induced SV waves in the ground.
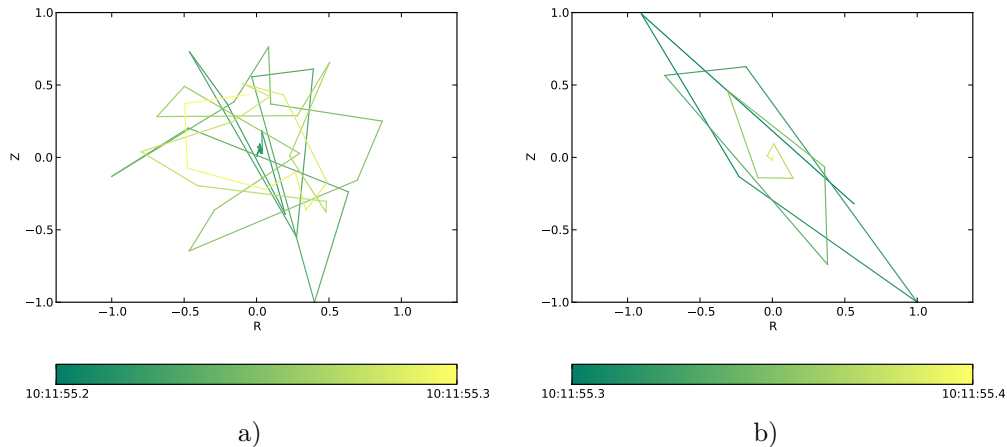
Figure 6.33.: *Particle motion associated with the main pulse of the signal produced by D*
at shot point SP2:
a) R–Z plane
b) R–Z plane (baz=200°, bandpass filtered)

The wave type corresponding to the PPO portion of the signal was also verified via particle motion plots. The particle motion of the raw seismic data set is shown in Fig. 6.34 a) whereas Fig. 6.34 b) illustrates the particle motion for the low pass filtered PPO portion. None of the plots shows a particle motion similar to Rayleigh waves. Neither for the main pulse nor for the PPO based on the particle motion no evidence for Love waves could be found.

a)

b)
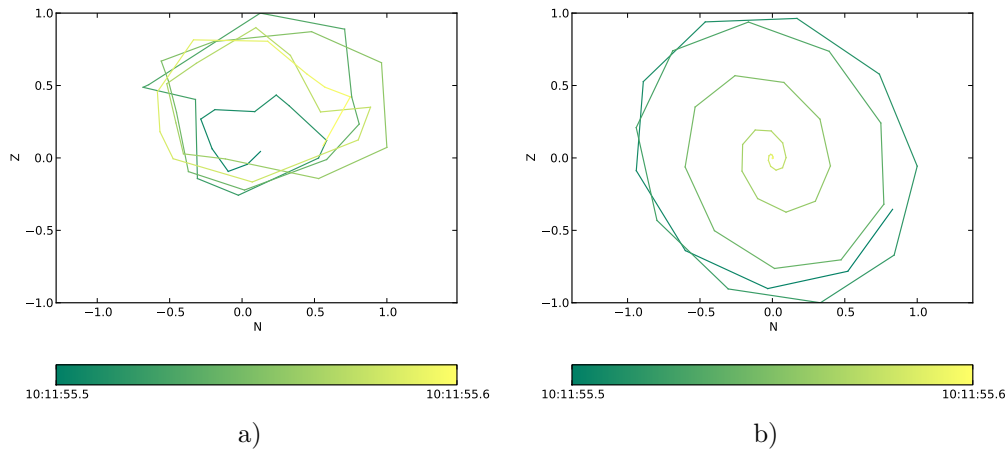
Figure 6.34.: *Particle motion associated with the PPO of the signal produced by D at shot point SP2:*
a) N–Z plane
b) N–Z plane (bandpass filtered)

It can be summarised that the low altitude acoustic source produced similar waveforms in both, the seismic and acoustic data and that the frequency content of the seismic and acoustic signals bear a high resemblance. Nevertheless, the slowness values computed from the seismic data were lower than the speed of sound and a particle motion similar to Rayleigh waves could be found for the main pulse portion of the signal. Hence, source D may have induced seismic surface waves in the ground.

Note, that for the PrePO no scientifically relevant results were found.

6.2.2.3. Analysis of the signals produced by a helicopter overflight

During the experiment a helicopter overflight was documented acting as a high altitude acoustic source. The helicopter crossed the KNH array from South-West to North-East. Since the time span of this event is known it is possible to extract the corresponding signal from the data. The signals produced by the helicopter overflight recorded with geophone and microphone and the corresponding spectrograms are depicted in Fig. 6.35 a) and Fig. 6.35 b), respectively. Generally, the waveform of the signal appears to be similar in the seismic and the acoustic data. However, the seismic signal amplitudes are lower than the amplitudes of the acoustic signal by the factor 10^1. The microphones produced a more detailed recording of the signal produced by the overflight while the seismic signal lacks some features that are visible in the acoustic data.

Valuable characteristics can be deduced from the spectrograms. Narrow frequency bands proceed parallel with time and are equally spaced in the frequency range. Due to bending of the frequency bands the interval between two adjacent bands is bigger for the first 30 s of the waveform than it is for the remaining signal portion. This frequency shift towards lower frequencies follows from the movement of the helicopter. The helicopter crossed the KNH array acting as a source moving relative to the observer. Hence, the bending of the frequency bands visible in the spectrograms is due to the Doppler effect. Whereas it may be difficult to recognise the present signal to be produced by a helicopter the corresponding spectrogram allows for a distinct identification of the signal source. Furthermore, it could be shown that by using spectrograms it is possible to discriminate between moving and stationary sources.

The amplitude spectra depicted in Fig. 6.36 a) and Fig. 6.36 b) are computed for the seismic and the acoustic data, respectively. The geophone amplitude spectrum depicts the frequency bands up to 70 Hz most clearly. For the remaining frequency range the bands visible in the spectrogram are indicated as little peaks. By contrast, the frequency bands are depicted well up to about 100 Hz for the acoustic data. Both spectra appear to be noisy above 120 Hz. As for the seismic amplitude spectrum for source D the proportion of the upper frequency range is surprisingly high in Fig. 6.36 a). An explanation was already given in the previous section. The seismic amplitude spectrum corresponding to the velocity of the ground movement can be considered to be sufficiently accurate for the present investigations.

A combined visualisation of the helicopter signal recorded with both types of sensors at each array point is presented in Fig. 6.37. In order to provide an useful comparison the seismic signals (black) and the acoustic signals (blue) are equally scaled. The overall similarity between the different sensor data can be seen from this illustration. The microphones seem to reproduce the signal more accurately since the visually evaluated similarity of the acoustic waveforms is high. In case of the seismograms the signal is reproduced with varying accuracy.

Figure 6.35.: *Signal and spectrogram produced by a helicopter overflight recorded at array point AP1:*
a) with the geophone's vertical component,
b) with the microphone

Figure 6.36.: *Amplitude spectrum of a helicopter overflight recorded at array point AP1:*
a) with the geophone's vertical component
b) with the microphone

81
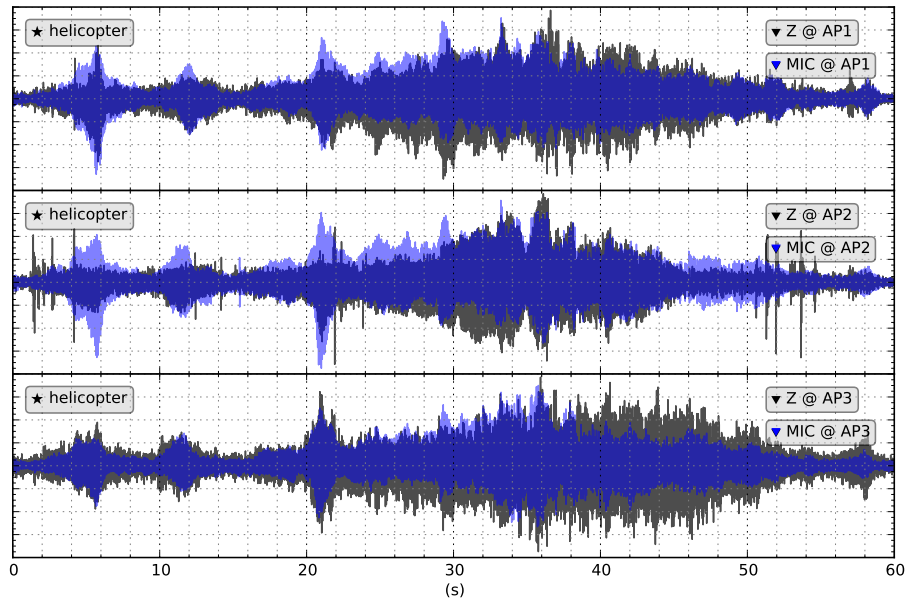
Figure 6.37.: *Signals produced by the helicopter overflight observed with the KNH array:*
black . . . seismic data
blue . . . acoustic data

Since frequencies of nearly up to the Nyquist frequency are contributing to the signals the array analysis was carried out with the unfiltered signals for both types of data. The resultant baz-s plots are provided in Fig. 6.38 a) for the seismic data and in Fig. 6.38 b) for the acoustic data. The resultant baz-s plot in Fig. 6.38 b) is more distinct than the one computed from the seismic data. Since the signal was recorded more accurately by the microphone this behaviour is comprehensible. However, from both data sets the helicopter overflight from South-West to North-East could be reconstructed.

A valuable fact is that besides the backazimuth values also the slowness values are identical for both data sets. That is contrary to the differing slowness values computed from the data sets containing the signals produced by the controlled sources HP, H and D. Another striking characteristic is the variation of slowness with the position of the helicopter. The low slowness values must not be mistaken for a seismic wave slowness. For helicopter positions near or directly above the KNH array the array analysis yields apparent slowness values which are lower than the actual slowness of the acoustic signals produced by the helicopter.

In order to obtain information on the wave types associated with the helicopter overflight the particle motion in the R–Z plane is illustrated for different backazimuth values. The succession of these values corresponds to the flight direction of the helicopter. The particle motion plots in Fig. 6.39 a) to c) unveil no distinct characteristics that can be associated with a seismic surface wave. Since the baz-s plots shown in Fig. 6.38 used a slowness range of up to $3.5 \, \mathrm{s \, km^{-1}}$ the slowness value corresponding to the surface wave portion may just not be illustrated.

Thus, the array analysis was carried out once again with an extended slowness range. The resultant baz-s plot is depicted in Fig. 6.38 c). As can be seen from this diagram there are no slowness values above $3.5\,\mathrm{s\,km^{-1}}$ which might indicated surface waves.

a)

b)

c)
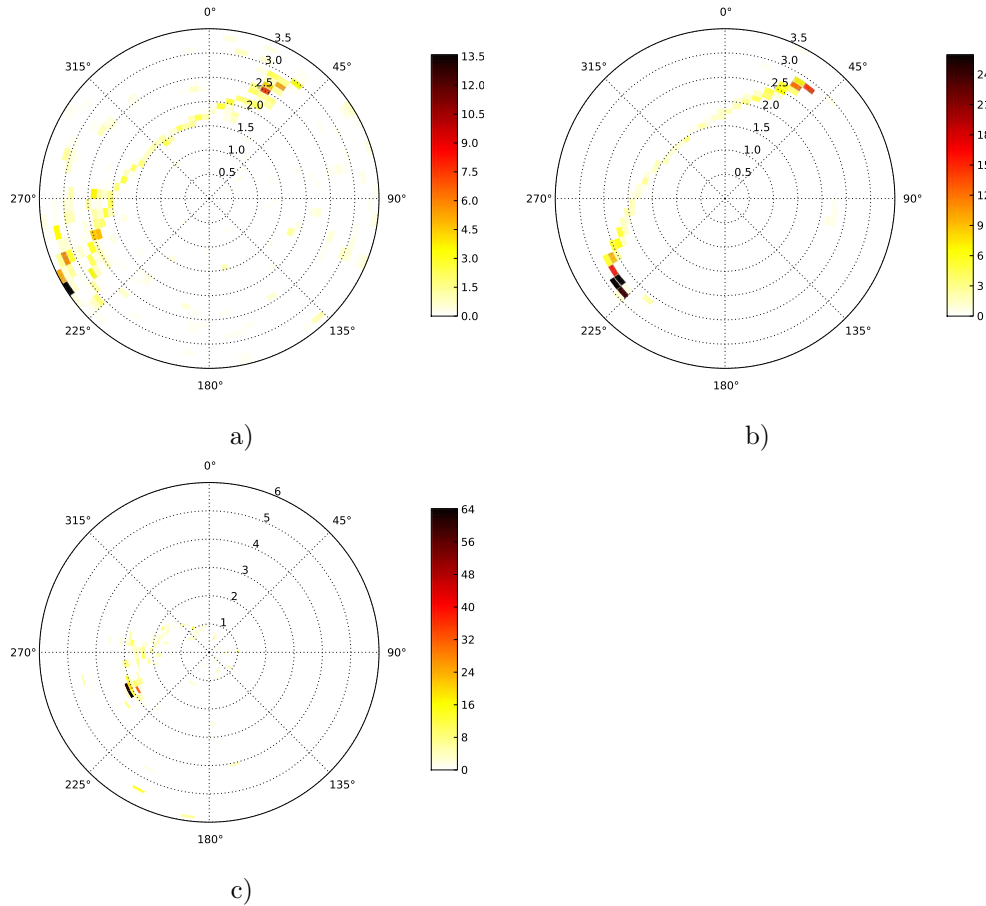
Figure 6.38.: *baz-s plots of signals produced by the overflight of a helicopter:*
a) observed with the KNH geophone array
b) observed with the KNH microphone array
c) extended slowness range (seismic data)

Based on the information obtained from the investigations presented in this section no evidence for seismic waves induced by the helicopter could be found. Most probably the sound pressure emitted by the helicopter produced ground movement nearby the geophone site. By contrast to the low altitude acoustic source, an acoustic source at higher altitudes can be considered as a source type that does not induce any type of seismic wave.
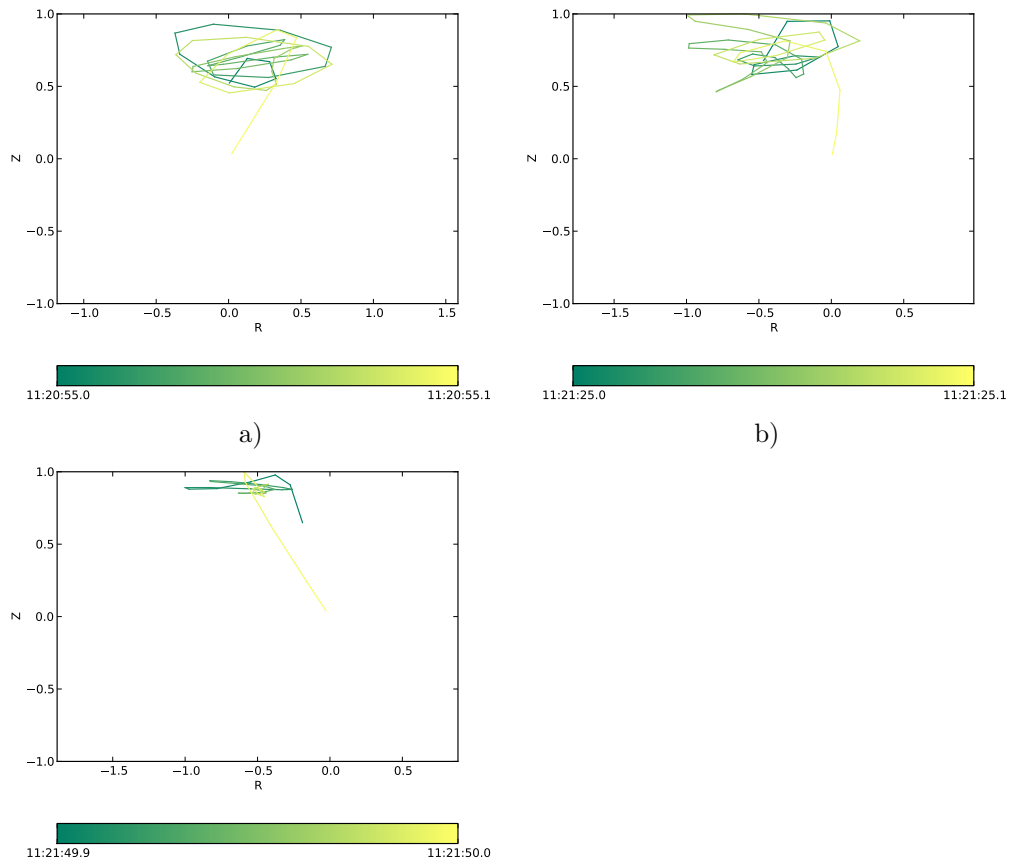
Figure 6.39.: *Particle motion in the R–Z plane associated with the helicopter overflight (low-pass filtered data):*
a) baz=240° b) baz=30° c) baz=315°

6.2.2.4. Analysis of the signals produced by a passing bus

The bus stop in front of the Knödelhütte area (eastwards of the KNH array) is periodically served by a bus. In this section the signals produced by the bus passing the KNH array are investigated. A map depicting the locations of the KNH array (blue dot) and the bus stop (red rectangle) as well as the route (grey line) and the direction (black arrows) of the passing bus is shown in Fig. 6.40.

Figure 6.40.: *Locations of the KNH array (blue dot) and the bus stop (red rectangle) as well as the route (grey line) and the driving direction (black arrows) of the passing bus*

The signals produced by the passing bus recorded with geophone and microphone and the corresponding spectrograms are depicted in Fig. 6.35 a) and Fig. 6.35 b), respectively. Although the acoustic amplitude is higher seismic amplitudes by the factor 10^1, the latter one appears to contain a lower noise level. Based on the acoustic signal and spectrogram the passing of the bus can be described in detail. Approximately the first 20 s of the signal depict the bus approaching the bus stop. The bus stays at the stop for about ten seconds visible as the part of the signal without any oscillations except for the noise. Afterwards the bus continues its tour producing the signals visible in the last 15 s of the data set. This characteristic features of the signal structure can also be found in the seismic data. From a seismic point of view the seismic signal part corresponding to the deceleration of the bus is expected to be of higher amplitude than the acceleration of the bus. This may be explained by the reaction of the ground to dominant initial forces during braking.

By contrast, the comparatively low speed during the acceleration of the bus causes weaker ground motion. From an acoustic point of view the signal part related to the acceleration of the bus is expected to be of higher amplitude due to the louder engine noise in the acoustic data. Both assumptions can be verified by the recorded waveforms.
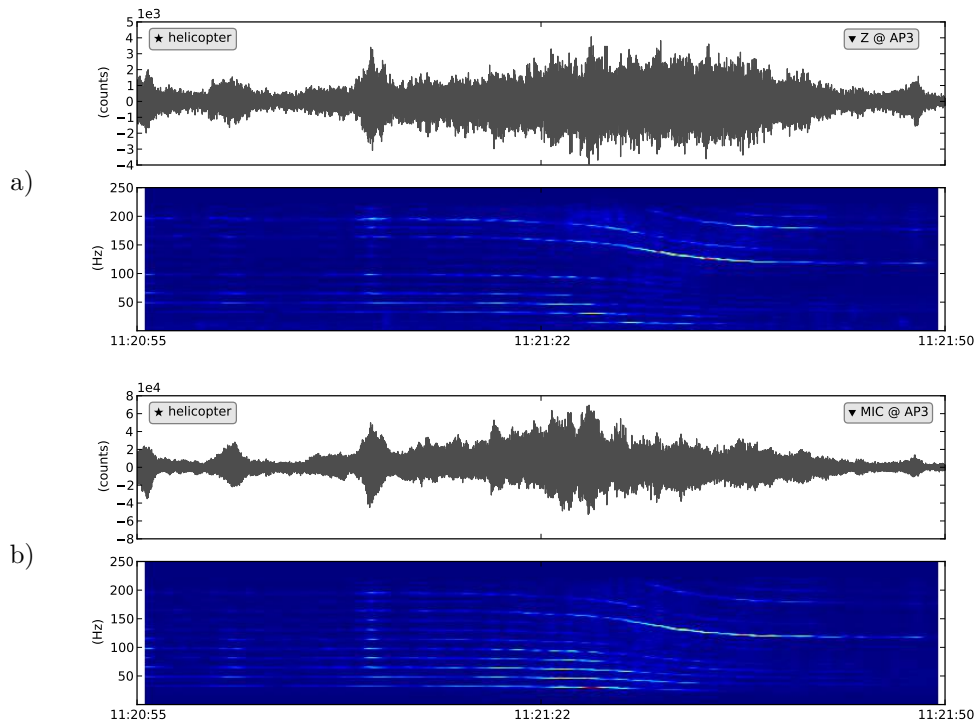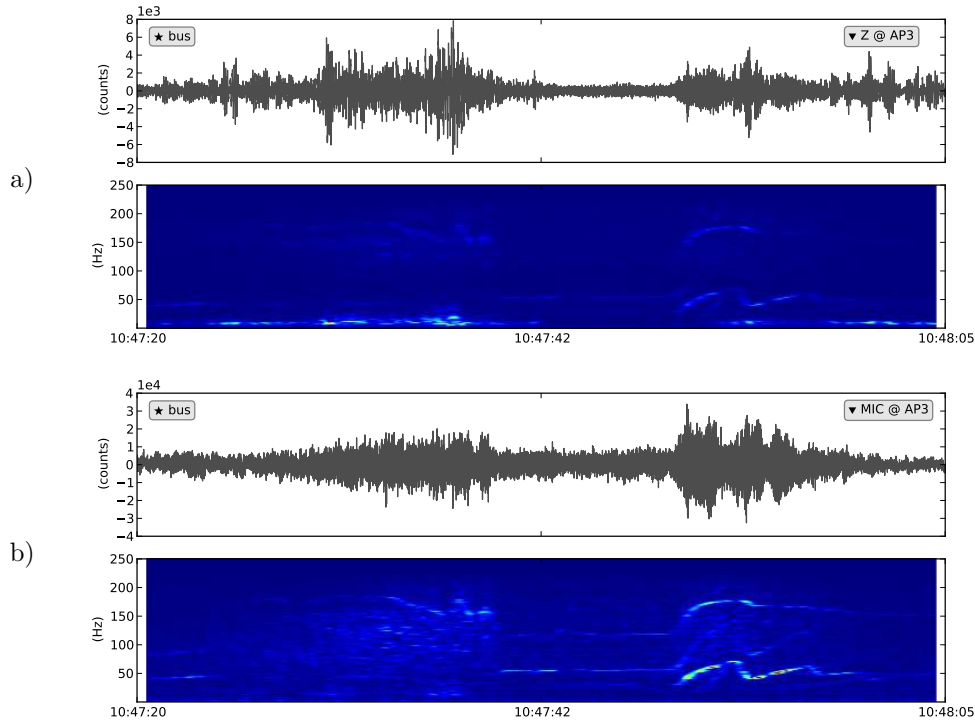

Figure 6.41.: *Signals and spectrograms produced by the passing bus recorded at array point AP1:*
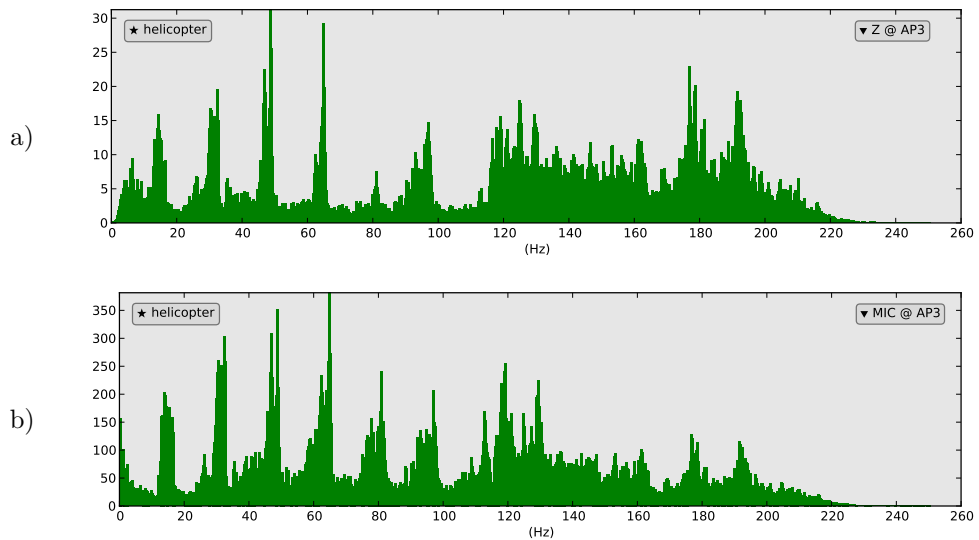*a) with the geophone's vertical component*
b) with the microphone

The spectrograms unveil further signal characteristics in the frequency domain. Based on the seismic data spectrogram shown in Fig. 6.41 a) it seems arguable to relate the strongest ground motion to the brake application. A corresponding maximum in the acoustic spectrogram does not exists. This behaviour seems to be correct since braking produces little noise but strong initial forces. The microphone spectrogram depicted in Fig. 6.41 b) features a wave-like shaped pattern that is most prominent in the frequency range of about 40 Hz to 60 Hz. This pattern is due to gentle increases of the frequency with time followed by sudden drops of the frequency. A process associated with the acceleration of the bus that can be related to this frequency-domain characteristic is gear change. Hence, the acceleration of the bus accompanied by increasing engine rpm[5] is responsible for the increasing frequency of the emitted engine sound. The gear change itself reduces the engine rpm causing an instantaneous drop of the engine sound frequency.

---

[5]rotations per minute

Since the acceleration mainly produces acoustic signals it is visible in the acoustic data more clearly than in the seismic data.

The illustration shown in Fig. 6.42 provides a combined visualisation of the seismic data (black) and the acoustic data (blue) clearly unveiling the differences of the signals. The deceleration of the bus is depicted more detailed by the geophones, whereas the microphones recorded the acceleration more precisely. The acoustic data comprise a high noise level during the stay of the bus at the bus stop, whereas for the seismic data the noise level for this time range is low. The higher noise level in the acoustic data may be explained by the running engine emitting sound detectable by the microphones but not inducing vibrations strong enough to be detected by the geophones.
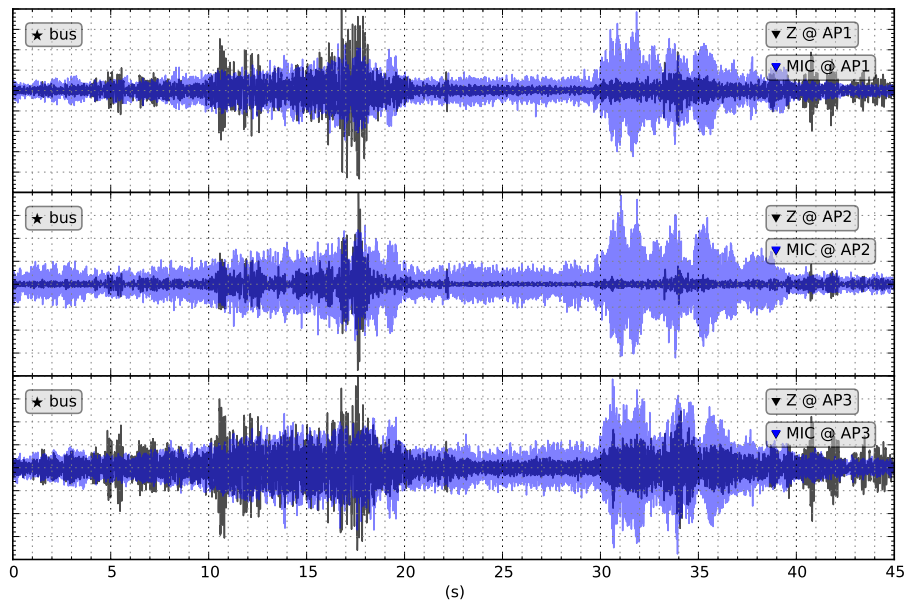
Figure 6.42.: *Signals produced by the passing bus observed with the KNH array:*
black   ...   seismic data
blue   ...   acoustic data

Since the deceleration and acceleration of the bus produce signals with different characteristics in the time- and frequency-domain these events are treated separately in the subsequent processing steps.

The amplitude spectrum of the signal produced by the decelerating bus is shown for the seismic and the acoustic data in Fig. 6.43 a) and Fig. 6.43 b), respectively. Comparing the different amplitude spectra unveils that the low frequencies associated with the braking of the bus can only be found in the seismic data set. The low frequencies are found to be gathered around 10 Hz. The overall similarity between the seismic and acoustic amplitude spectra is low.
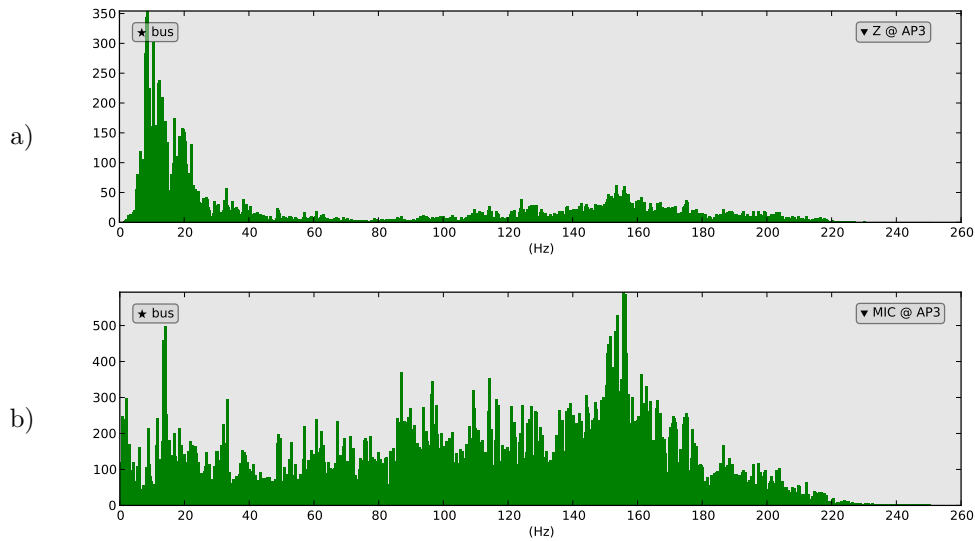
Figure 6.43.: *Amplitude spectrum of the signal produced by the braking of the bus:*
a) recorded with the geophone's vertical component
b) recorded with the microphone

The amplitude spectrum of the signal produced by the accelerating bus is shown for the seismic data and the acoustic data in Fig. 6.44 a) and Fig. 6.44 b), respectively.

As for the deceleration of the bus the seismic amplitude spectrum is dominated by low frequencies gathered around 10 Hz. The low frequency peak can also be seen in the seismic spectrogram and is related to the first gear change (reaction of the ground to strong initial forces). From the acoustic amplitude spectrum it can be deduced that the acceleration of the bus produces signals with frequencies between 40 Hz to 60 Hz. While the amplitude spectra similarity is low for frequencies below 40 Hz the spectra bear a high resemblance in the higher frequency range. The frequencies associated with the engine noise are clearly visible in the seismic amplitude spectrum, too.

Since the bus is a source of seismic and acoustic signals the array analysis may yield different slowness values for the seismic data. For the acoustic data the array analysis should give a slowness approximately corresponding to the speed of sound. From the map shown in Fig. 6.40 the backazimuth values are expected to range from 10° to 80° for the deceleration of the bus and from 90° to 120° for the acceleration of the bus.

In order to be able to compute high slowness values associated with the seismic signals produced by the passing bus the array analysis was also carried out with extended slowness ranges. The resultant baz-s plot illustrating slowness values up to $5.0 \, \mathrm{s \, km^{-1}}$ is shown in Fig. 6.45 a). As can be seen the seismic waves propagate across the KNH array with a constant slowness of approximately $2.0 \, \mathrm{s \, km^{-1}}$. From this illustration the backazimuth range covered by the passing bus is found to be approximately 0° to 135°.
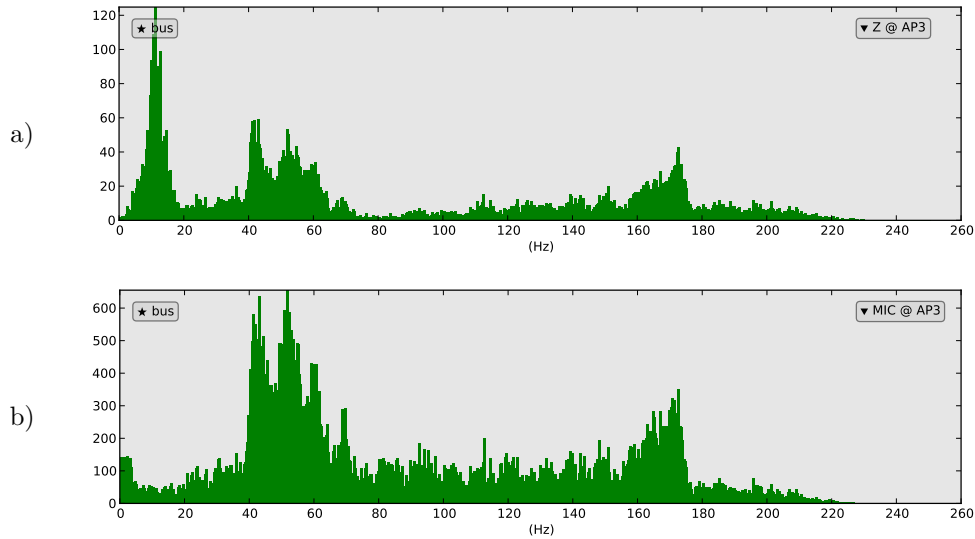
Figure 6.44.: *Amplitude spectrum of the signal produced by the acceleration of the bus:*
a) recorded with the geophone's vertical component
b) recorded with the microphone

Since surface waves might propagate at even higher slownesses the array analysis was carried out again with an slowness range up to $6.0\,\mathrm{s\,km^{-1}}$. The resultant baz-s plot shown in Fig. 6.45 b) does not exhibit high slowness values either.

As a consequence, all baz-s plots subsequently shown illustrate the standard slowness range of up to $3.5\,\mathrm{s\,km^{-1}}$.

The resultant baz-s plots of the array analysis using the unfiltered seismic and acoustic data containing the braking of the bus are presented in Fig. 6.46.

The backazimuth values computed from both sensor data perfectly describe the positions of the approaching bus. For the seismic data (Fig. 6.46 a)) the computed slowness values range approximately from $1.9\,\mathrm{s\,km^{-1}}$ to $2.5\,\mathrm{s\,km^{-1}}$. This slowness values are lower than the slowness values corresponding to acoustic waves. Hence, the deceleration of the bus can be considered of producing seismic waves. Due to the computed slowness range the induced seismic waves may be referred to as surface waves. The slowness values computed from the acoustic data (Fig. 6.46 b)) are approximately $2.85\,\mathrm{s\,km^{-1}}$ for the whole backazimuth range. Hence, the sound emitted by the bus could be detected by the KNH microphone array. A comparison of the baz-s plots shows that the array analysis yielded different slowness values for the different sensor data. Furthermore, the backazimuth and slowness values computed from the acoustic data are more distinct.

The resultant baz-s plots of the array analysis using the seismic data containing signals produced by the acceleration of the bus are shown in Fig. 6.47. In this case unfiltered (Fig. 6.47 a)) and bandpass-filtered (Fig. 6.47 b)) data were processed.

a)   b)
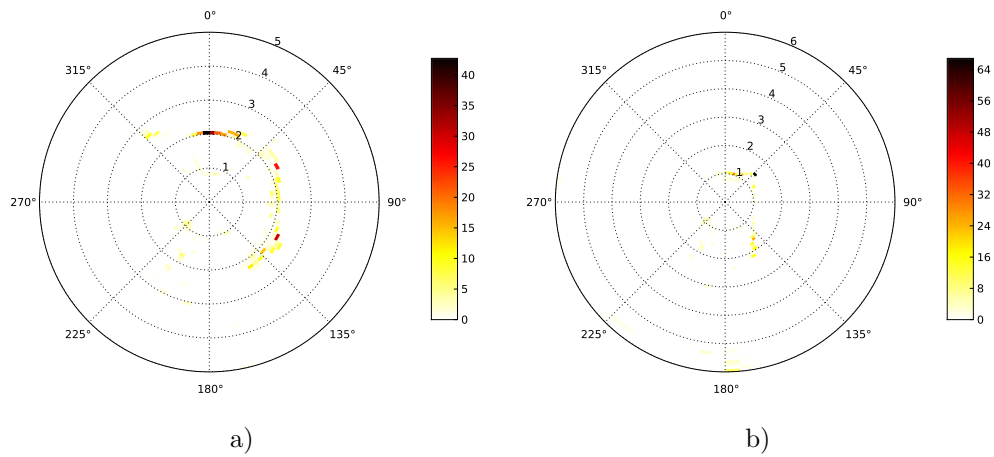
Figure 6.45.: *baz-s plot of the signals produced by the passing bus observed with the KNH*
geophone array:
a) slowness range up to $5\,\mathrm{s\,km^{-1}}$
b) slowness range up to $6\,\mathrm{s\,km^{-1}}$

a)   b)
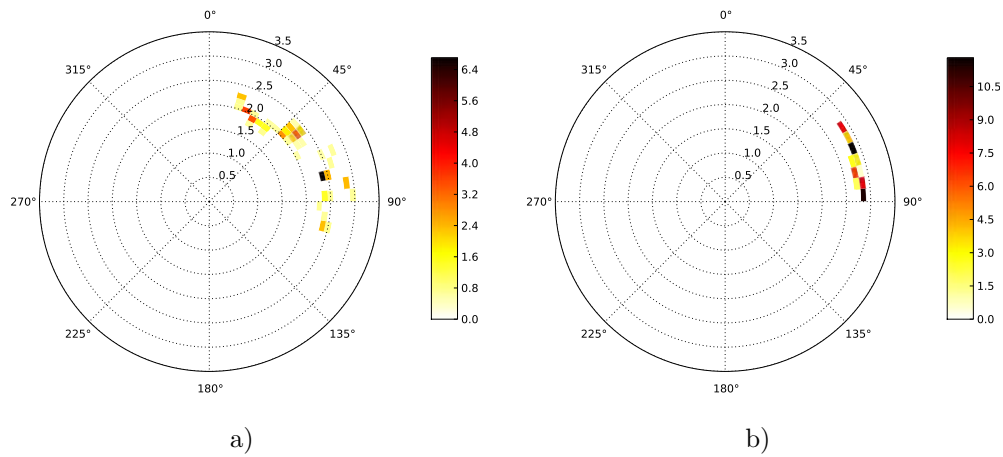
Figure 6.46.: *Braking of the passing bus detected with the KNH array:*
a) unfiltered seismic data
b) unfiltered acoustic data
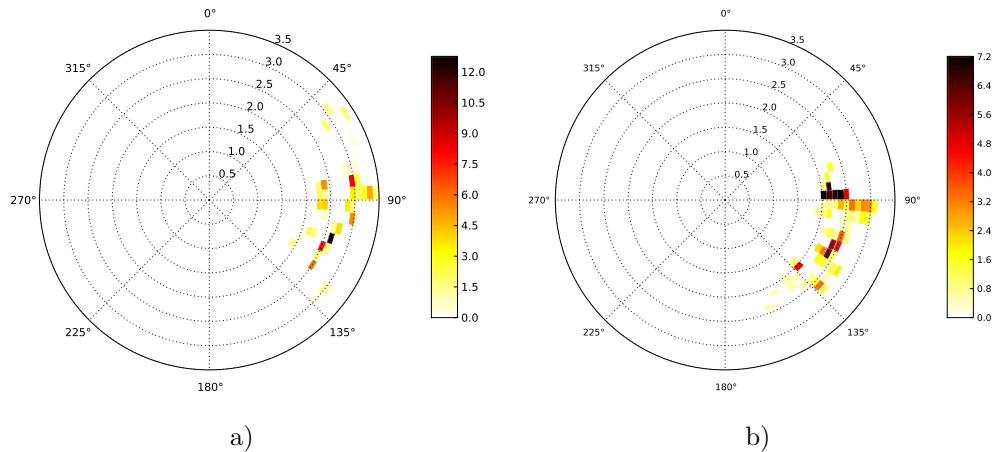
Figure 6.47.: *Acceleration of the passing bus detected with the KNH geophone array:*
   a) unfiltered
   b) 0.5 Hz to 20 Hz bandpass-filtered

For the unfiltered data the slowness values are not defined as clearly as for the braking of the bus. The slowness values approximately range from $2.25\,\mathrm{s\,km^{-1}}$ to $2.7\,\mathrm{s\,km^{-1}}$. By contrast, the computed backazimuth corresponds well to the positions of the bus leaving the bus stop.
By using the 0.5 Hz to 20 Hz bandpass-filtered seismic data the computed slowness values approximately range from $2.0\,\mathrm{s\,km^{-1}}$ to $2.6\,\mathrm{s\,km^{-1}}$, whereas the relative energy primarily indicates slowness values lower than $2.5\,\mathrm{s\,km^{-1}}$.

Based on the acoustic data containing the acceleration of the bus the array analysis yields the baz-s plots shown in Fig. 6.48. As for the seismic data the array analysis was carried out with unfiltered and bandpass-filtered data. Whereas the unfiltered acoustic data yields no distinct results for backzimuth and slowness as can be seen from the baz-s plot shown in Fig. 6.48 a), the 0.5 Hz to 30.0 Hz bandpass-filtered data set gives a backazimuth range roughly corresponding to the one computed from the seismic data. Although the computed slowness values vary around $3.0\,\mathrm{s\,km^{-1}}$ in some cases the values are slightly too high. From the frequency analysis the main frequencies were found to be 40 Hz to 60 Hz. Surprisingly the baz-s plot resulting from the array analysis using accordingly filtered data is not as distinct as expected (cf. Fig. 6.48 c)). Nevertheless, based on the already defined backazimuth the slowness value can be determined as approximately $2.8\,\mathrm{s\,km^{-1}}$.

The seismic wave type produced by the passing bus can be determined via particle motion plots. The particle motions caused by the braking of the bus in the E–N and the R–Z plane are shown in Fig. 6.49 a) and Fig. 6.49 b), respectively. The particle motions in the E–N plane partly coincide with the backazimuth range associated with the braking of the bus indicated by the blue arc (cf. Fig. 6.40). From this diagram it is not possible to verify the expected horizontal force produced by the bus.

a)

b)

c)
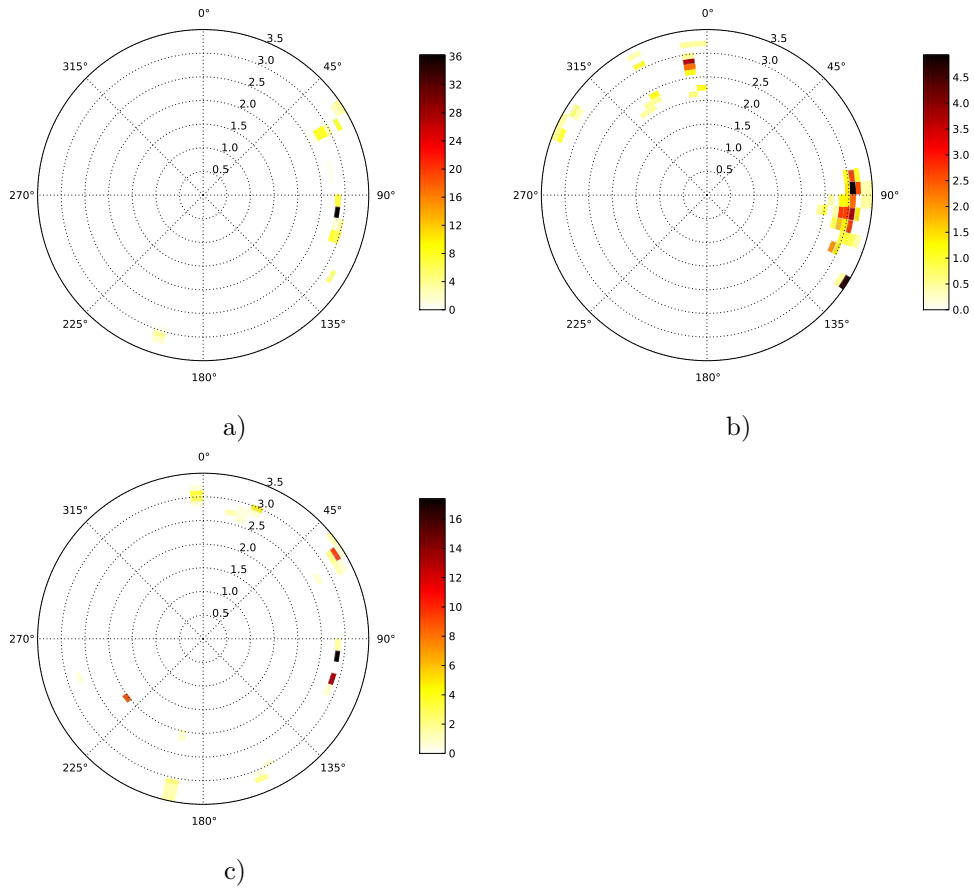
Figure 6.48.: *Acceleration of the passing bus detected with the KNH microphone array:*
a) unfiltered
b) 0.5 Hz to 30 Hz bandpass-filtered
c) 40 Hz to 60 Hz bandpass-filtered

a)

b)
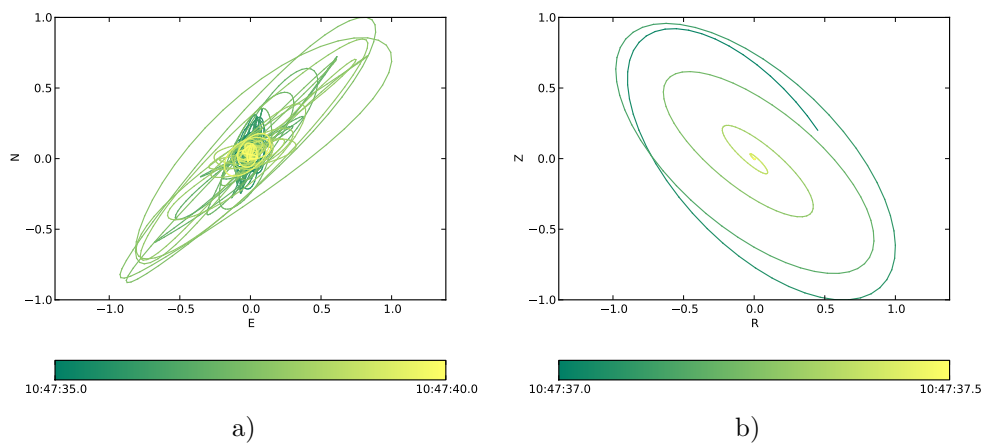
Figure 6.49.: *Particle motions associated with the braking of the bus (the blue arc indicates the corresponding backazimuth range):*
a) E–N plane (low-pass filtered)
b) R–Z plane (baz=80°, bandpass filtered)

In order to obtain the radial and transversal components the seismograms were rotated by 80° (indicated by the marker on the arc) towards the source. The chosen backazimuth does not coincide with the backazimuth range indicated by the particle motion, but was deduced from the previously shown baz-plots.

Rotating the seismograms towards the source provides the possibility to illustrate further wave characteristics. The diagram shown in Fig. 6.49 b) shows a retrograde elliptical particle motion. Due to the inclination of the ellipse the wave cannot distinctly be referred to as a Rayleigh wave. Most probably, the particle motion indicates a superposition of Rayleigh and SV waves.

The particle motions caused by the acceleration of the bus in the E–N and the R–Z plane are shown in Fig. 6.50 a) and Fig. 6.50 b), respectively. As previously discussed the acceleration process induces less and weaker seismic signals in the ground. The left diagram visualises the particle motion associated with the seismic signals induced by the gear change. The backazimuth range associated with the acceleration of the bus is illustrated by the blue arc. As can be seen the particle motion roughly corresponds to the known backazimuth range. In order to obtain the radial and transversal components the seismograms were rotated by 115° (indicated by the marker on the arc) towards the source. The plot on the right side shows the particle motion corresponding to the gear change and indicates a superposition of Rayleigh and SV waves (as for the deceleration of the bus).

a)   b)
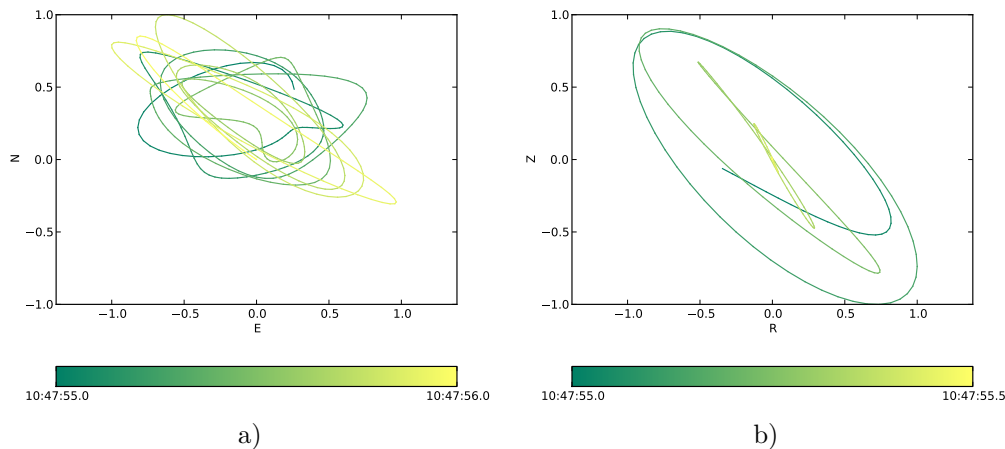
Figure 6.50.: *Particle motions associated with the acceleration of the bus (the blue arc indicates the corresponding backazimuth range):*
a) E–N plane (low-pass filtered
b) R–Z plane (baz=115°, bandpass filtered)

Hence, for both events, the deceleration and acceleration of the bus, similar wave types could be verified. Nevertheless, this result should be viewed with caution, since the used seismic sensors (geophones) are not well suited for the detection of signals produced by the passing bus. The duration of the bus passing the KNH array is several seconds. As a consequence, broadband seismic sensors would be a more appropriate choice for the observation.

6.3. Classification of source types

Based upon the results of the data analysis discussed above attempts to (automatically) classify signal sources are described in this section.

6.3.1. Amplitude ratio

Amongst other things, the analysis of the data recorded at the Knödelhütte lead to information on the amplitudes of the signals produced by different sources recorded with different sensor types. The possibility to identify signal sources based on the ratio of seismic and acoustic signal amplitudes was already proposed in Sec. 4.1. The amplitude ratio method should provide an instantly available and statistically reliable identification criterion. Hence, it should rely on the unprocessed raw data and utilise robust statistical methods.

Measuring maximum amplitudes can be done by using defined time windows for long lasting signals. If the signal is limited to a short time period only one amplitude value should be picked. The maximum amplitudes taken from seismic and acoustic data are used to compute the dimensionless amplitude ratio as

$$A_{ratio} = \frac{A_{seismic}}{A_{acoustic}} \tag{6.1}$$

If a large set of amplitude ratios is computed from signals produced by a certain source or source class descriptive statistics can be used to obtain estimates for the center value and the variability of this data set. Since the amplitude ratio method is expected to be statistically robust the median of the data set should be used to define the center value. The variability within the data set related to the median is the MAD (median absolute deviation)

$$\mathrm{MAD} = \mathrm{MED}(\mathbf{A}_{ratio} - \mathrm{MED}(\mathbf{A}_{ratio})) \tag{6.2}$$

By using the small but heterogeneous database created during the KNH experiment the usability of this source classification method can be verified. Each of the three controlled sources (D, HP, H) was applied three times in a row at five shot points. The produced signals were recorded at three array stations yielding a total of 45 seismic and 45 acoustic events. With the maximum amplitudes measured for each event 45 amplitude ratios can be computed. In order to reduce the influence of outliers in the data the median is used to find the representative center value of the signals produced by the different source types[6]. The median and MAD of the amplitude ratios computed for the controlled sources (D,HP,H) are summarized in Tab. 6.1. The signals produced by the helicopter overflight and the passing bus investigated in the previous sections are also used for computing amplitude ratios.

---

[6]The specific amplitude values as well as the computed amplitude ratios are given in the appendix (Sec. B.1)

The median and the MAD of the amplitude ratios computed for these uncontrolled but still artificial sources are shown in Tab. 6.1, too. As assumed the amplitude ratio can be used as a identification criterion since the computed values for the various sources are different. The signals produced by mainly seismic sources HP, H and the bus (brake) yield high amplitude ratios. By contrast, the amplitude ratios are low if computed for the signals produced by the (mainly) acoustic sources D, helicopter and bus (acc.).

Especially for the discrimination of controlled sources HP and H as well as for the different phases of the bus movement significant results were obtained. By comparing the amplitude ratios for HP and H it is possible to discriminate these source types (seismic-acoustic surface source and seismic surface source). Furthermore, the amplitude ratio indicates that source HP emitted more sound than source H. This corresponds to the actual behaviour of theses sources.

Since the deceleration and the acceleration of the bus were already discriminated before these processes were treated separately for the computation of the amplitude ratios, too. Although, the median values are less distinguishable than for the controlled sources there is still a difference between the two cases. As for the controlled sources the lower amplitude ratio was computed for the event that produced a higher amount of sound (acceleration of the bus).

Table 6.1.: *Median value (MED) and MAD of amplitudes ratios of different signal sources*

source	MED	MAD
helicopter	0.0500	0.0100
D	0.0247	0.0070
bus (acc.)	0.1300	0.0200
bus (brake)	0.2600	0.0300
HP	1.1282	0.6534
H	2.9678	1.0185

6.3.2. Amplitude spectrum similarity

As suggested in Sec. 4.1 the similarity of amplitude spectra computed from the seismic and acoustic data produced by a source may be used as an source classification criterion. A profound analysis of the frequency content of the signals produced as part of the Knödelhütte experiment was carried out in the previous sections. In order to provide the possibility of a visual inspection of the amplitude spectra similarity (ASS) for different source types the amplitude spectra produced by the investigated sources are shown in Fig. 6.51. The seismic spectra are depicted on the left side and the acoustic spectra on the right side of the figure. The amplitude spectra are sorted by the visually estimated similarity level starting with the highest one. From this overview it can be easily seen that the ASS is dependent on the source type and is highest for (mainly) acoustic sources.

The ASS is obtained by computing the correlation coefficient for each amplitude spectra pair.

In total 15 values are obtained for each controlled source (signals produced at five shot points detected at three array points)[7]. In order to provide an robust estimate for the center value and the variability of the correlation coefficients the median and the MAD are computed. The ASS is also computed for the amplitude spectra of the signals produced by the helicopter overflight and the passing bus discussed in the previous sections. The resultant values are summarised in Tab. 6.2. The (mainly) acoustic sources D, helicopter and bus (acc.) yield a high value for the amplitude spectrum similarity while the (primarily) seismic sources HP, H and bus (brake) yield lower values.

seismic data   acoustic data
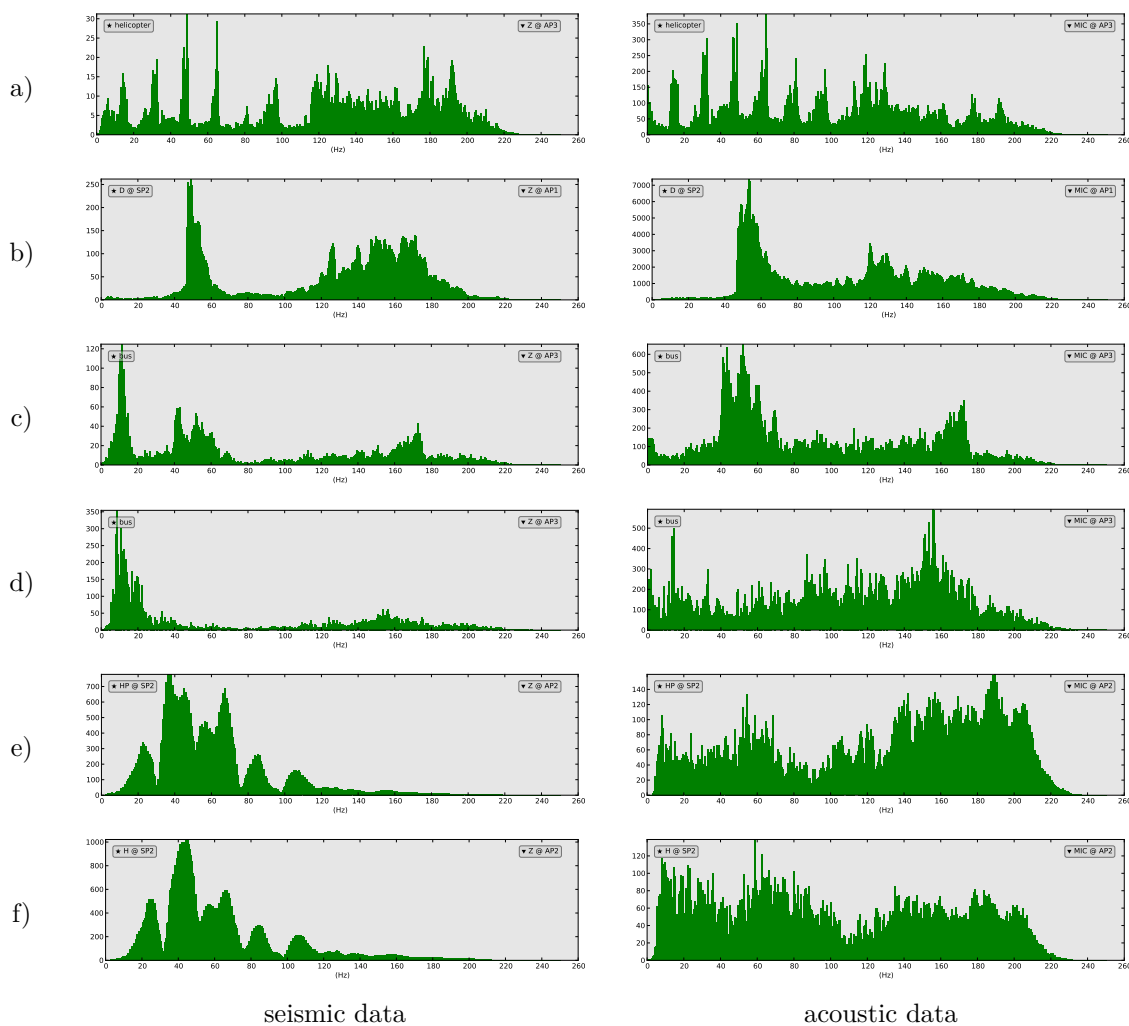
Figure 6.51.: *Comparison of seismic and acoustic amplitude spectra:*

a)	*...*	*helicopter*	*b)*	*...*	*D*
c)	*...*	*bus (acc.)*	*d)*	*...*	*bus (brake)*
e)	*...*	*HP*	*f)*	*...*	*H*

---

[7]The specific values are given in the appendix (Sec. B.4)

Based on the ASS, a clearer distinction of the deceleration and the acceleration of the bus can be achieved than by considering the amplitude ratios. Furthermore, the ASS distinctly indicates the braking event as a seismic source and the acceleration as an acoustic source. The ASS partially fails in the case of the controlled sources HP and H. With regard to the ASS, source H is supposed to have produced more sound than source HP. Since source HP is known as the seismic-acoustic surface source this ASS classification can be seen as a failure. Nevertheless, the ASS allows for a distinct discrimination of the two surface source types.

Table 6.2.: *Median value (MED) and MAD of the ASS for different signal sources*

source	MED	MAD
helicopter	63.6	5.2
D	83.9	4.7
bus (acc.)	28.9	9.6
bus (brake)	10.7	2.2
HP	16.6	7.5
H	24.5	4.4

6.3.3. Seismic and acoustic wave slowness

As mentioned in Sec. 4.1 the wave (phase) velocity can also be used to characterise the source (type) that produced the investigated signal. By contrast to the criteria discussed before, the computation of the velocity requires a more demanding processing of the data. This is mainly due to the computationally intensive array analysis if the data sets are large in both, the time-domain and the frequency-domain. If the slowness for a specific phase of a (seismic) wave is used for the source characterisation the corresponding portion in the signal has to be extracted. This extraction requires at least one interactive processing step. Nevertheless, the usability of the slowness as a characterisation criterion is obvious and shall be illustrated, too.

Table 6.3.: *Seismic slowness ranges computed for various source types*

source	s_{min} $(\mathrm{s\,km^{-1}})$	s_{max} $(\mathrm{s\,km^{-1}})$
helicopter	1.5	2.8
D	1.9	2.3
bus (acc.)	1.9	2.5
bus (brake)	1.9	2.5
HP (P wave)	0.7	1.2
HP (surface wave)	5.4	5.6
H (P wave)	0.7	1.2
H (surface wave)	5.4	5.6

The reciprocal of the velocity, namely the slowness, was computed via array analysis for different signals in the previous sections. The slowness ranges computed from the seismic data sets are summarised in Tab. 6.3. For the controlled seismic surface sources both, the body wave and the surface wave slowness ranges are given.

The slowness ranges computed from the acoustic data sets are summarised in Tab. 6.4. As expected these values differ significantly from the seismic slowness values. From the data set generated during the Knödelhütte experiment only the helicopter signals yielded equivalent slowness values for both types of data (seismic and acoustic).

Table 6.4.: *Acoustic slowness ranges computed for various source types*

source	s_{min}	s_{max}
helicopter	1.5	2.8
D	2.5	3.1
bus (acc.)	2.8	3.0
bus (brake)	2.8	3.0
HP	2.5	3.1
H	2.5	3.1

A reliable interpretation of the computed slowness values may only be possible based on a visual representation. Hence, a more detailed discussion of the results is given in Sec. 6.3.5.

6.3.4. A_{ratio}–ASS classification

The robust center values and the related robust variabilities ($\pm 1.5 \cdot$ MAD) of the amplitude ratios are plotted on the x-axis of the diagram shown in Fig. 6.53. In order to provide an optimal illustration of the amplitude ratios the x-axis is scaled in a logarithmic format. This illustration verifies the usability of the amplitude ratio as a sufficient measure in order to characterise the source type since the acoustic source D (red) can be clearly distinguished from the seismic sources HP (green) and H (blue). Hence, the amplitude ratio allows for a distinct separation of ground-based and airborne signal sources. As expected, the helicopter (yellow) is located near the pure acoustic source D in the diagram and thus is clearly delimited from the pure seismic sources. An interesting result was achieved for the signals produced by the passing bus. The log scaling of the x-axis enhances the visual separability of the deceleration (cyan) and the acceleration (magenta) of the bus. Furthermore, the separately computed amplitude ratios point out the usefulness of this classification criterion. In the case of the passing bus it would have been possible to assign a specific phase of the bus movement to its corresponding data set by just considering the amplitude ratios.
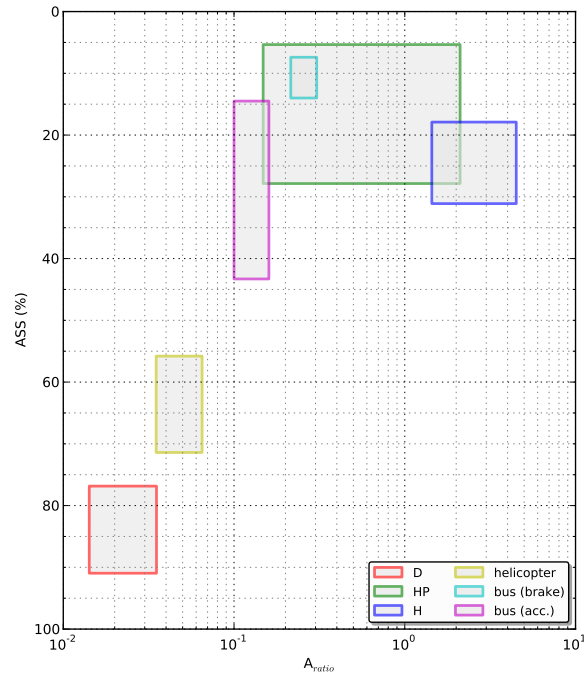
Figure 6.52.: *Seismic-acoustic source classification based on amplitude ratio and amplitude spectrum similarity*

The statistically described amplitude spectrum similarities summarised in Tab. 6.2 are plotted on the y-axis of the diagram shown in Fig. 6.52. In order to enhance the readability of the whole diagram the y-axis is reversed. From this illustration the amplitude spectrum similarity is proven to be a powerful stand-alone classification criterion, too. Based on the values computed for the investigated sources the seismic sources gather in the upper part of the diagram, while acoustic sources are located in the lower part.

Considering both axes simultaneously shows that the classification of sources based on a combination of both criteria is even more distinct. The (pure) acoustic sources are located in the lower left of the diagram based on their amplitude ratio and ASS. With increasing amplitude ratio and decreasing ASS the sources are classified as seismic sources located in the upper right of the diagram. As a consequence, the signals produced by a source that is located in the upper left or lower right sections of the diagram have to be investigated more precisely. The A_{ratio}–ASS plot illustrates the capability of this source classification based on the amplitude ratio and the amplitude spectrum similarity.

6.3.5. **A**$_{ratio}$**–slowness classification**

Since the amplitude ratio is the main classification criterion it is also plotted on the log-scale x-axis in the diagram shown in Fig. 6.53. The resultant source-dependent slowness ranges are plotted on the y-axis of the diagram. The combination of amplitude ratios and slowness ranges yields rectangular areas for each source type. Areas with solid edges rely on the slowness estimated from the seismic data, whereas dashed edges indicate slowness values estimated from the acoustic data. Based on the values summarised in Tab. 3.2 the variations of the speed of sound due to temperature and relative humidity can be computed. In Fig. 6.53 the corresponding slowness range is illustrated as a hatched area.
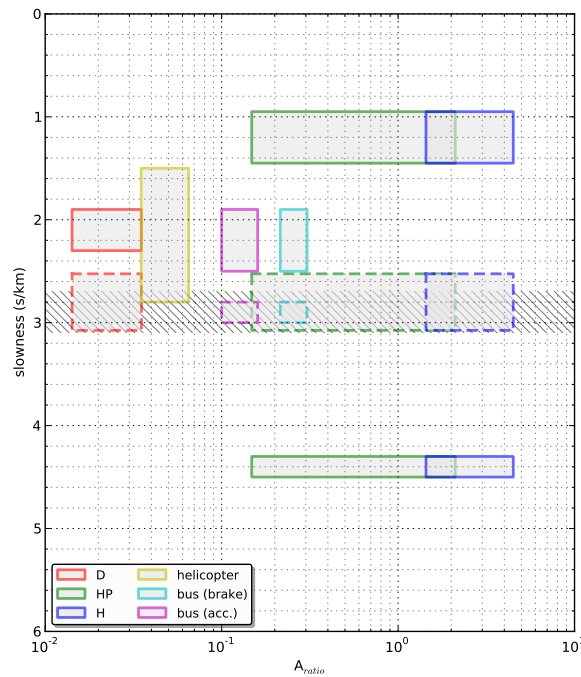
Figure 6.53.: *Seismic-acoustic source classification based on amplitude ratio and slowness:*
solid rectangles . . . seismic data
dashed rectangles . . . acoustic data
hatched area . . . acoustic slowness range

As can be seen from the diagram the slowness is an useful classification criterion. In case of the helicopter the resultant slowness range allows the assumption of a high altitude acoustic source[8] since the same slowness values are computed from the seismic and acoustic data sets. In case of the signals produced by sources HP and H the slowness allows for a discrimination of different wave phases. Lower slowness values indicate a body wave whereas higher slowness values are associated with surface waves. Hence, the slowness computed via array analysis can be used to identify the seismic wave phases.

---

[8]For this source type identical seismic and acoustic slowness values are assumed

Chapter 7

Conclusion

Seismic signals are produced by sources located in the Earth's crust, on the Earth's surface or above the Earth's surface. The subject of this study was to find a possibility to discriminate the different sources through the application of seismic sensors (geophones) and acoustic sensors (microphones).

The various sources were condensed into five rather generally described source types. The high altitude acoustic sources include human air traffic, e.g. airplanes and helicopters, as well as natural events like thunder. Near the surface the low altitude acoustic sources can be found. This source type describes sources that emit sound and act also as seismic sources. The seismic surface sources are split into two groups. One group of sources produces seismic signals in the ground but also intense acoustic signals. The second group produces mainly seismic signals while the emitted sound is negligible. The fifth source type unites all kinds of seismic subsurface sources, e.g. earthquakes or cavity impacts.

Within this study experiments were carried out at two different test sites. The seismic and acoustic sensors were installed in form of a triangular sensor array. The purpose of the experiments was to generate data sets that comprise distinct signal characteristics that can be used to categorise the sources that produced distinct signals. During the experiments signals produced by controlled and uncontrolled sources were recorded. The controlled sources included the standard source used in small scale seismic surveys, namely the hammer and a plate, as well as a pure acoustic source in form of a standard 26 " orchestra drum. A helicopter overflight, a passing bus and a nearby motorway made up the group of uncontrolled sources.

The recorded signals were analysed with different types of analysis techniques and tools. Basic characteristics of the time-domain signals were obtained by using standard time-domain illustrations of the recorded signals. These investigations provided information on the amplitudes of the signals in the seismic and acoustic data. The frequency content of the signals was investigated by computing spectrograms and amplitude spectra. The spectrograms provided an illustration of the frequency content of the signals plotted with respect to time. The amplitude spectra were used for the definition of filters which were applied on the data. In order to determine the produced seismic wave type particle motion plots were produced.

By using these plots the existence of body and surface waves in the seismic data was verified. Since the data were recorded with sensor arrays also array analysis was used for investigating the data. The resultant plots provide information on the backazimuth to the source that produced the signal and on the slowness at which the waves propagated across the array.

Based on the information obtained from the different analysis techniques the suggested classification criteria could be computed for real data. The resultant amplitude ratios (A_{ratio}) of seismic and acoustic signals, the amplitude spectrum similarities (ASS) and the seismic and acoustic slowness values were then used to generate classification diagrams. Since the amplitude ratio was assumed to be the most reliable criterion it was used as base parameter in these diagrams and therefore was plotted on the x-axis. In the first diagram the ASS was plotted on the y-axis of the diagram. In the final A_{ratio}–ASS plot acoustic sources can be found in the lower left of the diagram, while seismic sources are located in the upper right. Hence, this diagram allows to determine the source type that produced the investigated signal without knowing more than the signal amplitudes and the amplitude spectra. By plotting the computed slowness on the y-axis the A_{ratio}–slowness plot was obtained. Based on the slowness, this plot allows to identify high latitude acoustic sources and seismic wave phases.

To conclude, two important assumptions could be verified within this work. It was shown that the five newly defined source types can be used to classify signal sources based on easy to obtain signal characteristics. Furthermore, it was demonstrated that the usage of sensor arrays in combination with appropriate array analysis techniques is superior to installations of single sensors at a test site. Even minimal array installations (three array stations) provide a clear added value.

The classification based on the amplitude ratios and the amplitude spectrum similarity may have the potential for real-time usage. A real-time classification procedure relying on the A_{ratio}-ASS approach could be used to prevent sound-induced signals being processed by geophysical analysis tools. For example, would it be of particular importance for studies hunting for earthquake precursors. The data amount arising from such investigations is already enormous since a big variety of sensor data is recorded. Omitting non-subsurface signals might significantly reduce the amount of data.

For further development of the source classification discussed in the present thesis some improvement suggestions should be considered. These suggestions concern the experiment equipment, the installation of the used sensors as well as the sources or source types used for the experiments.

The equipment utilised in future in-situ experiments should be modified in order to efficiently use the available resources. Instead of using three 3C-geophones at three array points the seismic array should comprise just one 3C-geophone.

By reducing the number of 3C-geophones the deallocated channels on the seismic recorder can be equipped with additional Z-geophones and microphones while the particle motions still can be investigated. Based on the twelve channels available on two Ref Tek seismic recorders three channels would be used by the 3C-geophone, four channels would be occupied by four Z-geophones and the remaining five channels would host five microphones. Hence, by using the same number of seismic recorders an array consisting of five array stations could be installed. Each array station would be equipped with a seismic and an acoustic sensor. Furthermore, an increased spatial extent might enhance the capabilities of the array. Two possible array layouts with five stations are shown in Fig. 7.1. The layout of a five station sensor array might either be diamond-shaped or L-shaped. By using different components or combinations of single components the variables shown on the far right of Fig. 7.1 can be computed. These variables were already used in the present thesis for the classification of sources.
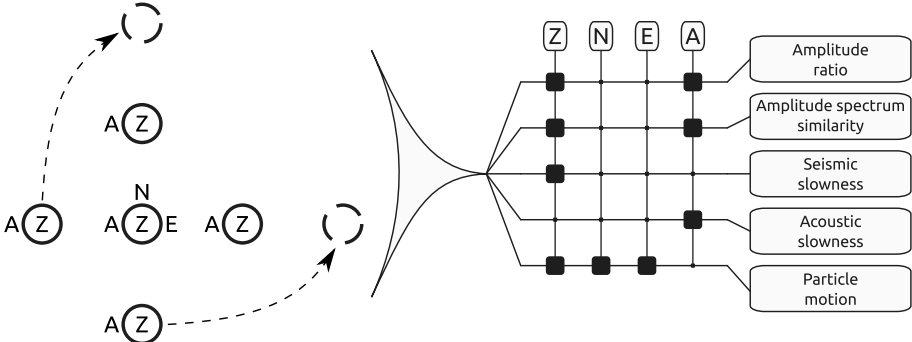
Figure 7.1.: *Data flow based on a five station array layout*

In order to improve the significance of the amplitude ratios computed from the seismic and acoustic signal amplitudes the geophones should be installed beneath the topmost weathering layer. This precaution would probably decrease the amplitude ratios computed for signals produced by a high altitude acoustic source.

The data basis generated and used in this thesis is heterogeneous but still small. Thus, in future experiments well-defined controlled seismic sources (including subsurface sources) and different low altitude acoustic sources should be used. Additionally, the various types of cultural noise and actual earthquakes should be monitored.

For a reliable interpretation of the slowness values computed via array analysis a detailed seismic exploration of near surface structures should be carried out at future experiment sites. This would provide information on the structures in the subsurface and the velocities that have to be expected.

Appendices

Appendix A

Figures

A.1. Signals and windows associated with source H
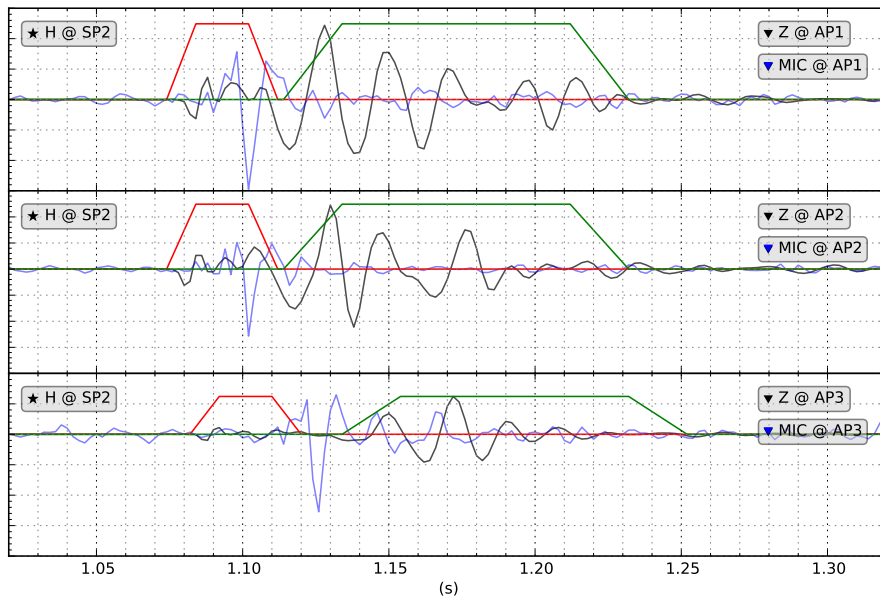
Figure A.1.: *Signals produced by source H (one hammer stroke) at shot point SP2 observed with the KNH geophone and microphone array:*

black	...	*seismic data*
blue	...	*acoustic data*
red	...	*body wave window*
green	...	*surface wave window*

A.2. Particle motion plots source H
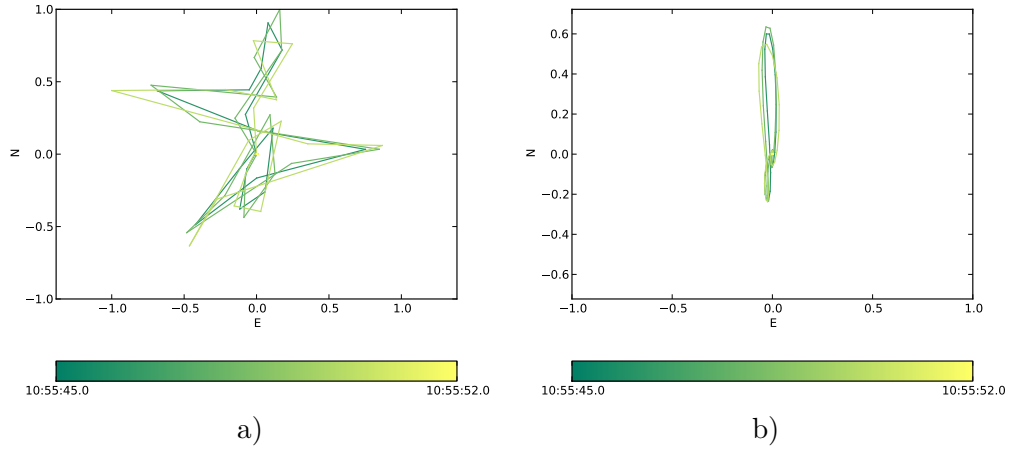
Figure A.2.: *Particle motion associated with the P wave produced by source H at SP2: a) E–N plane b) E–N plane (low-pass filtered)*
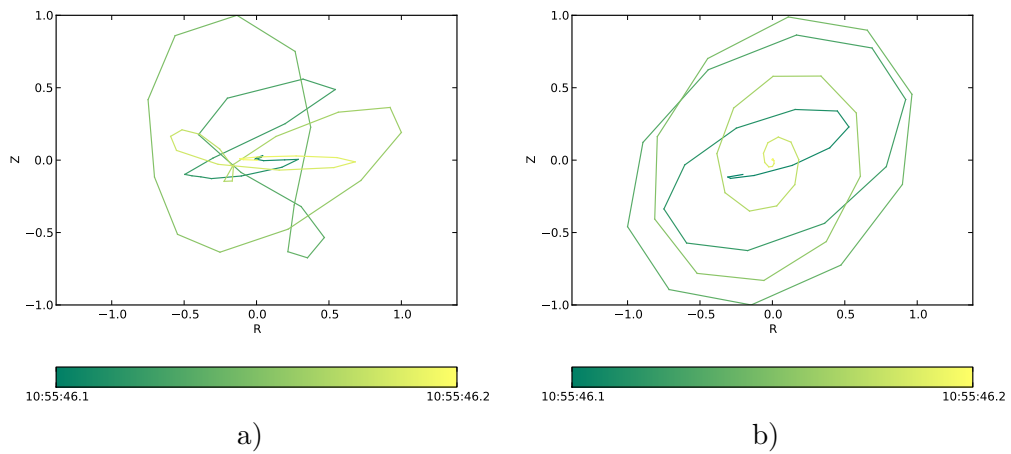
Figure A.3.: *Particle motion associated with the surface wave portion of the signal produced by source HP at SP2: a) R–Z plane b) R–Z plane (low-pass filtered)*

Appendix B

Additional information and tables

B.1. Computation of seismic-acoustic amplitude ratios for source D

The subsequently summarized maximum amplitude values were taken from the detrended seismic and acoustic data sets.

Table B.1.: *Maximum amplitude values for controlled source D*

		AP1			AP2			AP3		
		Z	MIC	ratio	Z	MIC	ratio	Z	MIC	ratio
SP1	1st	44206	2422110	0.0183	12219	1024160	0.0119	56336	978070	0.0576
	2nd	54876	2387660	0.0230	16877	1025100	0.0165	78232	1118240	0.0700
	3rd	68753	2934840	0.0234	21835	1484990	0.0147	95956	1508380	0.0636
SP2	1st	31137	940152	0.0331	19735	1032810	0.0191	39731	664389	0.0598
	2nd	48868	1567530	0.0312	27533	1726350	0.0159	67613	664389	0.0722
	3rd	53275	1064290	0.0501	30732	1253240	0.0245	52965	1007670	0.0526
SP3	1st	31450	1069910	0.0294	61850	2695910	0.0229	76612	921689	0.0831
	2nd	37409	1127550	0.0332	68831	3359600	0.0205	87401	1084610	0.0806
	3rd	37699	1560780	0.0242	79520	3866010	0.0206	113715	1428100	0.0796
SP4	1st	30724	1282110	0.0240	58986	3193720	0.0185	139983	1870520	0.0748
	2nd	24433	897010	0.0272	50830	2130790	0.0239	84724	1083530	0.0782
	3rd	28393	1089700	0.0261	58219	2888720	0.0202	123511	1694030	0.0729
SP5	1st	30096	1275880	0.0236	23290	1287220	0.0181	508989	3898030	0.1306
	2nd	28596	1292060	0.0221	25862	1376200	0.0188	511530	3882830	0.1317
	3rd	33299	1349640	0.0247	24497	1384810	0.0177	581608	4175820	0.1393

B.2. Computation of seismic-acoustic amplitude ratios for source HP

The subsequently summarized maximum amplitude values were taken from the detrended seismic and acoustic data sets.

Table B.2.: *Maximum amplitude values for controlled source HP*

| | | AP1 | | | | AP2 | | | AP3 | |
		Z	MIC	ratio	Z	MIC	ratio	Z	MIC	ratio
SP1	1st	410552	197997	2.0735	70942	90879	0.7806	98166	96744	1.0147
	2nd	456446	243286	1.8762	75849	108411	0.6996	104894	112942	0.9287
	3rd	490899	218713	2.2445	81545	101119	0.8064	109780	119066	0.9220
SP2	1st	80250	46067	1.7420	101597	54426	1.8667	70619	35784	1.9735
	2nd	84406	38162	2.2170	106787	63369	1.6852	75089	38072	1.9723
	3rd	81677	37932	2.1532	105906	55564	1.9060	74687	37222	2.0065
SP3	1st	71340	71961	0.9914	750143	125698	5.9678	122294	41854	2.9219
	2nd	74340	67097	1.1079	724478	158642	4.5667	123453	51000	2.4206
	3rd	75124	75749	0.9917	746024	199643	3.7368	123986	69591	1.7816
SP4	1st	26742	119676	0.2235	389606	219092	1.7783	156080	142428	1.0959
	2nd	22991	98080	0.2344	259901	327175	0.7944	127294	128355	0.9917
	3rd	29070	113494	0.2561	378790	242192	1.5640	160691	170108	0.9446
SP5	1st	35340	79434	0.4449	50106	100889	0.4966	424260	286400	1.4814
	2nd	35796	74731	0.4790	43686	72176	0.6053	411210	220176	1.8676
	3rd	39087	123721	0.3159	51527	109292	0.4715	434180	384835	1.1282

B.3. Computation of seismic-acoustic amplitude ratios for source H

The subsequently summarized maximum amplitude values were taken from the detrended seismic and acoustic data sets.

Table B.3.: *Maximum amplitude values for controlled source H*

| | | AP1 | | | AP2 | | | AP3 | | |
		Z	MIC	ratio	Z	MIC	ratio	Z	MIC	ratio
SP1	1st	401078	96965	4.1363	74995	41476	1.8082	102530	34139	3.0033
	2nd	478779	114466	4.1827	81219	46415	1.7498	114179	37753	3.0244
	3rd	503787	139656	3.6073	83835	57559	1.4565	116045	54060	2.1466
SP2	1st	102538	32960	3.1110	122401	36872	3.3196	84551	25969	3.2558
	2nd	104609	29762	3.5149	124404	45508	2.7337	83559	28155	2.9678
	3rd	104466	30337	3.4435	121010	36128	3.3495	78637	34080	2.3074
SP3	1st	69455	56431	1.2308	782056	125063	6.2533	113612	58282	1.9493
	2nd	74737	68830	1.0858	901347	214751	4.1972	111826	59050	1.8938
	3rd	77219	64695	1.1936	905149	267857	3.3792	117824	71314	1.6522
SP4	1st	30396	27587	1.1018	440215	67751	6.4975	159268	42967	3.7068
	2nd	36654	41887	0.8751	526426	103586	5.0820	195268	65370	2.9925
	3rd	40869	40449	1.0104	558386	102866	5.4283	212072	72895	2.9093
SP5	1st	38525	35689	1.0795	71766	34302	2.0922	412534	126210	3.2686
	2nd	47044	34278	1.3724	82865	37914	2.1856	441158	121758	3.6232
	3rd	52220	38341	1.3620	81072	43242	1.8748	447607	142573	3.1395

B.4. Amplitude spectrum similarity for different source types

Table B.4.: *Amplitude spectrum similarity (ASS) for controlled sources D, HP and H*

src	SP	AP	ASS	src	SP	AP	ASS	src	SP	AP	ASS
	1	1	93.1		1	1	12.0		1	1	3.3
		2	83.8			2	17.8			2	4.4
		3	89.3			3	10.5			3	2.6
	2	1	74.9		2	1	41.4		2	1	39.8
		2	79.7			2	2.3			2	21.1
		3	83.8			3	17.8			3	26.3
	3	1	84.4		3	1	32.9		3	1	34.1
D		2	88.6	HP		2	32.7	H		2	27.8
		3	83.9			3	2.6			3	20.1
	4	1	89.9		4	1	32.3		4	1	13.6
		2	80.6			2	9.1			2	25.7
		3	88.6			3	20.5			3	27.7
	5	1	90.0		5	1	2.6		5	1	24.5
		2	67.7			2	9.3			2	23.8
		3	83.9			3	16.6			3	39.2

Appendix C

Source Code

The source code of the Python functions written as a part of this thesis is listed subsequently. These functions were developed in order to be able to process, analyse and visualise the data recorded during the in-situ experiments and should not be rated with regard to user-friendliness and efficiency.

Imports

```python
import matplotlib.pyplot as plt;
import matplotlib.colors as clrs;
import matplotlib.cm as cmx;
from matplotlib.patches import Arc;
import numpy as np;
from obspy.signal import cpxtrace;
from scipy import fftpack;
```

Envelope

```python
def compEnvelope(tr):
    # make a deep copy of the given trace
    enve = tr.copy();

    # compute the envelope of the data
    enve.data = filter.envelope(enve.data);

    return enve;
```

Median absolute deviation

```python
def mad(a):
    # compute median of given data set
    median = np.median(a);

    # calculate the absolute deviations from the median
    ad = np.abs(a-median);

    # compute the median of the absolute deviations --> MAD
    mad = np.median(ad);

    return mad;
```

Synthetic signal generation

```python
def synthsiggen(samprate=500.0,peaks=3,noise=False):
    # synthetic signal generation modified after (Almendros,1999)
    A = 1; # m/s
    B = 2;
    t0 = 0.15; # s
    f0 = 11; # Hz
    nl = 1400; # noise level

    # combine three pulses to a synthetic signal
    sig = np.array([0]*int(1*samprate));
    for i in np.arange(0,peaks):
        sig = np.append(sig,
                np.array([
                (25*(t/t0)**B*np.exp(-t/t0)*np.sin(2*np.pi*f0*t)) *
                (25*(t/t0)**4*np.exp(-t/t0)*np.sin(2*np.pi*29*t)) *
                (25*(t/t0)**1*np.exp(-t/t0)*np.sin(2*np.pi*2*t)) \
                for t in np.arange(0,1,1.0/samprate)]));
        sig = np.append(sig,np.array([0]*int(1*samprate)));

    # add noise
    if noise: sig += (np.random.normal(0,1,int(7*samprate))*nl);

    return sig;
```

Appendix C. Source Code

Amplitude spectrum

```python
def ampspec(tr,starttime,endtime,source='',fmin=0,fmax=0):
  if starttime >= tr.stats.starttime and \
    endtime <= tr.stats.endtime:

    # apply bandpass filter
    if not (fmin==0 and fmax==0):
      tr.filter('bandpass',freqmin=fmin,freqmax=fmax,
            corners=4,zerophase=True);

    # trim trace
    tr.trim(starttime,endtime);

    # subtract mean
    tr.data = tr.data - np.mean(tr.data);

    # compute amplitude spectrum
    spec = fftpack.fft(tr.data)/tr.stats.npts;
    spec = spec[range(tr.stats.npts/2)];
    Yf = np.abs(spec);
    freq = np.arange(tr.stats.npts)/ \
          (tr.stats.npts/tr.stats.sampling_rate);
    freq = freq[range(tr.stats.npts/2)];

    # plot amplitude spectrum
    f = plt.figure(figsize=(10,3));
    ax0 = plt.subplot(111,axisbg='.9');
    for x,y in zip(freq,Yf):
      ax0.bar(left=x,height=y,bottom=0,edgecolor='None',color='g');
    ax0.set_xlim([0,260]);
    ax0.set_ylim([0,np.max(Yf)]);
    ax0.set_xticks(np.linspace(0,260,14));
    ax0.set_xlabel('(Hz)');
    ax0.text(.88,.9,
          r'$\blacktriangledown$ ' + tr.stats.channel,
          bbox = dict(boxstyle='round',facecolor='0.8',
                edgecolor='k',alpha=.5),
          transform = ax0.transAxes,ha='left',va='center');
    ax0.text(.02,.9,
          r'$\bigstar$ ' + source,
          bbox = dict(boxstyle='round',facecolor='0.8',
                edgecolor='k',alpha=.5),
          transform = ax0.transAxes,ha='left',va='center');

    # format plot
    plt.rc('font', size=10);
    f.tight_layout();

    plt.show();
```

Multiple seismograms illustration

```python
def multseism(st,starttime,endtime,source,
          window,shift,
          fmin=0,fmax=0,fminmic=0,fmaxmic=0,
          combined=True):
  if starttime >= st[0].stats.starttime and \
    endtime <= st[0].stats.endtime:

    # trim stream
    st.trim(starttime,endtime);

    # apply bandpass filter
    if not (fmin==0 and fmax==0):
      for tr in st[0:3]:
        tr.filter('bandpass',freqmin=fmin,freqmax=fmax,
              corners=2,zerophase=True);

    if not (fminmic==0 and fmaxmic==0):
      for tr in st[3:6]:
        tr.filter('bandpass',freqmin=fminmic,freqmax=fmaxmic,
```

```python
            corners=2,zerophase=True);

    # amplitude equalization
    amp_max = float(np.max([np.max(np.abs(tr.data)) for tr in st]));
    for idx,tr in enumerate(st):
      st[idx].data = st[idx].data * (amp_max/np.max(st[idx].data));

    # plot data
    plt.rc('font', size=10);
    f,axarr = plt.subplots(3,sharex=True,figsize=(10,6));

    t = np.arange(st[0].stats.npts,dtype='float32')/ \
      st[0].stats.sampling_rate;

    for ax,tr in zip(axarr,st[0:3]):
      ax.plot(t,tr.data,'.3',alpha=1);
      ax.text(.02,.86,
            r'$\bigstar$ ' + source,
            bbox = dict(boxstyle='round',facecolor='0.8',
                  edgecolor='k',alpha=.5),
                  transform = ax.transAxes,
                  ha='left',va='center');
      ax.text(.86,.86,
            r'$\blacktriangledown$ ' + tr.stats.channel,
            bbox = dict(boxstyle='round',facecolor='0.8',
                  edgecolor='k',alpha=.5),
                  transform = ax.transAxes,
                  ha='left',va='center');
      ax.xaxis.grid(b=True,which='major',color='k');
      ax.yaxis.grid(b=True,which='major',color='.5');
      ax.minorticks_on();
      ax.xaxis.grid(b=True,which='minor',color='.5');
      plt.setp(ax.get_yticklabels(),visible=False);
    axarr[2].set_xlabel('(s)');

    if combined:
      for ax,tr in zip(axarr,st[3:6]):
        tr.filter('highpass',freq=20,zerophase=True);
        ax.plot(t,tr.data,'b',alpha=.5);
        ax.text(.86,.68,#.86,.86,
              r'$\blacktriangledown$ ' +
                  tr.stats.channel,color='k',
              bbox = dict(boxstyle='round',facecolor='0.8',
                    edgecolor='k',alpha=.5),
                    transform = ax.transAxes,
                    ha='left',va='center');
        ax.text(.86,.68, #.86,.86,
              r'$\blacktriangledown$',color='b',
              transform = ax.transAxes,ha='left',va='center');

    # plot windows
    window = window * amp_max;
    axarr[0].plot(t,window,'r',lw=1.);
    axarr[1].plot(t,window,'r',lw=1.);
    axarr[2].plot(t,np.roll(window,
                int(shift*st[0].stats.sampling_rate)),
            'r',lw=1.);

    # format plot
    axarr[2].set_xlim([1.02,1.32]);
    plt.setp(axarr[0].get_xticklabels(),visible=False);
    plt.setp(axarr[1].get_xticklabels(),visible=False);
    f.subplots_adjust(hspace=0);

    plt.show();
```

Particle motion

```python
def partmot(st,starttime,endtime,baz=0.,bazrng=[0.,0.]):
    # rotate the seismograms by the given backazimuth
    st.rotate(method='NE->RT',back_azimuth=45.);

    # set start- and endtime
    st.trim(starttime,endtime);

    # normalize the data
    st.normalize();

    # split data into segments
    points = np.array([st[1].data,st[0].data]).T.reshape(-1, 1, 2);
    segments = np.concatenate([points[:-1],points[1:]],axis=1);

    # init colorbar
    cmap = plt.get_cmap('summer');
    cNorm = clrs.Normalize(vmin=0,vmax=len(segments));
    scalarMap = cmx.ScalarMappable(norm=cNorm,cmap=cmap);
    scalarMap._A = [];

    # init figure
    f,ax = plt.subplots(1,sharex=True,figsize=(6,6));
    plt.rc('font', size=10);

    # plot known backazimuth range
    arc = Arc([0,0],2,2,
              theta1=bazrng[0],theta2=bazrng[1],
              color='b',alpha='1',lw=3.);
    ax.add_patch(arc);

    # plot data segments with colourcode
    for idx,seg in enumerate(segments):
        ax.plot([seg[0][0],seg[1][0]],[seg[0][1],seg[1][1]],
                color=scalarMap.to_rgba(idx));

    # format plot
    ax.axis('equal');
    ax.set_xlabel(st[1].stats.channel.strip());
    ax.set_ylabel(st[0].stats.channel.strip());
    ax.set_xlim([-1,1]);
    ax.set_ylim([-1,1]);
    cbar = plt.colorbar(scalarMap,orientation='horizontal',
                        ticks=[0,len(segments)]);
    cbar.ax.set_xticklabels(
        [st[0].stats.starttime.strftime('%X.%f')[0:-5],
         st[0].stats.endtime.strftime('%X.%f')[0:-5]]);
    plt.show();
```

Record section

```python
def recsec(st,starttime,endtime):
    # trim stream
    st.trim(starttime,endtime);
    dT = endtime - starttime;

    # sort stream by distance
    st.sort(keys=['distance']);

    # improve data characteristics
    st.normalize(global_max=True);

    # compute envelopes
    st_enve = st.copy();
    st_enve[0].data = filter.envelope(st[0].data);
    st_enve[1].data = filter.envelope(st[1].data);
    st_enve[2].data = filter.envelope(st[2].data);
    st_enve.normalize(global_max=True);

    # plot data
    st.trim(starttime,starttime);
    st_enve.trim(starttime,starttime);
    f,ax = plt.subplots(1,sharex=True,figsize=(10,6));
    plt.rc('font', size=10);
    for tr,enve in zip(st,st_enve):
        t = np.arange(tr.stats.npts,dtype='float32')/ \
            tr.stats.sampling_rate;
        ax.plot(tr.data+tr.stats.distance,t,'k');
        ax.plot(enve.data+enve.stats.distance,t,'c');

    ax.set_xlabel('Offset (m)');
    ax.xaxis.tick_top();
    ax.xaxis.set_label_position('top');
    ax.set_xlim([0,
                np.ceil(np.max([st[0].stats.distance,
                                st[1].stats.distance,
                                st[2].stats.distance]))]);
    ax.set_ylabel('Time (s)');

    # format plot
    ax.xaxis.grid(b=True,which='major',color='k');
    ax.yaxis.grid(b=True,which='major',color='k');
    ax.minorticks_on();
    ax.xaxis.grid(b=True,which='minor',color='.5');
    ax.yaxis.grid(b=True,which='minor',color='.5');
    f.tight_layout();
    f.subplots_adjust(hspace=0);
    plt.gca().invert_yaxis();

    plt.show();
```

Appendix C. Source Code

Signal and spectrogram

```python
def dataspecgram(tr,starttime,endtime,source,
                 fmin=0,fmax=0,enve=False):
    if starttime >= tr.stats.starttime and \
       endtime <= tr.stats.endtime:

        # trim trace
        tr.trim(starttime,endtime);

        # apply bandpass filter
        if not (fmin==0 and fmax==0):
            tr.filter('bandpass',freqmin=fmin,freqmax=fmax,
                      corners=4,zerophase=True);

        # subtract mean
        tr.data = tr.data - np.mean(tr.data);

        # plot data
        f = plt.figure(figsize=(10,4));
        ax0 = plt.subplot(211);
        t = np.arange(tr.stats.npts,dtype='float32')/ \
            tr.stats.sampling_rate;
        ax0.plot(t,tr.data,'.3');
        if enve: ax0.plot(t,
                          compEnvelope(tr,.5*tr.stats.sampling_rate).data,
                          'c');
        ax0.text(.88,.88,
                 r'$\blacktriangledown$ ' + tr.stats.channel,
                 bbox = dict(boxstyle='round',facecolor='0.8',
                             edgecolor='k',alpha=.5),
                 transform = ax0.transAxes,ha='left',va='center');
        ax0.text(.02,.88,
                 r'$\bigstar$ ' + source,
                 bbox = dict(boxstyle='round',facecolor='0.8',
                             edgecolor='k',alpha=.5),
                 transform = ax0.transAxes,ha='left',va='center');
        ax0.set_ylabel('(counts)');
        plt.ticklabel_format(style='sci',axis='y',scilimits=(0,0));

        # plot spectrogram
        ax1 = plt.subplot(212,sharex=ax0);
        tr.spectrogram(axes=ax1,show=True,per_lap=.99,wlen=1,log=False);
        tticks = [starttime.strftime('%H:%M:%S'),
                  (starttime+
                   (endtime-
                    starttime)/2).strftime('%H:%M:%S'),
                  endtime.strftime('%H:%M:%S')];
        ax1.set_xticks(np.linspace(0,int((endtime-
                                          starttime)),3));
        ax1.set_xticklabels(tticks,rotation=0);
        ax1.set_ylabel('(Hz)');

        # format plot
        plt.setp(ax0.get_xticklabels(),visible=False);
        plt.rc('font', size=10);
        f.tight_layout();

        plt.show();
```

Bibliography

Aki, K. and Richards, P. G. (2002). *Quantitative Seismology*. Ed. by Jane Ellis. 2nd ed. University Science Books.

Almendros, J., Ibáñez, J. M., Alguacil, G. and Pezzo, E. D. (1999). 'Array analysis using circular-wave-front geometry: an application to locate the nearby seismo-volcanic source'. In: *Geophysical Journal International* 136, pp. 159–170.

Baisch, S., Carbon, D., Dannwolf, U., Delacou, B., Devaux, M., Dunand, F., Jung, R., Koller, M., Martin, C., Sartor, M., Secanell, R. and Vörös, R. (2009). *Deep Heat Mining Basel - Seismic Risk Analysis*. Tech. rep. Departement für Wirtschaft, Soziales und Umwelt des Kantons Basel-Stadt Amt für Umwelt und Energie.

Beyreuther, M., Barsch, R., Krischer, L., Megies, T., Behr, Y. and Wassermann, J. (2010). 'ObsPy: A Python Toolbox for Seismology'. In: *SRL* 81.3, pp. 530–533. DOI: 10.1785/gssrl. 81.3.530.

Biescas, B., Dufour, F., Furdada, G., Khazaradze, G. and Suriñach, E. (2003). 'Frequency content evolution of snow avalanche seismic signals'. In: *Surveys in geophysics* 24.5-6, pp. 447–464.

Bohn, D. A. (1988). 'Environmental Effects on the Speed of Sound'. In: *Journal of the Audio Engineering Society* 36.

Bolt, B. A. (1982). *Inside the Earth: Evidence from Earthquakes*. W. H. Freeman and Company.

Bolt, B. A. (2000). *Earthquakes*. 4th ed. W. H. Freeman and Company.

Bormann, P., Baumbach, M., Bock, G., Grosser, H., Choy, G. L. and Boatwright, J. (2002). 'Seismic Sources and Source Parameters'. In: *New Manual of Seismological Observatory Practice*. GeoForschungsZentrum Potsdam.

Bormann, P., Engdahl, B. and Kind, R. (2002). 'Seismic Wave Propagation and Earth models'. In: *New Manual of Seismological Observatory Practice*. GeoForschungsZentrum Potsdam.

Bibliography

Braile, L. (2010). *Seismic Wave Demonstrations and Animations.* Accessed: 25th February, 2015. URL: `http://web.ics.purdue.edu/~braile/isw/motion.htm`.

Bromley, C. J. and Mongillo, M. A. (2008). 'Geothermal Energy from Fractured Reservoirs - Dealing with Induced Seismicity'. In: *IEA OPEN Energy Technology Bulletin* 48.

Brückl, E., Weber, R., Apoloner, M. T., Brückl, J., Loderer, W., Maras, J., Mertl, S., Moeller, G., Schurr, B., Weginger, S. and Umnig, E. (2014). *ALPAACT - Seismological and Geodetic Monitoring of Alpine-PAnnonian Active Tectonics.* Tech. rep. Österreichische Akademie der Wissenschaften.

Capon, J. (Aug. 1969). 'High-resolution frequency-wavenumber spectrum analysis'. In: *Proceedings of the IEEE* 57.8, pp. 1408–1418. ISSN: 0018-9219. DOI: `10.1109/PROC.1969.7278`.

Capon, J. (1973). 'Signal processing and frequency-wavenumber spectrum analysis for a large aperture seismic array'. In: *Methods in Computational Physics* 13, pp. 1–59.

Cooley, J. W. and Tukey, J. W. (1965). 'An Algorithm for the Machine Calculation of Complex Fourier Series'. English. In: *Mathematics of Computation* 19.90, pp. 297–301. ISSN: 00255718. URL: `http://www.jstor.org/stable/2003354`.

Deparis, J., Jongmans, D., Cotton, F., Baillet, L., Thouvenot, F. and Hantz, D. (2008). 'Analysis of rock-fall and rock-fall avalanche seismograms in the French Alps'. In: *Bulletin of the Seismological Society of America* 98.4, pp. 1781–1796.

Dysart, P. S. and Pulli, J. J. (1990). 'Regional seismic event classification at the NORESS array: seismological measurements and the use of trained neural networks'. In: *Bulletin of the Seismological Society of America* 80.6B, pp. 1910–1933.

Esposito, A., Giudicepietro, F., Scarpetta, S., D'Auria, L., Marinaro, M. and Martini, M. (2006). 'Automatic discrimination among landslide, explosion-quake, and microtremor seismic signals at Stromboli Volcano using neural networks'. In: *Bulletin of the Seismological Society of America* 96.4A, pp. 1230–1240.

Fritschen, R. and Rüter, H. (2010). 'Induzierte Seismizität–Ein Problem der Tiefen Geothermie'. In: *Geothermische Energie* 5.66, pp. 6–13.

Gadallah, M. R. and Fisher, R. (2009). *Exploration Geophysics.* Springer Verlag.

Häge, M., Blascheck, P. and Joswig, M. (2013). 'EGS hydraulic stimulation monitoring by surface arrays - location accuracy and completeness magnitude: the Basel Deep Heat Mining Project case study'. In: *Journal of Seismology* 17, pp. 51–61.

Harjes, H. P. and Henger, M. (1973). 'Array-Seismologie'. In: *Zeitschrift für Geophysik* 39, pp. 865–905.

Highland, L. (2004). *Landslide Types and Processes*. USGS Fact Sheet 2004–3072.

Hunter, J. D. (2007). 'Matplotlib: A 2D graphics environment'. In: *Computing In Science & Engineering* 9.3, pp. 90–95.

Jones, E., Oliphant, T., Peterson, P. et al. (2001–). *SciPy: Open source scientific tools for Python.* Accessed: 20th February, 2015. URL: http://www.scipy.org/.

Joswig, M. (2008). 'Nanoseismic monitoring fills the gap between microseismic networks and passive seismic'. In: *first break* 26, pp. 117–124.

Kanasewich, E. R. (1981). *Time Sequence Analysis in Geophysics*. University of Alberta Press. ISBN: 9780888640741.

Kearey, P., Brooks, M. and Hill, I. (2002). *An Introduction to Geophysical Exploration*. 3rd ed. Blackwell Science.

Kelly, E. J. (1967). *Response of seismic arrays to wide-band signals*. Tech. rep. DTIC Document.

Kogelnig, A., Hübl, J., Suriñach, E., Vilajosana, I. and McArdell, B. W. (2014). 'Infrasound produced by debris flow: propagation and frequency content evolution'. In: *Natural Hazards* 70.3, pp. 1713–1733.

Kuttruff, H. (2007). *Acoustics - An introduction*. Taylor & Francis.

Langer, H., Falsaperla, S., Powell, T. and Thompson, G. (2006). 'Automatic classification and a-posteriori analysis of seismic event identification at Soufriere Hills volcano, Montserrat'. In: *Journal of volcanology and geothermal research* 153.1, pp. 1–10.

La Rocca, M., Galluzzo, D., Saccorotti, G., Tinti, S., Cimini, G. B. and Del Pezzo, E. (2004). 'Seismic signals associated with landslides and with a tsunami at Stromboli volcano, Italy'. In: *Bulletin of the Seismological Society of America* 94.5, pp. 1850–1867.

Bibliography

Lowrie, W. (1997). *Fundamentals of Geophysics.* Cambridge University Press.

Mari, J. L., Glangeaud, F. and Coppens, F. (1999). *Signal processing for geologists & geophysicists.* Institut francais du pétrole publications.

Milsom, J. (2003). *Field Geophysics.* John Wiley & Sons Ltd.

Mulargia, F. and Bizzarri, A. (2014). 'Anthropogenic tritrigger of large Earthquakes'. In: *Scientific Reports* 4.

Petri, P., Hikade, R. and Kuschel, A. (2010). *Handbuch Sprengtechnik: Nachschlagewerk und Leitfaden für Sprengbefugte.* 2nd ed. Plöchl.

REF TEK 130S Users Guide (2014). Trimble Navigation Limited.

Rost, S. and Thomas, C. (2002). 'Array seismology: methods and applications'. In: *Reviews of Geophysics* 40.3, pp. 1–27.

Rowe, C., Aster, R., Kyle, P., Dibble, R. and Schlue, J. (2000). 'Seismic and acoustic observations at Mount Erebus Volcano, Ross Island, Antarctica, 1994–1998'. In: *Journal of Volcanology and Geothermal Research* 101.1, pp. 105–128.

Scarpetta, S., Giudicepietro, F., Ezin, E., Petrosino, S., Del Pezzo, E., Martini, M. and Marinaro, M. (2005). 'Automatic classification of seismic signals at Mt. Vesuvius volcano, Italy, using neural networks'. In: *Bulletin of the Seismological Society of America* 95.1, pp. 185–196.

Schnabel, W. (1997). 'Baden 1:50.000'. In: *Geologische Karte der Republik Österreich 1:50.000.* Geologische Bundesanstalt.

Schnabel, W. (2002). *Geologische Karte von Niederösterreich 1:200.000.* Geologische Bundesanstalt.

Schweitzer, J., Fyen, J., Mykkeltveit, S. and Kværna, T. (2002). 'Seismic Arrays'. In: *New Manual of Seismological Observatory Practice.* GeoForschungsZentrum Potsdam.

Shearer, P. M. (1999). *Introduction to seismology.* Cambridge University Press.

Sheriff, R. E. and Geldart, L. P. (1995). *Exploration Seismology.* Cambridge University Press.

Stein, S. and Wysession, M. (2007). *An Introduction to Seismology, Earthquakes, and Earth Structure.* 7th ed. Blackwell Publishing.

Suriñach, E., Sabot, F., Furdada, G., Vilaplana, J. et al. (2000). 'Study of seismic signals of artificially released snow avalanches for monitoring purposes'. In: *Physics and Chemistry of the Earth, Part B: Hydrology, Oceans and Atmosphere* 25.9, pp. 721–727.

Suriñach, E., Vilajosana, I., Khazaradze, G., Biescas, B., Furdada, G. and Vilaplana, J. (2005). 'Seismic detection and characterization of landslides and other mass movements'. In: *Natural Hazards and Earth System Science* 5.6, pp. 791–798.

Telford, W. M., Geldart, L. P. and Sheriff, R. E. (1990). *Applied Geophysics*. 2nd ed. Camebridge University Press.

Vilajosana, I., Suriñach, E., Abellán, A., Khazaradze, G., Garcia, D. and Llosa, J. (2008). 'Rockfall induced seismic signals: case study in Montserrat, Catalonia'. In: *Natural Hazards and Earth System Science* 8.4, pp. 805–812.

Wagreich, M. (2008). 'Lithostratigraphic definition and depositional model of the Hütteldorf Formation (Upper Albian-Turonian, Rhenodanubian Flysch Zone, Austria)'. In: *Austrian Journal of Earth Sciences* 101, pp. 70–80.

Zhang, J., Gerstoft, P. and Shearer, P. M. (2009). 'High-frequency P-wave seismic noise driven by ocean winds'. In: *Geophysical Research Letters* 36.9.